I.O.S.

THE MOVEMENT OF NON-COHESIVE SEDIMENT BY
SURFACE WATER WAVES

by

A G Davies, N A Frederiksen* and R H Wilkinson

Part II

Experimental Study

REPORT No. 46

1977

INSTITUTE OF OCEANOGRAPHIC SCIENCES

Wormley, Godalming,
Surrey, GU8 5UB.
(0428 - 79 - 4141)

(Director: Professor H. Charnock)

Bidston Observatory,
Birkenhead,
Merseyside, L43 7RA.
(051-653-8633)

(Assistant Director: Dr. D. E. Cartwright)

Crossway,
Taunton,
Somerset, TA1 2DW.
(0823-86211)

(Assistant Director: M. J. Tucker)

Marine Scientific Equipment Service
Research Vessel Base,
No. 1 Dock.
Barry,
South Glamorgan, CF6 6UZ.
(0446-737451)
(Officer-in-Charge: Dr. L. M. Skinner)

THE MOVEMENT OF NON-COHESIVE SEDIMENT BY

SURFACE WATER WAVES

by

A G Davies, N A Frederiksen* and R H Wilkinson

Part II

Experimental Study

Report No 46

1977

Institute of Oceanographic Sciences
Crossway
Taunton
Somerset

*N A Frederiksen held a NATO fellowship during the course of the study.

PART II

CONTENTS

PART II

ABSTRACT

A field experiment is described in which the movement of non-cohesive sediment by wave action has been studied.   The experiment was carried out at Blackpool Sands, Start Bay, Devon in March 1975.   It was performed outside the surf zone in water of depth approximately 8m.   The dominant feature of the flow field was an incoming swell which was contained in a narrow band of frequencies centred on 0.088 Hz. Significant modulation in the wave amplitude was recorded during the experiment.

Continuous measurements of the fluid velocity were made in the vertical plane in the direction of wave advance for a two hour period.   The horizontal and vertical components of velocity were measured at heights of 30cms and 1m, above the crest of a ripple of wavelength approximately 1m.   This enabled the fluid stress field to be studied.   In addition, an attempt was made to measure the horizontal pressure gradient in the direction of wave advance in order to study its importance at incipient sediment motion.   Observations of sediment transport were made using an underwater television system.   Although sediment movement occurred on the crest of the ripple, the ripple itself was stationary during the experiment.   Since its length was substantially greater than the orbital diameter, it was concluded that the ripple must have been formed previously by more active wave induced flows.

The field measurements were only partly successful.   As expected, since the bed was rippled, incipient motion was found at smaller values of the free stream velocity amplitude than for a flat bed at the same frequency.   Also the zone of comparatively frictionless flow in the main body of the fluid was found to give way to a zone of energy dissipation in the layer adjacent to the bed.   However it was not possible to clearly identify the role of the horizontal pressure gradient in moving sediment, nor was it evident whether transition to turbulent flow had occurred in the boundary layer at incipient motion.   A comparison of the results from the present experiment with results obtained in the laboratory has been made wherever possible.

CHAPTER 1

INTRODUCTION

In Part I of this report (DAVIES and WILKINSON (1977)) a review has been presented
of the existing state of knowledge concerning the movement of non-cohesive
sediment by wave action.   The nature of the wave boundary layer, and any associated
sediment transport, have been the subjects of a considerable amount of theoretical
work and experimental observation in the laboratory, but comparatively little work
has yet been carried out in the field.

The oscillatory boundary layer over a granular bed is poorly understood at present,
and this is particularly so if the bed is rippled.   As yet there is no potential
flow solution for small amplitude waves over a rippled bed, and the boundary layer
could best be defined by departures from such a solution.   Another aspect of the
problem which is not clearly understood is the condition for transition from
laminar to turbulent flow in the boundary layer.   This transition differs for
flat and rippled beds and, for sands, occurs near the threshold of sediment motion.
To study incipient sediment movement, a full understanding of the shear stress
distribution in the flow is needed, accompanied by a knowledge of the instantaneous
velocity profile in the boundary layer through the wave cycle.   In any model of
the instantaneous velocity field, the presence of turbulence in the flow can be
expressed in terms of an effective viscosity.   This is expected to differ from
the molecular viscosity, and to be a function of both height above the bed and
phase angle in the wave cycle.

Unfortunately the information obtained from most laboratory experiments has been
insufficient to answer certain basic questions about the processes involved in
sediment transport by waves.   Such studies have usually involved the generation of
an oscillatory flow at a single frequency over an initially flat granular bed, and
the identification of a "critical" wave capable of producing sediment motion at
that frequency.   The subsequent development of ripples serves to complicate the
flow pattern close to the bed, and hence to both alter the amount of sediment in
motion and require a re-definition of the "critical wave".   In the experimental
work, there has been a lack of attention to the phase angles in the wave cycle
between which sediment is in motion, and this would seem to be fundamental to an
understanding of the phenomenon.   The unsteadiness in the flow is likely to have

2

a bearing on incipient sediment transport since the fluctuating pressure gradients driving the fluid motion will act directly on the grains on the surface of the bed, complementing any drag forces on them arising from the fluid velocity. The instantaneous shear stress in the boundary layer is expected to be directly related to this drag on the bed, although the phase relationship between these two fluctuating quantities is not known at present. The unsteadiness in the flow is known, however, to produce a greater shear stress on the bed than would arise from calculations made on the assumption of a velocity profile of steady logarithmic type in the boundary layer.

In Part II of this report is described a preliminary field experiment designed to study the processes involved in sediment transport by waves. The experiment was carried out at Blackpool Sands, Start Bay, Devon, between 21st and 23rd March 1975. Measurements were made at a position close to the beach but well outside the breaker zone. Tidal currents and the effects of shoaling were, at most, of secondary importance at the experimental site, and the flow near the seabed was due primarily to an incoming ocean swell.

The object of the experiment was to study the threshold of sediment motion in a natural situation in relation to measurements of the fluid velocity and pressure fields close to the sea bed. The phase relationships and critical values of these quantities would provide information on the mechanisms involved. By making velocity measurements at two heights above the bed with two-component EM flowmeters, indications of the velocity profile and the fluid stress fields were obtained. The results were compared with published laboratory measurements of the fluid motion at the threshold of sediment movement and transition to turbulence under oscillatory flow. No attempt was made to relate the measured fluid motion to the deformation of the free surface; this aspect was considered to be outside the terms of reference of the present study.

CHAPTER 2

DESCRIPTION OF THE EXPERIMENT

The principal constraint on the choice of an experimental site was a cable length
of 100m. This was the limiting length for the apparatus existing at Taunton in
1975. Thus a field site had to be selected where there was the likelihood of
finding 'simple' waves (similar to first order small amplitude waves in water of
constant depth) over a sand bed, with vehicular access to within 100m of the
position where the measurements were to be made. These requirements were fulfilled
at Blackpool Sands, Start Bay, Devon. In addition, data gathered in Start Bay
by the Institute in previous years showed that a suitable wave climate probably
existed in March; this determined the dates on which the experiment was carried
out. There were no outcrops of rock or sand bars seaward of the beach to impede
the incoming waves, and the slope of the seabed at 100m from the sea wall was
small. At high tide the rig supporting the sensors was in water of 8m depth on
a coarse sand bed. The rig was positioned on the seabed by divers at a location
where the bed material was formed into ripples of about 1m length.

2.1 Apparatus

The velocity measurements were made using two electromagnetic flowmeters with
10cm discus shaped measuring heads (Colnbrook Electronics ship's log MK1).
These were positioned to measure the horizontal and vertical components of the
fluid velocity at about 30 cms and 1m from the seabed. In order to improve the
performance of the flowmeters,two shielded multicore cables were passed through
1.2cm bore PVC tube; this enabled the small signals from the electrodes on
the measuring head to be well shielded from the much larger signals that powered
the field coils. The flowmeters were attached to a tetrahedral frame, upon
which was also positioned an underwater television camera to view the area of the
bed vertically below the flowmeters. The arrangement of the equipment on the
seabed is shown in Fig 2.1 together with the definition of axes and velocity
components.

In order to measure the horizontal pressure gradient, two FM pressure transducers
(Type NIO/4803) were placed 5m on either side of the rig in the direction of
wave travel. Thus the fluid pressure and an approximation to the pressure
gradient at the point under the flowmeters could be calculated, assuming a small
modification of the wave between the two transducers.

A block diagram of the recording arrangements is shown in Fig 2.2   The two
horizontal and two vertical velocities from the flowmeters were recorded on four
channels of a Bell and Howell FM tape recorder.   As the instantaneous recordings
from the two pressure transducers would be of similar magnitude, it was decided
to record (on two more channels of the same tape recorder) one pressure and the
pressure difference, as computed on line by an operational amplifier subtractor
circuit.   Unfortunately, this circuit failed and the information from the second
pressure transducer was lost (see Section 5.3).   The seventh track was used to
record a timing pulse, a 1 kHz 'bleep' with a repetition period of 1 second.   To
give synchronization, this signal was also recorded on the audio track of the video
tape recorder used for the underwater television.   A pulse counter was connected
to the bleep circuit for the duration of the experiment, and audio fixes were
recorded on both tape recorders at intervals throughout the two hours of recording,
notably at the beginning and end of each video tape.   In addition, a calibration
signal (100 mv pk-pk, 1 Hz sine wave) was recorded on each channel of the B & H
recorder before and after the experiment.   During the entire experiment a six
channel UV chart recorder was used to monitor the signals recorded on tape.

The noise of the flowmeter system was equivalent to a r.m.s. velocity of about 1 cm/sec,
that is about 5% of the maximum wave induced oscillatory velocities.   The
stability of the d.c. offset of the system was low, and this, together with the
lack of field zero information (see Section 4.1) made the determination of anything
but the oscillatory components of velocity impossible.   The pressure transducer
system could resolve to about 1 cm of water, and the tape recorder could reproduce
the recorded signals ($\approx$ 100 mv. pk-pk) to within 1%.

2.2 Deployment of the apparatus
Initially a suitable site for the experiment was selected by the divers.
Flotation buoys were attached to the rig which, after having been manhandled
through the breaker zone, was towed out to the chosen site by a launch and lowered
to the seabed.   The rig was positioned so that the flowmeters were over a ripple
crest and it was oriented in the wave direction by divers using a slightly buoyant
inverted pendulum (to indicate the vertical plane of maximum wave activity).   Its
base was then levelled with the aid of a pair of mutually perpendicular spirit
levels.   Finally, the pressure transducers were carried out from the beach by
the divers and put into position.   The cables which had been flaked out on the
beach to facilitate handling were lashed together, weighted with chain in the

breaker zone, and buried where they passed up the beach. All the electronic equipment was set up in a van parked on the seawall, about 15m from the high tide mark. The power was provided by a small petrol generator.

CHAPTER 3

BACKGROUND INFORMATION

3.1 Introduction

While the experiment was in progress, a certain amount of background information was collected. This consisted of:

(i) The beach profile and bottom topography in the vicinity of the experiment.

(ii) A record of water level during the experiment.

(iii) Sediment sampling at the sea bed in the vicinity of the rig.

(iv) An estimation of the ripple shape (using stereo photogrammetry).

(i) Beach Profile

A traverse was taken down the beach to the water, by chain and level, from an arbitrary datum bench mark of +10.0m on the sea wall. This profile was extended out to sea by echo sounding from the launch, between positions fixed by sextant. The profile is shown in Fig 3.1. The bottom in the vicinity of the experiment can be seen to be fairly flat (1 in 17 slope). Further investigation to seaward revealed neither sudden changes in the depth nor rocky outcrops.

(ii) Changes in water level

Changes in the water depth during the experiment were minimized by working over the peak of the tidal cycle. The approximate depth was measured using a staff and level, as shown in Figure 3.2. The levels for Dartmouth were calculated from the Admiralty Tide Tables.

(iii) Sediment sampling

Observation by divers revealed that the size of sediment varied greatly in the region of the rig. Consequently sediment samples were taken at the crest and in the troughs on either side of the ripple above which the flowmeters were located. The grain size distribution curves (Fig 3.3) show that the material in the troughs was generally coarser than that on the crest of the ripple.

6

3.2 Estimate of ripple shape using Stereophotogrammetry

(i) Method and preparation

In order to quantify any changes in ripple positions or shapes, measurements of profiles of the sand ripple topography over several ripple wavelengths adjacent to the rig were required. These were to be obtained before and after the recording period. In addition, the photographic equipment had to create minimum interference with the flow. Since the equipment available for analysis of the photographs was a Zeiss Jena Stereopantometer, only vertical photographs were acceptable. Visibility limited the 'flying height' to around 1 to 2 metres, and about 6 consecutive overlaps were needed to cover 2 to 3 ripple wavelengths. Since only one camera was available, a suitable apparatus was made to enable the requisite number of overlaps to be obtained without relative tilt. The resulting rig consisted of two frames, as shown in Fig 3.4. The lower frame provided a set of rails that could be adjusted into the horizontal plane, and along which the upper frame, which carried the camera and flash gun, could be moved on wheels between pre-marked positions. The upper frame also carried a pair of horizontal rods for optical calibration (see Analysis method), and two mutually perpendicular spirit levels to ensure that the optical axis was vertical. The two frames were deployed separately,and the camera and flash unit fitted onto the rolling frame underwater after levelling. Three pegs with square tops of known size were also hammered into the seabed in the field of view to provide an extra control for strip comparison, in case the lower frame settled during the experiment.

(ii) Equipment

The photographic equipment consisted of a Hasselblad 5000 camera fitted with a 50mm Distagon lens, enclosed in a Hasselblad underwater housing with a Leitz underwater corrector port designed for a 38mm Biogen lens. The lighting unit was a Sub-sea Strobe wide angle electronic flash gun fitted with an underwater corrector.

(iii) Analysis method

The focal length of the optical system (camera and corrector lens, etc) when underwater had to be calibrated. In order to do this, the pair of rods mentioned above were fastened in the field of view, parallel with the direction of traverse (the x – axis) and separated by 100mm⁻ in the vertical direction. The rods were fixed to the rolling frame, and so were <u>not</u> viewed stereoscopically. However, if the frame was moved 'B' mm (the'camera base'), and two marks on the

7

rods (one vertically above the other) were compared with two more marks B mm away in the x-direction, the 'false stereo effect' could be used.

Referring to Fig 3.5, it can be seen from the similar triangles $o_1 n_1 a_1$, $O_1 GA$ and $O_2 n_2 a_2$, $O_2 HA$, that the x_1 and x_2 coordinates of the image point A can be found in the two photographs. The stereoscopic parallax of point A is the difference:

$$P_A = n_1 a_1 - n_2 a_2 = \frac{F B}{O_1 N_1 - N_1 G}$$

$$= \frac{F B}{H - \Delta \mathcal{l}}$$

where F = focal length of the system*

    B = camera base

    H = distance to the bottom bar

    h = distance between bars

        (and $(H - \Delta h)$ is the vertical distance from the perspective centre to the point A).

Similarly, the stereoscopic parallax of C is:

$$P_c = \frac{F B}{O_1 N_1}$$

$$= \frac{F B}{H}$$

Taking the above two equations, and solving for F and H:

$$F = \frac{\Delta \mathcal{l}}{B} \cdot \frac{P_A P_c}{P_A - P_c} \tag{1}$$

$$H = \frac{F B}{P_c} \tag{2}$$

Similarly, it can be shown that the height 'h' of a general point D with relation to the bottom bar is given by:

$$\mathcal{l} = \frac{F B}{P_D} - H \tag{3}$$

Differentiating Eqn (3) with respect to P_D and taking $H \gg h$, the minimum discernable change in h can be seen to be

$$\Delta \mathcal{l}_{min} = \frac{H^2}{F B} \Delta P \tag{4}$$

*Note: This is an effective focal length during analysis; since the prints off which parallax is measured are 3 times contact size, the true focal length of the system is F/3.

where ΔP is the minimum resolvable difference in parallax.

The horizontal scale 'S' of the photographs at the point D is simply (by similar triangles)

$$S = \frac{\text{distance in photograph}}{\text{distance on ground}} = \frac{F}{H + h}$$

Since 'S' varies over an undulating surface, it is customary to choose a reference plane upon which this surface is projected and the scale is constant. The resolution in the horizontal plane is simply related to the minimum measurable distance on the photographs divided by S.

(iv) Results

Technical difficulties and bad underwater visibility led to full sets of photographs, 'before' and 'after', being obtained only for the second day of the experiment. A stereoscopic pair from this strip is shown in Fig 3.6, and these were analysed by the methods described above. Parallax measurements of the points on the calibration rods gave (from Eqns. (1) and (2)) values for the focal length of 159.7mm, and for the distance from the perspective centre to the bottom calibration bar of 879mm. The reference plane was chosen at 1278mm from the perspective centre, giving a scale of 0.125. The minimum height resolution was found from Eqn (4) to be 3.4mm (camera base B = 300mm, parallax resolution P = 0.1mm). The horizontal resolution at the scale used was 0.8mm. It must be noted that these considerations do not take into account either distortion due to stretching of photographic prints, or lens aberration.

Micrometer parallax readings were taken from each overlap on a profile line through the ripples. A plot of plan points and heights along the profile line was made together with conspicuous detail, e.g. stones, which helped to locate the profile from overlap to overlap. The profiles were then compiled to give two long profiles along the same line, one before and one after the experiment (see Fig 3.7). Comparison of the two profiles showed that the topography had not changed. Thus even if sediment movement had taken place, it did not change the shape of the sea bed. As the wave conditions apparently had not changed from the previous day, it suggests that the ripples were of constant shape during the first day of the experiment also.

9

A contour map was also produced from a sample pair of photographs by two operators in order to assess the capabilities of underwater photogrammetry. These agreed within the accuracy of the system.

(v) Discussion

Visibility in British coastal waters is typically between zero and 10m. This severely restricts the 'flying height', which in turn limits the height resolution and ground coverage per photograph. The situation is not alleviated by additional lighting, as the poor visibility is due to suspended matter in the water, not to the lack of ambient light. An increase of the light level leads only to increased backscatter and a lack of contrast. Thus large scale surveys would require a prohibitive number of photographs, unless exceptionally clear conditions prevailed.

Although the technique did yield the required information for this experiment, the apparatus on the sea floor would have been much simplified if a more sophisticated plotting maching (capable of dealing with tilt etc) had been available. Furthermore, when a stereo pair of photographs is not taken simultaneously, moving sediment (either on the bed or in suspension) obviously appears at different points on the two negatives; this can create an apparent laek of focus and/or false parallax conditions which can be totally confusing to the plotter. Thus stereo photogrammetry under these conditions requires simultaneous exposure of each stereo pair.

CHAPTER 4

ANALYSIS METHODS

The experiment provided continuous data over a two hour period. This consisted of analogue tape recordings of two horizontal and two vertical velocities and the pressure in the vicinity, together with a video tape recording of an area of the sea bed beneath the flowmeters.

4.1 Calibration of the recording system

The analogue voltage levels recorded in the experiment were dependant on the gain of the tape recorder and also contained DC offsets. In principle, on a particular recording channel, these two quantities are arranged to make the most efficient use of the equipment and are determined accurately by recording calibration

signals during the experiment. The DC offset of a pressure record is not required, as the shore unit in conjunction with the pressure transducer effectively high pass filters the signal at approximately 0.01 Hz. However it is necessary to obtain the DC offsets of the velocity records, since, for example, absolute velocities are required for successful calculations of the Reynolds stress (see Appendix I). The DC offsets of an EM flowmeter system for zero flow conditions are generally established in the field by placing a shroud over the flowmeter head. In the present experiment, the volume of water trapped around the EM heads was too small, and only the fluctuating components of velocity were subsequently available for analysis.

The voltage output of the tape recorder (disregarding the DC effects) can be expressed for the lower horizontal velocity, for example, as:

$$V_2(t) = k_{\ell x}\, G_2\, U_\ell(t)$$

where $U_\ell(t)$ = horizontal velocity at the lower flowmeter (cm sec^{-1})

$k_{\ell x}$ = sensitivity of the 'x' channel of the lower flowmeter (volts cm^{-1} sec)

G_2 = gain of channel 2 of the tape recorder

The sensitivities of the instruments were found by laboratory calibrations; namely by standard towing techniques for the flowmeters, and pressure tests for the wave recorders. The gain of the tape recorder was found by replaying the calibration signal recorded on each channel before and after the experiment. During the analysis for the threshold of sediment motion, the analogue records were replayed onto a UV chart recorder, and measurements were taken off the chart. The calibration signals were also replayed enabling the gain of the chart recorder to be ascertained.

4.2 The analysis of sediment motion

An objective of the experiment was to determine the values of the fluid velocity when sediment motion stopped and started in both shoreward and seaward directions. This study required the times of occurrence of the different instances of grain motion from the video tapes and a comparison with the EM flowmeter results. To this end three three-way 'motion indicator switches' were made up to apply either +1v, -1v or 0v to the Uv chart recorder. The video tapes were then replayed and three observers (each equipped with a motion indicator switch) recorded their opinions of the instants of the stopping and starting of sediment motion in

11

each direction. One channel of the UV recorder was used to display the audio
'bleep' from the sound track on the video tape (see Chapter 2) to enable the
critical times to be established. An example of the resulting chart is shown
in Fig 4.1. To relate these results to the flow measurements, the three sets
of critical times were averaged, and the average trace was superimposed on another
UV chart upon which the velocity and pressure records had already been replayed.
From this second chart (see Fig 4.2) all the variables were calculated at the
critical times, with respect to their means over the two hour period. It was
convenient to assign a code to the sediment motion events such that α and Ω
represented the starting and stopping of motion respectively and '+' and '-'
indicated the shoreward and seaward directions respectively.

All the critical times together with the corresponding values of the velocities
and the pressure were processed on a PDP11 computer, in order to calculate, for
example, the mean horizontal velocity at the start of motion in the shoreward
direction $(+\alpha)$ as measured by the lower flowmeter. For all such quantities,
the distribution of the measured values around their mean was found to be
approximately Gaussian and so the standard error was calculated in the usual way.
The data was then divided into succeeding 10 minute intervals, and the number
of instances of motion and the length of time of grain motion in each interval
were computed. This procedure was repeated with an interval length of 5 minutes.
Finally the same process was carried out on a set of data reduced in such a way
that instances of motion were retained for analysis only if the time interval
between the initiation of motion and the preceding cessation of motion exceeded
a certain specified value, ΔT. This procedure, aimed at studying differences
in threshold values caused possibly by a 'settling of the bed' during a period of
no grain motion, was repeated for various values of ΔT.

4.3 Time series analysis of the analogue data
The analogue velocity and pressure data recorded on the magnetic tape was
digitized and then examined in succeeding 10 minute portions with a view to
assessing changes in the flow conditions through the experiment. The magnetic
tape was replayed through low pass filters (6 pole 0.01 dB Tchebychev low pass
filters with a 3dBpoint of 3.5 Hz). The signals were then passed into a four
channel analogue to digital converter (ADC : DEC type AD01) controlled by a
PDP8 computer. The digitization rate was set at 5Hz which was sufficiently high
to avoid aliasing. The ADC was operated with 2048 fixed quantizing levels

(the increment between levels being $\Delta \approx 1.22\text{mv}$ after digitization), and the
output was in binary form (10 bit plus sign).

As the output of the tape recorder was 100 mv pk-pk, only about 80 of the levels
were used. BENDAT and PIERSOL (1971) indicate that the quantization error has a
uniform probability distribution, and thus a standard deviation of about 0.29Δ
In the present case, therefore, the error introduced by digitisation has a
standard deviation of about 0.35 mv ($\approx 0.3\%$ of the pk-pk signal). This is
unlikely to be of any importance in comparison with other errors (see Section 2.1).

Each 10minutes of digitisation resulted in groups of 3000 digitised values on
each of 4 channels. Each group was transferred from the PDP8 magnetic tape to a
data file on magnetic disc on a PDP11 computer by means of a standard library
routine. At this stage the quality of the data was checked visually by
examination of a microplot of each data file. Two clearly identifiable types
of error were found. Firstly it was evident that on one of the ADC channels two
of the quantization levels were not working. A subroutine was written to find
the rogue values, and replace them with linearly interpolated ones. Secondly,
large 'spikes' were found occasionally in the velocity data. These were
assumed to be produced by a malfunctioning of the EM flowmeter electronics.
Normally these spikes, which were isolated and occurred in the middle of otherwise
'clean' data, were removed manually and replaced by an interpolated value. In
certain cases, a number of spikes appeared in rapid succession, and it was found
that these could be removed by the use of a low pass digital filter. (An
isolated spike merely suffered a reduction in its magnitude when passed through
this filter, due to its frequency composition). The digital filter was designed
to cut off between 1 and 1.25 Hz, and its 30 coefficients were evaluated using
the NIO Library Programme 158, 'HILOW'. All the data files were passed through
this filter, thus removing all energy in the data at frequencies above 1.25 Hz,
(which is equivalent to half the Nyquist frequency). Although no reference
could be found to the problem in the literature, it was considered unlikely that
the 10cm EM Flowmeter heads could respond hydrodynamically to velocity changes
at frequencies greater than 1 Hz. Therefore it was concluded that no useful
information would be lost by the filtering procedure. The processed files were
stored on disc.

The quality of the data also gave concern at very low frequencies. Despite

there being no absolute velocity zero available (see Section 4.1), it was hoped that residual velocity trends could be calculated from long term means. However, mean values calculated from 5 and 10 minute blocks of data showed no consistent trends. It was concluded from this that the long term stability of the equipment left something to be desired, and it was decided to reduce each data file to a zero mean before using it further. While this procedure did not introduce significant errors into the examination of certain quantities such as the wave energy, it most certainly casts doubts upon Reynolds stress values calculated. This aspect is treated fully in the Appendix.

The energy content of the signals was investigated by computing their variances, group by group, and the frequency composition of these variances was studied using standard spectral analysis techniques. A fast Fourier transform (FFT) method was used to produce a continuous function passing through the 3000 data points of the group under analysis. The NIO Fortran Library Program 134, 'FFT', was used over the 10 minute data sets, the output consisting of the sine and cosine coefficients at the 1501 harmonics of the Fourier series (including the 'zero frequency'). The harmonics were equally spaced between 0 and 2.5 Hz, the Nyquist frequency. By squaring and adding the pairs of coefficients, the contributions to the variance at the discrete frequencies were obtained. The contributions contained in groups of 5 adjacent harmonics were next averaged; five harmonics per group were chosen in order to preserve sufficient frequency resolution, whilst achieving an acceptable confidence interval around the grouped estimates. For this choice of 5 harmonics and a grouped estimate of, say, E in any one of the resulting broader frequency intervals, the 80% confidence limits were as follows: lower limit 0.62E, upper limit 2.0E. Spectral estimates with these confidence limits were obtained every 1/120 Hz in the frequency domain.

Further use of the FFT was made in obtaining cross spectra from two simultaneous data sets (see RAYMENT (1970) for a simple exposition of the details of obtaining a cross spectrum from the output of an FFT). The procedure adopted again involved smoothing the cross spectra by taking groups of 5 adjacent harmonics. The cross spectrum is of complex form, and is often represented in terms of the co- and quad-spectra, its real and imaginary parts respectively. The co-spectral estimates are the average products of the two data sets at particular frequencies, such that the sum over all frequencies is the co-variance. The quad-spectrum is

14

of a similar nature, except that one data set is shifted in time by a 90° phase angle at each frequency of interest, prior to the product being formed.

Finally, a computer programme was developed to obtain auto- and cross-correlation functions. The former display the dependance of values at one time in a given data set on values at another time, and may be used to detect periodic data masked in a random background. The latter give a description of the dependance of the values of one data set on those of another set at various time lags. Time delays in a system may be established in this way, but if transmission through the system is frequency dependent, the interpretation of the cross-correlation function is complicated, and cross spectral analysis is usually of more value. The correlation functions were found in the simplest possible way, the lagged products being formed before averaging (by division by the number of possible products) and normalizing to give the normalized correlation function at a particular time delay. This method was tedious, but it did give the true correlation function, and not a circular approximation to it. It was found that the computation could be shortened by using only the odd or even members of the data sets, and by using integral arithmetic to avoid unnecessary accuracy.

CHAPTER 5

RESULTS
5.1 Introduction
The analysis was carried out in two stages: firstly, a study of the threshold of sediment motion and, secondly, a time series analysis of a portion of the analogue data. Only data recorded during a two-hour run on the first day of the experiment was used, as this was thought to have been the best obtained. The study of the threshold of motion was conducted using the record on the video tape. This consisted of a view of the area of the sea bed vertically below the heads of the EM flowmeters. In the centre of the screen of the television monitor could be seen the crest of a ripple, and, along this crest, individual sand grains could be detected for a distance of about 0.5m. The length of the ripple (trough to trough about 1m) was also visible, the sand on the ripple crest giving way to much coarser material in the troughs on either side of it. Under the experimental conditions, the sand on the ripple crest remained stationary for most of the time. Sediment movement was observed only occasionally and it was usually associated with the arrival above the ripple of a group of higher amplitude surface waves. The motion of individual sediment grains could be

detected quite clearly on the television screen and it was decided that this visual data was of a sufficiently high quality for an analysis to be conducted on the threshold of sediment motion.

5.2 The threshold of sediment motion

Observation of video tape records of the sea bed indicated 396 occurrences of sediment motion during the two hour experiment.   The distribution of these occurrences in succeeding 10 minute intervals through the experiment is shown in Table 5.1; the values marked with an asterisk are scaled values for intervals in which the video record was incomplete for some reason.   The total time during which sediment motion took place is classified in the same manner in Table 5.1.   The variability in both the total number of instances of motion and the total time of motion in succeeding intervals is evident.   It is shown later that this variability can be associated with the changing wave conditions which were experienced during the experiment.

Associated with each of the 396 occurrences of grain motion were four values of velocity and one of pressure, at the instants of both starting and stopping of motion.   As described in Chapter 4, these values were sorted into four groups of starting and stopping in the shoreward and seaward directions, and their mean values, standard deviations and standard errors were calculated, as shown in Table 5.2 .

A pattern is clearly discernable in some of these results, in particular the results for u_l and u_u .   Considering, initially, the mean values of u_l and u_u , it is clear that at threshold (α), the current speeds in the '+' and '-' directions are approximately equal.   The higher values obtained at the upper flowmeter indicate either wave attenuation or the fact that the lower flowmeter was in a layer where boundary effects were of importance.   The standard errors for the α values show that the differences in the threshold values in the '+' and '-' directions have no statistical significance (within 95% confidence limits). This suggests that the asymmetry introduced by an overall slope of the beach of 1 in 17 (see Figure 3.1) did not significantly enhance sediment motion seawards.   The $\bigwedge$ values of u_l and u_u indicate smaller speeds at termination than at initiation of motion.   This suggests the persistence of grain motion after the current speed had fallen below the initiation threshold value, possibly as a result of the inertia of the grains in motion.   No pattern

16

Interval Number	Seaward (−)	Shoreward (+)	Total
1	25	29	54
2	8	8	16
3	13	13	26
4	9	11	20
5	22 *	21 *	43 *
6	18	20	38
7	24	22	46
8	7	11	18
9	18 *	18 *	36 *
10	17	20	37
11	22 *	22 *	44 *
12	20 *	23 *	43 *
13	11	14	25

Instances of Motion

Interval Number	Seaward (−)	Shoreward (+)	Total
1	64.9	59.8	124.7
2	11.4	15.3	26.7
3	24.9	25.4	50.3
4	13.9	14.7	28.6
5	50.6 *	46.9 *	97.6 *
6	32.9	41.6	74.5
7	50.9	48.7	99.6
8	10.7	16.6	27.3
9	39.5 *	42.0 *	81.4 *
10	30.4	44.6	75.0
11	38.6 *	36.6 *	75.3 *
12	43.1 *	46.9 *	89.9 *
13	17.1	22.3	39.4

Total time of motion in seconds

TABLE 5.1

Variable	Class of Motion			
	$-\alpha$	$-\Omega$	$+\alpha$	$+\Omega$
W_{L} cm/sec Mean St.dev. St.error	1.25 1.06 0.08	0.39 1.20 0.08	−1.22 1.25 0.09	0.27 1.26 0.09
U_{L} cm/sec Mean St.dev. St.error	−14.84 7.98 0.56	−9.11 7.67 0.54	15.13 7.45 0.53	12.02 7.65 0.54
U_{v} cm/sec Mean St.dev. St.error	−16.48 7.93 0.56	−9.37 8.69 0.61	16.23 7.67 0.54	11.79 8.24 0.58
p_{2} cms H_2O Mean St. dev.	− 6.15 6.64 0.47	−7.80 4.53 0.32	3.81 5.43 0.38	6.50 4.87 0.34

Terminology:

α : initiation of motion; Ω : termination of motion

+ : shoreward direction; — : seaward direction

Threshold results ΔT = 0 secs

TABLE 5.2

at all is evident in the w_L values; indeed, the standard deviations here exceed the mean value in three out of the four values tabulated. Finally, in assessing the results for the pressure p_2 (the only pressure signal recorded successfully), it must be recalled (see Fig 2.1) that this quantity was measured at a distance of 5m shorewards in the direction of wave travel from the point at which sediment motion was observed, and, therefore, these results cannot be viewed in the same way. (For completeness, the same method was applied to a data set consisting of the instantaneous values of the product $u_L w_L$. Perhaps predictably, in view of the results described above, this yielded no useful information (see also the discussion in Chapter 6.4)).

The next step was to perform exactly the same analysis on reduced sets of data. The criterion adopted in establishing these reduced sets was that the time between an Ω value and the next α value should exceed ΔT seconds (Section 4.2), thus possibly enabling the bed to "settle", and thereby to become more resistant to subsequent erosion. The results for ΔT = 5 seconds are shown in Table 5.3. Here an increase in the threshold values in u_L and u_U is evident compared with Table 5.2, suggesting that the "settling" of the bed may have a significant effect on threshold values. However, it is not possible, on the basis of results from the present experiment, to draw any firm conclusions on this point since the effects of pressure gradients in the flow, and of phase differences between the fluid velocity close to the bed and in the free stream cannot be assessed. These effects may combine to produce a more complicated stress distribution at the surface of the bed than can be ascertained from simple considerations based on critical values of the horizontal velocity at some reference height above the bed.   The first motion criterion has been varied through different values of ΔT and the picture which emerges, for the typical case of u_L (negative), is shown in Figure 5.1. For current speeds at threshold (α), a sharp increase can be seen for $0 < \Delta T < 3$ secs, but, thereafter, no further statistically significant increase is found. Standard errors are indicated by vertical bars, and a statistical test (the t-Test for the Two Sample Case, DAYTON and STUNKARD (1971) has been used to show that the mean values obtained for u_L in 2 secs. $\leqslant \Delta T \leqslant 15$ secs are different from the overall mean value ($\Delta T = 0$) within 95% confidence limits. On the other hand, the mean Ω values indicating termination of motion, display no such trend as ΔT is varied, for these values, the t-test indicates that none of the mean values in 1 secs $\leqslant \Delta T \leqslant 30$ secs has arisen from a population having a

17

Variable		Class of Motion			
		$-\alpha$	$-\Omega$	$+\alpha$	$+\Omega$
W_L cm/sec	Mean St.dev. St.error	1.46 1.06 0.08	0.40 1.10 0.08	-1.19 1.24 0.09	-0.21 1.19 0.09
u_L cm/sec	Mean St.dev. St.error	-17.94 5.85 0.43	-8.41 8.03 0.60	17.18 6.42 0.48	10.57 7.79 0.58
u_v cm/sec	Mean St.dev. St.error	-19.41 6.12 0.45	-8.44 9.19 0.68	18.17 6.64 0.49	10.11 8.56 0.64
p_z cms H_2O	Mean St.dev. St.error	- 8.87 5.99 0.44	-7.99 5.22 0.39	5.63 4.89 0.36	6.78 4.36 0.32

Terminology:-

α : initiation of motion; Ω : termination of motion

+ : shoreward direction;   — : seaward direction

Threshold results ΔT = 5 secs

TABLE 5.3

different mean value from the overall mean at $\Delta T = 0$, again within 95%
confidence limits. Whether, as seems possible, these results do indicate a
"settling" of the bed and an increase in its resistance to erosion the longer it
remains undisturbed, or whether the processes involved in the initiation
of grain motion are more complicated than this, is a question which will only
be settled by future detailed investigations of the nature of the bed shear
stress and the role of the pressure gradient. At present, it can be stated
only that an increase in ΔT is associated with an increase in the threshold
velocity, while the corresponding values for the termination of motion show
no such dependence on ΔT.

It is important to stress here the subjective nature of the threshold analysis,
since it is possible that this may have had a bearing on the results described
above. Generally there was reasonable agreement among the observers operating
the system of switches as to the occurrence of sediment motions. However the
identification of the time of termination of motion was apparently much more
difficult than that of initiation of motion, judging by the scatter in the
estimates prior to averaging in a number of cases. On the few occasions when
two of the observers detected some slight grain motion while the third did not,
a majority decision was taken. In the matter of the "settling" of the bed, the
possibility must be admitted that the longer a grain remained stationary the
slower were the reactions of the observers when it eventually moved. It is
to be hoped that a more quantitative means of assessing grain motion will emerge
in the future.

5.3 Time Series Analysis

Wave conditions through the experiment displayed a variability which has
been assessed by calculating the variances of the basic quantities in the analysis
over successive 5 and 10 minute periods.   This variability was associated
with the amount of grain motion as observed on the underwater television.
In order to display this point, the number of instances of motion in a given
10 minute interval (Table 5.1) is plotted against the variances of both u_L
and p_L in Figure 5.2.   There is clearly an increase in the number of instances
of motion with variance in both cases.   The scatter in the results merely
indicates that the variance is only a crude measure of wave intensity for the
present purpose and does not bear any direct relationship to sediment transport.
A similar pattern was found with w_L and u_v , and also with variances measured

18

over 5 minutes. However the scatter in the points was more marked over the shorter interval.

The co-variances of u and w were calculated for both the upper and lower flowmeters over 10 minute intervals. Noting that $\tau_t = -\rho_f \, \overline{uw}$, where τ_t is the turbulent shear stress and ρ_f is the fluid density, it can be seen that the $\overline{uw}$ value for a 10 minute interval is proportional to the residual stress at the measuring point, on a plane which is defined by the orientation of the electrodes of the EM flowmeter. This plane is orthogonal to the vertical plane lying in the direction of wave travel. In the present analysis it has not been possible to define adequately the plane on which the stress has been measured since the absolute velocity zero was not determined. (Some general discussion on this topic can be found in the Appendix. It follows that the results quoted in Table 5.4 can only be taken as a rough qualitative guide to relative stress levels at different positions in the flow. Positive values in the table represent a residual onshore stress but, possibly, the only significance in the results presented is the ratio of the stresses at $\approx$ 1m and at $\approx$ 30 cms above the bed. On average, over the 13 pairs of values tabulated, this ratio is such that the stress at $\approx$ 1m is smaller than the stress at $\approx$ 30 cms by a factor of 0.12 (with a standard deviation of the ratio of 0.08). Performing the calculation using 5 minute intervals leads to approximately the same value for the ratio. Above the $\approx$ 1m level it might be expected that, in the absence of any residual flows, the stress decreases further. In the situation of the free stream being a potential flow, the residual stress would, of course, be zero. LONGUET-HIGGINS (1959) has shown that at the upper edge of both laminar and turbulent bottom boundary layers, the residual stress due to progressive surface waves is non-zero and in the direction of wave travel. This stress is associated with residual mass transport velocities. The results presented in Table 5.4 suggest a residual stress at both 30 cms and 1m above the bed in the opposite direction to this. However it would be wrong to draw even general qualitative conclusions on the basis of a doubtful set of stress values.

The next step in the analysis involved the determination of the frequency composition both of the variances of the basic quantities u_L , w_L , etc, and of the co-variances $\overline{u_L w_L}$, $\overline{u_u w_u}$. The frequency spectra were computed by the Fast Fourier Transform (FFT) method described in Chapter 4. This operation enabled the waves to be characterized according to frequency, and also, crudely, to be separated from any "background" turbulence present. In Figs 5.3 and 5.7

Interval Number	Height of measurement position from bed	
	30 cms	1 metre
1	-10.43	-1.32
2	- 4.86	-0.89
3	- 6.84	-0.32
4	- 6.11	-0.51
5	-10.65	-0.39
6	-10.80	-2.12
7	- 8.75	-1.20
8	- 5.59	-1.14
9	-10.98	-1.66
10	- 7.39	0.27
11	- 8.61	-1.90
12	- 9.06	-1.67
13	- 5.94	0.13

Residual stress ($\tau_t = -\rho_f \overline{uw}$) in each 10 minute interval in dynes/cm^2

TABLE 5.4

are displayed typical data sets for which spectra have been obtained. The traces
are continuous in time from left to right and from top to bottom, each figure
containing 10 minutes of data. The signal is drawn about its mean (during the
interval), the vertical scale being fixed by normalizing the values by the maximum
deviation from the mean in each case. The variances of the data are given in
the captions to Figs 5.3 to 5.7. Periodic fluctuations about the means are
evident on all five channels, but the higher frequency noise apparent in the
traces for W_L and W_U is a result of the more sensitive scales due to the low
signal variance.

The spectra corresponding to the five traces are displayed in Figs 5.8 - 5.12.
Each spectrum is dominated by a single peak centred on 0.088 Hz, corresponding
to waves of 11.4 secs period. Relatively little activity is found at frequencies
above 0.3 Hz. The dominance of the single peak thus provides convincing evidence
that the flow conditions were the result of a single wave train. The similarity
between the spectra of both u_L and u_U, and p_2 can be interpreted in the
following way. A spectrum of a pressure fluctuation such as p_2 is not expected
to reflect more than the wave induced part of the flow field, as any turbulence
induced pressure fluctuations are of a smaller order of magnitude. The spectrum
of the directly measured velocity field, however, contains information about
wave-induced and turbulent velocities present. This fact has been exploited by
SEITZ (1971) in an analysis of observations made in an estuarine flow. No
analysis along the lines proposed by Seitz, involving the use of small amplitude
wave theory to link the pressure and velocity fields, has been undertaken here.
However, the qualitative similarity between the spectra of p_2 and u_L (or u_U)
suggests that the velocity field is very probably wave-induced and contains
little turbulence. It can be concluded, therefore, that the flow during the
typical 10 minute interval displayed in Figs 5.3 - 5.7 was dominated by wave
action at a discrete frequency and that little other significant fluid motion
was present.

The digitized data from Figs 5.3 to 5.6 is presented in the form of normalized
probability density functions in Figs 5.13 and 5.14, and the normalized Gaussian
curve is included for comparison. In neither of the figures is the characteristic
distribution for a sine wave evident. The signal can best be described as narrow
band random noise (see BENDAT and PIERSOL (1971)), which is consistent with the
wave group behaviour noted in the velocities and the pressure measured during the

experiment.   The distribution of all four velocity components can be seen
to be approximately Gaussian.

The division of the flow into wave induced and turbulent components can, in
principle, be studied by means of a cross-spectral analysis of u_L and w_L ,
and u_u and w_u .   The Reynolds stress is directly proportional to the co-
variance of u and w , and the 'co-spectrum' shows the frequency composition
of this co-variance.   In other words, the co-spectrum indicates the frequency
composition of 'in-phase' components of the fluctuating quantities u and w ,
and these in-phase components are generally associated with energy dissipation
in the flow.   On the other hand, 'out-of-phase' components, such as are found
for u and w in the velocity field under small amplitude inviscid waves, give
expression to that part of the flow field in which no energy dissipation is
taking place.   The frequency composition of this frictionless part of the
flow field is expressed in the 'quad-spectrum'.   In Figs 5.15 and 5.16 are shown
traces of the instantaneous products $u_L w_L$ and $u_u w_u$ during the same period
of time as that in Figs 5.3 to 5.7.   These are the products of the fluctuating
components of velocity and have been plotted about their own means to arbitrary
vertical scales as before.   (Note that even though the signals u and w
used for this calculation have a zero mean, the resulting product does not.)
The trace of $u_L w_L$ is rather different in appearance from that of $u_u w_u$;
in particular, there is an intermittency in the occurrence of large values of
the product in the case of $u_u w_u$, which is not evident in $u_L w_L$.
It is recalled, from Table 5.4, that the computed values of stress $\left(\propto \overline{uw} \right)$
for the first 10 minute interval were -10.42 and -1.32 dynes cm^{-2} at the lower
and upper flowmeter positions respectively.   It is interesting initially to
note the composition of these mean values in terms of the distribution of the
instantaneous values calculated, and for this purpose probability density
functions have been plotted in Fig 5.17.   In the case of the values at $\approx$ 1m
the distribution of the instantaneous values is approximately symmetrical about
the computed mean.   However, in the case of the values at $\approx$ 30 cms, a long
'tail' is evident in the negative stress direction and there is little symmetry
about the mean.   The values in the 'tail' will, of course, make relatively
important contributions to the total stress.   Neither of the probability
densities displays the approximately Gaussian behaviour seen, in Figs 5.13 and
5.14, in the composition of the basic signals u_L , w_L , etc.   Still less
is there any evidence of a distribution characteristic of a sine wave in the
product at either level.   (The product of two sine waves in quadrature, as found

21

in a simple Airey model of a potential flow under small amplitude waves, is a sinusoidal function at twice the wave frequency).

The cross spectra of u and w at the two levels are presented in Figs 5.18 and 5.19. At both levels the co- and quad-spectra are dominated by a peak at 0.088 Hz, as were the individual signals u_L , w_L , etc, and, again, little contribution is made to either the co- or quad-spectrum at frequencies greater than about 0.3 Hz. The results at $\approx$ 30 cms above the bed show a dominance of the in-phase components in the co-spectrum over the out-of-phase components in the quad-spectrum. The ratio of the cross-spectral estimators integrated over the full frequency range was 3.8 : 1.0 at this level. This suggests the dominance of the dissipative part of the water velocity field over the non-dissipative part. At the $\approx$ 1m level the opposite appeared to be the case, for here the ratio of the integrals of the estimators was 1.0 : 6.8. No undue importance should be attached to the magnitudes of these ratios, but they do suggest that the velocity field away from the bed has more the character of potential flow than close to the bed where a zone of energy dissipation is found. This pattern was repeated in all the 10 minute intervals studied.

Auto- and cross-correlation functions were also computed. The most important use made of these functions was in examining the pressure data. In particular, an attempt was made to use the recorded pressure p_2 and pressure difference $(p_1 - p_2)$ to reconstitute p_1 . The cross-correlation function of the two pressures was calculated in order to find the time lag between them (the time of travel of the wave between the two transducers), and the value of the correlation coefficient at this time lag was also calculated, giving an indication of the degree of modification of the wave during its passage between the transducers. In addition, the variance of p_1 was calculated and compared with that of p_2. The results of these calculations indicated that some mistake had been made during the recording of $(p_1 - p_2)$. The time lag between the two pressures suggested an unrealistically fast wave speed (orders of magnitude different to that calculated from small-amplitude theory) and the variance of the reconstituted pressure signal was wildly different from that of p_2. Initially it was hoped that some simple error had been made, and that the results were still recoverable, but unfortunately an extensive investigation showed this not to be the case. The amplitude of the fluctuating pressure gradient, $\partial p/\partial x$, during the experiment was estimated to be 0.5 (cms of water)/metre, using p_2 and a phase speed calculated on the basis of small amplitude wave theory. However it was not

22

possible to estimate $\frac{\partial p}{\partial x}$ from p_2 for the purposes of the threshold of motion study described in Section 5.2, since the pressure was recorded 5m away from the point where the sediment motion was observed.

CHAPTER 6

DISCUSSION AND CONCLUSIONS

6.1 Comparison of threshold velocity results with previous work

In making even the most simple comparisons between the results from the present experiment and other work, we run almost immediately into a number of fundamental difficulties.   In the first place, the values of velocity quoted in Chapter 5 were obtained in the sea above the crest of a ripple.   Furthermore, the waves measured during the course of the experiment were in all probability not responsible for the formation of this ripple in the first place.   This is the typical situation found in the sea, and, unfortunately, it means that laboratory results on the incipient motion of a rippledbed are probably not directly relevant. Secondly, recalling the discussion in Part 1 of this report (DAVIES and WILKINSON (1977)), it is important to note that all laboratory work on incipient motion has been carried out with a simple monochromatic wave train, whereas in the sea we find the wave energy spread through a band of frequencies.   Although in the present experiment this band was narrow and centred upon 0.088 Hz (Figs 5.8 – 5.12), the waves were not truly sinusoidal (Figs 5.13 and 5.14);   each was different to the one preceding it, the wave ampltiude varying considerably with time. This resulted in some waves causing sediment motion and some not.

It is clear, therefore, that the immediate difficulty arising in relation to incipient motion tests in the laboratory, is the lack of a good basis for comparison with the present set of results.   The "critical wave" for sediment motion (discussed in Part I, Section 3.3) is not readily available in nature, and there is little justification for comparing the peak velocity in the "critical wave" from the laboratory, $\overline{U_\infty}\Big|_{max}$, with our instantaneous threshold velocity values, $u_\wedge\Big|_\kappa$ and $u_\vee\Big|_\alpha$, occurring at some phase in the cycle.   The results, quoted in Tables 5.2 and 5.3, are neither of velocity amplitude, nor were obtained above a flat bed.   Despite this, a comparison will be made with laboratory results on the assumption that $\overline{U_\infty}\Big|_{max} = u_m$, where $u_m = \frac{1}{2}\left\{\left|u_\vee\right|_{+\kappa}\right| + \left|u_\vee\right|_{-\alpha}\right|\right\}$ is adopted as the appropriate critical velocity amplitude at the upper flowmeter, approximately 1m above the ripple crest:

$$U_m = 18.8 \text{ cms/sec} \qquad \text{for "first motion" } (\Delta T > 5 \text{ secs})$$

$$U_m = 16.4 \text{ cms/sec} \qquad \text{for "general motion" (all } \Delta T)$$

In the calculations we have taken D = 0.1 cms; this is the smallest value of representative grain size which can reasonably be adopted on the basis of the grain size analysis (see Chapter 3). We have taken also the dominant wave frequency as ω = 0.088 Hz (or 0.552 rads/sec), and $\gamma \equiv \dfrac{\ell_s - \ell_f}{\ell_f} = 1.65.$

(i) Comparison with Bagnold's formula

This has been taken from BAGNOLD (1946) and has been used in the form

$$\frac{\omega^{1/4} \left[\overline{U}_\infty \big|_{max} \right]^{3/4}}{\gamma^{1/2} \, D^{0.325}} = 21.5 \qquad (\text{in c.g.s. units})$$

Making the substitutions given above

$$\overline{U}_\infty \big|_{max} = 37.5 \text{ cms/sec}$$

Our threshold velocity U_m is about half this, despite the fact that Bagnold's formula is supposed to be valid for the grain size, the frequency of oscillation and the fluid velocity amplitude in question. We note here Bagnold's claim that his boundary layer conditions were essentially laminar when incipient motion occurred. The transition to turbulence is discussed later.

(ii) Comparison with Manohar's (1955) formula (for turbulent flow)

This has been taken in the form

$$\frac{\overline{U}_\infty \big|_{max}}{(\gamma g)^{0.4} (\nu D)^{0.2}} = 8.2$$

from which it follows that

$$\overline{U}_\infty \big|_{max} = 40.6 \text{ cms/sec}$$

Although our grain sizes and operating conditions supposedly permit the use of MANOHAR's formula, again threshold motion occurs for considerably smaller U_m than predicted by the laboratory work. We note here the doubt which has been expressed in the literature (eg EINSTEIN (1972), SLEATH (1974)) as to whether Manohar's experimental conditions were truly turbulent.

24

P.24, at the end of para 1

Insert 'where ℓ_s and ℓ_f are the densities of the sediment and fluid respectively'.

(iii) Comparison with the formula of CHAN, BAIRD and ROUND (1972)

We include this calculation, even though the authors' only performed experiments with D < 0.11 cms, and with frequencies between 0.4 and 1.4 Hz, because the stroke was such that large fluid velocities were achieved. We have taken the formula as

$$\frac{\omega^{1/3} \left[\overline{U}_\infty \big|_{max} \right]^{2/3}}{(\gamma_g)^{1/2} \, D^{1/6}} = 0.52$$

which, with our values, gives

$$\overline{U}_\infty \big|_{max} = 72.4 \text{ cms/sec}$$

Thus the pattern found in the two cases above is again repeated.

(iv) Comparison with the formula of KOMAR and MILLER (1973)

On the basis of the experimental results of RANCE and WARREN (1968) these authors have proposed an incipient motion condition of the form

$$\frac{\omega^{1/4} \left[\overline{U}_\infty \big|_{max} \right]^{7/4}}{\gamma_g \, D^{3/4}} = 1.45 \text{ for } D > 0.05 \text{ cms}$$

In this case

$$\overline{U}_\infty \big|_{max} = 34.2 \text{ cms/sec}$$

Also, from KOMAR and MILLER's separate graphical presentation of incipient motion results, it has been shown that the critical experimental value of $\overline{U}_\infty \big|_{max}$ is approximately twice the value (u_m) found in the present study. Finally, it should be added that if a larger grain size than D = 0.1 cm had been adopted in all of the comparisons made, the discrepancies between $\overline{U}_\infty \big|_{max}$ and u_m would have been enhanced. Some of the possible reasons for the discrepancies have been discussed earlier in this section and also in Part 1 (Section 3.3(i)) with reference to SILVESTER and MOGRIDGE (1970).

We note next the connection which the above findings have with some simple calculations of the shear stress at the bed. In particular, we can gain some insight into the general effect which unsteadiness in the flow has on incipient motion conditions by now comparing the average velocity u_m with velocities

25

associated with incipient motion in steady flows.   This exercise cannot, of
course, yield any unambiguous conclusions about incipient motion in unsteady flows
since the values of u_m quoted earlier relate to a rippled bed;   this means
that, as far as the results from the present experiment are concerned, the effects
of unsteadiness and a rippled topography are bound to remain inextricably linked.
Taking Shields' relation for incipient motion in steady flow, we have found that
the critical shear stresses for grains of representative diameter D = 0.1 cm
and 0.2 cm are τ_c = 5.5   and 13 dynes/cm^2 respectively.   Adopting the
usual hypothesis for a steady turbulent boundary layer of a logarithmic velocity
profile, these shear stresses can be associated with steady fluid velocities, at
a height of 100 cms above the bed, of 31 cms/sec and 48 cms/sec respectively.
These values are considerably larger than, and in fact about twice, the values
of u_m quoted above.   A comparison of this kind between threshold stresses in
steady and oscillatory flows has been carried out by CHAN, BAIRD and ROUND (1972).

It is perhaps natural to draw the conclusion that the differences between
laboratory and field results at incipient motion are most likely accounted for
largely by the effects of a rippled bed rather than the unsteadiness in the flow.
This is particularly so when we recall that Johns (1975) (see Part I, Section
2.4(v)) has shown that the discrepancy between the turbulent shear stress calcula-
ted on the basis of a steady logarithmic profile assumption (Part I, Section 2.4
Eq (17)) and upon incorporating unsteadiness, is relatively small (between 9%
and 23% depending upon phase in the wave cycle).   In general, for a given value
of $\overline{U_\infty}\big|_{max}$, the shear stress over the crest of a ripple is likely to be
greater throughout the wave cycle than it would be in the case of a flat bed;
and, conversely, a given shear stress over a ripple crest will be brought about
by a smaller value of $\overline{U_\infty}\big|_{max}$ than would be needed over a flat bed.
However the discrepancy between u_m and $\overline{U_\infty}\big|_{max}$ cannot in all probability
be accounted for entirely by the rippled bed (even given that the basis for
comparison between the two quantities is satisfactory), since the unsteadiness
in the flow is likely to have the effects on incipient motion which were
discussed in Part I.   The present exercise confirms the great need, stressed
in Part I, for an analytical solution for the inviscid flow over a rippled bed.

6.2 The state of the boundary layer flow in the sea
In the preceding discussion we have not been specific as to whether the boundary
layer was laminar or turbulent.   As noted in Part I, many criteria for

26

transition   from a laminar to a turbulent boundary layer have been proposed,
these criteria differing for smooth beds, two dimensionally rough (rippled)
beds and three dimensionally rough (flat granular) beds.   Whether or not transition
to turbulence is dominated by the presence of ripples as such, or by the individual
loose grains of which the ripples are composed, is a matter of some doubt at
present;   the former possibility perhaps seems the more likely.   Since a wide
variety of conditions were observed through the present experiment, it is quite
possible that both laminar and turbulent flow states existed for a portion of the
total time.

Our chief concern is the state of the boundary layer when grains are moving.
Thus, taking the critical values at incipient motion adopted above and using
Einstein's criterion for two dimensional roughness (see Part I, Table 2.1),
with the representative roughness k_s as the ripple height of 10 cms, we obtain

$$\frac{U_\infty\, k_s}{\nu} \approx 2 \times 10^4 \gg 640 \quad , \quad \left(U_\infty = u_m \right)$$

According to this the boundary layer is definitely turbulent.   However, if we
take the grain diameter D as the representative roughness k_s , and use
Einstein's criterion for three dimensional roughness, we find that the dimension-
less group takes a value of about 200.   This is about twice the value at the
transition point.   On the other hand, it is an order of magnitude smaller than
the transition point to rough turbulent flow suggested by KAJIURA (1968).

The situation is unclear, therefore, and this is hardly surprising in view of
the large amount of scatter which is apparent in the definitions of transition
in Part 1, Table 2.1.   If the presence of ripples dominates transition, we may
expect the boundary layer to be turbulent when incipient motion occurs, whereas,
if the individual grains dominate the process, we cannot be sure of either laminar
or turbulent flow conditions on the present evidence.   KOMAR and MILLER (1973)
have suggested that if the grain size is greater than about 0.05 cms then the
boundary layer will be turbulent at the threshold of sediment motion.   If this
is correct it would support the view that the observed boundary layer was, indeed,
turbulent.   In future experiments, the injection of dye into the flow near the
bed may help to resolve this problem.

6.3 The processes involved at the threshold of sediment motion
In Part I it was argued that, for the typical situation in the laboratory of a

monochromatic wave train, the parameters of importance in the problem of incipient sediment transport can be identified, and then dimensional arguments can be employed in the development of plausible relationships describing the phenomenon in terms of these parameters. It was also suggested that this masks the details of the processes involved in incipient motion and that the approach quickly breaks down if more than a single wave frequency (and wave length and height) are present simultaneously. This points to the need for information of an instantaneous kind about the important parameters in the problem, close to the bed at the instant of the initiation of grain motion.

In the previous chapter we saw that the values of the horizontal velocity at the threshold of motion (Tables 5.2 and 5.3) were quoted with large standard deviations. The standard errors quoted were much smaller and were presented on the assumption that our observations of $u_h|_\alpha$ and $u_v|_\alpha$ followed a normal error law; this was partially borne out by a comparison of the observations with the Gaussian form. Thus the assumption in presenting the standard errors was that threshold is uniquely determined by a critical value of the velocity and that the observations made were randomly distributed about this value. If this is correct, then the large standard deviations may be the result of the rather subjective method of analysis adopted (see Chapters 4 and 5).

However there are additional factors that need to be considered. In particular, the role of the **pressure gradient** is excluded in the above considerations. This is acceptable in analysing results obtained in the laboratory with a mono-chromatic wave train; typically in such analyses, as we have argued above, the processes involved in incipient sediment motion are not examined directly. However, field studies call for the problem to be tackled rather differently. Thus it is possible to suggest the following conjectural model.

A grain of the bed is set in motion when the force acting on it is sufficient to dislodge it from its resting place. This critical force, F_{crit}, may be separated crudely into (i) a velocity-induced part, F_v, and (ii) a pressure gradient induced part, F_p. Therefore we have

$$F_{crit} = \left[F_v + F_p \right]_{crit}$$

and it is clear that any number of combinations of F_v and F_p may be sufficient to cause sediment motion. For a monochromatic wave train in a

laboratory experiment, a particular value of velocity, and therefore F_v ,
is always associated with the same pressure gradient, and therefore with F_p .
On the other hand, in the sea where two successive waves are seldom identical,
a wide range of values of F_v may be measured at a particular value of
F_p . Consequently, it would not be at all surprising to find a large
standard deviation for a typical velocity threshold value, say, $u_L|_\alpha$. It
follows that if the combined function (F_v + F_p) could be correctly
identified in terms of the flow parameters, threshold might be found to be well
defined with a small standard deviation in terms of this new function. (If
the standard deviation remains large, however, while the scheme of things is
substantially as has been outlined above, then shortcomings in the analysis
method used might still be responsible.)

It appears to be of the utmost importance that we move towards an understanding
of the relative magnitudes of F_v and F_p , something which has not been
possible in this experiment since the pressure difference results were lost.
In this exercise, the approach adopted will depend to a large extent on the degree
of correlation between u_L (or u_v) and Δp ($= \frac{\partial p}{\partial x} \cdot \Delta x$). If, as seems
likely, they are shown to be substantially uncorrelated in the sea, this will
present us with a large set of instantaneous values of basic parameters at
threshold with which to test hypotheses about incipient motion. Such hypotheses
will, of course, have to take into account the phase difference between the
velocity close to the bed and u_L or u_v . Several authors, noting the
limitations imposed by working in the laboratory, have recommended an investigation
along these lines.

It seems reasonable to suggest that the drag force, F_v , is substantially
larger than the pressure gradient induced force, F_p . In fact, CARSTENS,
NEILSEN and ALTINBILEK (1969) have discounted the possibility of the pressure
gradient having a significant role at incipient motion, on the basis of their
experimental observations in the laboratory. However the uncertainty which
surrounds our knowledge of flow conditions adjacent to the exposed grains on the
bed, makes order of magnitude calculations to compare F_v and F_p
unreliable, and we regard this matter as being at present unresolved.

6.4 The Reynolds stress under waves and its relevance to sediment motion
within a wave cycle
One of the principal differences between most of the work done in the laboratory

and the present experiment is that the former work has usually involved measurements of velocity in flows which, in the free stream away from the bed, are x-directed and contain no velocity component in the z-direction. In the sea, (or in laboratory studies involving a free surface) this is no longer the case and, as has been described in Chapter 4, the present experiment has been concerned with the measurement of two components of the velocity (u and w) at various heights above the bed.   The turbulent fluid shear stress has been obtainable, therefore, by means other than those used by JONSSON (1963)(see Part I, Section 2.4(v)) and others, notably by calculating the Reynolds stress directly. (Appendix I contains a general discussion about the measurement of the Reynolds stress in a fluid flow with an EM flowmeter).

The turbulent fluid shear stress is $\tau_t = -\rho_f \, \overline{uw}$, where the overbar denotes time averaging taken over the required interval.   This interval is normally much longer than the wave period, and therefore the stress computed is the residual stress arising from the wave action.   It is observed in Part I that it is the instantaneous stress, rather than the residual stress, which is one of the factors of importance in considering incipient sediment motion and the instant- aneous sediment transport rate.   Thus, in practice, in the calculation of the turbulent fluid stress, we require the time averaging to be taken over an interval which is short ,compared with the wave period.   In other words, we must be careful to make a clear distinction between the Reynolds stress over many wave cycles and the Reynolds stress within a wave cycle.   A problem can arise in the calculation of the latter as we will argue below.

Figures 5.15 and 5.16 show how the instantaneous values of the products $u_\perp w_\perp$ and $u_v w_v$ fluctuate about their means.   Now, provided that measurements of the fluctuating components of velocity are made sufficiently close to the bottom, we might initially be tempted to suppose that it is possible to relate instantaneous values of the product, uw , to the instants at which sediment motion starts or stops.   However care must be exercised here because the fluid stress in the flow, which is connected with the existence of a fluid stress at the bed and possibly, therefore, with sediment transport, cannot be calculated directly from the entire momentum flux at an instant, implicit in the product signal uw.   We can illustrate the reason for this by considering the results of the Fourier decomposition of the signals   u and w , at a single frequency ω_0 ; this frequency may be any one of those emerging from the spectral

30

analysis of the full data sets.

Suppose we have a flow field dominated by progressive wave motion:

$$u(\omega_0) = a\cos\omega_0 t + b\sin\omega_0 t$$
$$w(\omega_0) = c\cos\omega_0 t + d\sin\omega_0 t$$

then the full product signal uw at this frequency is

$$uw(\omega_0) = ac\cos^2\omega_0 t + (ad+bc)\cos\omega_0 t\sin\omega_0 t + bd\sin^2\omega_0 t$$

It is this* which we have plotted in Figs 5.15 and 5.16. Now, still at the
single frequency ω_0, the product signal can be subdivided into two component
parts; firstly a part made up of the in-phase components giving expression
to that part of the flow field in which energy dissipation is taking place, and
secondly out-of-phase components corresponding to the frictionless or potential
part of the flow field. Thus

$$uw(\omega_0)\big|_{\text{dissipative}} = ac\cos^2\omega_0 t + bd\sin^2\omega_0 t$$
$$uw(\omega_0)\big|_{\text{frictionless}} = (ad+bc)\sin\omega_0 t\cos\omega_0 t$$

Taking time averages over an interval long compared with the period ($2\pi/\omega_0$)
gives

$$\overline{uw(\omega_0)}\big|_{\text{dissipative}} = \tfrac{1}{2}(ac+bd)$$

$$\overline{uw(\omega_0)}\big|_{\text{frictionless}} = 0$$

This is the situation which usually exists when values of the Reynolds stress
are quoted. However, averaged over intervals short compared with ($2\pi/\omega_0$)
both the dissipative and frictionless parts of the product signal yield non-zero
contributions in general. Since it is only the dissipative part of the flow
field which can possibly be relevant to instantaneous sediment transport
(and, in particular, to F_v in the previous Section), it is necessary to remove
the non-zero frictionless part of the product signal from the total signal,
that is

* P.31, para 1, line 6
  Change to 'It is $\sum_{\omega_0} uw(\omega_0)$ which we have plotted ......'

31

$$uw(\omega_o)\Big|_{\text{dissipative}} = uw(\omega_o) - uw(\omega_o)\Big|_{\text{frictionless}}$$

at an instant.   A correlation between this quantity and any sediment transport
observed must then be sought.   Such a correlation is by no means certain to be
found, since the height at which the velocity observations are made will usually
be an appreciable distance above the bed on which the grains are moving.
Nevertheless it is extremely likely that the ▮▮▮▮▮▮ shear stress in the flow
plays an important part in the sediment transport process as a whole.

In Chapter 5 we described an analysis of results at the threshold of motion, in
which an unsuccessful attempt was made to relate incipient sediment motion to the
fluid shear stress.   Since we worked with $\sum_{\omega_o} uw(\omega_o)$ rather than
$\sum_{\omega_o} uw(\omega_o)\Big|_{\text{dissipative}}$, it is perhaps not surprising that this
analysis provided no useful information.   Unfortunately in examining the data
from the present experiment we were not in a position even to accurately calculate
the Reynolds stress (residual stress) over many wave cycles, for reasons which
have been discussed elsewhere.   An examination of instantaneous stresses was not
possible both on account of the lack of complete synchronisation between the video
record and the digitised data, and on account of the lack of information about
the zero points on both of the velocity channels.   However, with the data
obtained in experiments in the future, we hope to pursue an analysis along the
lines proposed above.

6.5 Concluding remarks and comments about the future aims of the project
In the two preceding Sections we have suggested, in their general outlines,
two methods of data analysis which we consider important to develop in the future.
In this Section, we look briefly at the present state of knowledge in the field
of study as a whole, with particular reference to the questions which were raised
in Part I, Sections 1.1 and 1.2.   We take initially the fluid flow aspects of
the study.

Several times in this report, we have pointed to the need for the development of
a potential flow solution for small amplitude waves over a rippled bed.   At
present, analytical solutions exist both for the case of a smooth horizontal bed
and for a smooth bed of constant slope.   In the case of the former, there seems
to be reasonable agreement between the classical theoretical solution and
measurements of the free stream flow.   However no analytical solution exists for

the case of a rippled bed, which is the case commonly encountered in the sea. Departures from the appropriate inviscid flow solution may be expected to indicate the extent and nature of the wave boundary layer, and, as long as the inviscid solution for a rippled bed remains unknown, the character of the boundary layer in this case will remain largely unknown also.

The theoretical solution for viscous laminar flow above a smooth horizontal bed is well known, and has been shown in the laboratory to predict correctly both the amplitude and the phase angle of the oscillatory motion as functions of distance from the bed. The replacement of a smooth bed by a rough sand bed causes departures from the solution which are not yet clearly understood; it seems that a relaxation of the "no slip" condition at the bed is required to account for these departures. Of rather more importance than this, however, is the fact that in many situations the dissipative flow in the boundary layer may not be laminar but turbulent. This is an aspect of the study of the wave boundary layer where there is considerable uncertainty at present, largely on account of the lack of agreement which exists as to the conditions needed for transition from laminar to turbulent flow. Furthermore, there is even doubt as to what constitutes 'turbulence' in the present context. In view of this, we feel that future experimental investigations must include flow visualization, by the injection of dye into the flow at different heights above the bed, in order to determine the critical conditions for transition to turbulence in the sea. Transition itself is governed by the fluid flow parameters and the nature of the bed roughness. The latter may be characterized either by the sand grains or by any ripples on the bed, but which of these two dominates transition where they are found together, is at present uncertain. We have suggested that it is more likely that transition is dominated by the ripples.

When the boundary layer has become fully turbulent, it is to be expected that its principal features can be represented either in a semi-theoretical or an empirical way. Unfortunately, we do not feel justified in adopting with confidence any of the existing representations which have been proposed, for the purpose of drawing detailed conclusions about instantaneous velocity profiles in the boundary layer or about instantaneous values of the bed shear stress. The central problem here is the prevailing uncertainty about the correct functional form for the eddy viscosity. Many authors have adopted effective viscosity representations which are functions of height above the bed only, whereas it has become clear that what is required is an eddy viscosity which

is a function both of height and phase angle in the wave cycle.   Attempts have
been made to elucidate the gross features of the function from experiments in the
laboratory.   However, all that seems clear is that the effective viscosity must
have the following behaviour:

effective viscosity
of the flow
=
$\Big($ μ , the molecular viscosity, in the
thin layer immediately adjacent to the bed

$\Big($ $\varepsilon_m (\gg \mu)$, where $\varepsilon_m(z,t)$ is the eddy
viscosity in the turbulent boundary layer

$\Big($ $\longrightarrow$ 0 upon entering the potential flow
region (i.e. the free stream flow)

It is to be hoped that the form of the effective viscosity can be determined from
measurements made in the sea, enabling us to model the flow in the boundary layer.
This aim is closely connected with the matter of transition to turbulence since,
as we argued in Part 1, Section 2.3, a significant departure from unity of the
non-dimensional quantity $K_v = \{(\varepsilon_m + \mu)/\mu\}$ may serve as a suitable
criterion for transition.

Turning now to the sediment motion aspects of the study, we have found that there
have been a considerable number of studies of the threshold of sediment motion in
oscillatory flow, but comparatively few treating the problem of the quantity of
sediment in motion during the wave cycle.   The conditions needed for incipient
motion are usually defined in terms of a "critical wave" belonging to a wave
train having a single frequency.   Such a wave train can be generated in a wave
flume in the laboratory but is seldom, if ever, found in isolation in the sea.
Consequently we have argued (see Part 1, Section 3.3(i) and Section 6.1) that the
approach to an understanding of incipient motion based on a "critical wave" is
not directly helpful to our investigation of critical conditions in the sea.
Nevertheless it may be possible to define approximately a "critical wave" in
the sea (or at least a class of critical waves) for purposes of comparison with
work done in the laboratory.   For instance, we could in future experiments
measure the velocity amplitude $U_{\infty max}$ of each half-cycle noting which waves cause
sediment motion, and by doing this it might become apparent that below some
reasonably well defined value $\overline{U}_{\infty max}\big|_{crit}$ no sediment motion occurs.   This value
might well differ from our existing values of u_m (see Section 6.1) enabling
us to improve our basis of comparison.   On the other hand, if the pressure
gradient plays a crucial part in incipient sediment motion, we might find that
this exercise produces no useful information.   In this connection we have

34

emphasised the need for measurements of the pressure gradient in a wave flow and hope in the future to be able to make such measurements over much shorter distances in the direction of wave travel than the 10m in the present experiment.

In our programme of observations in the field we are restricted, at present, to visual observations of sediment motion, and, therefore, to the highly subjective methods of data analysis described in Chapter 5. As far as quantifying the amount of sediment motion is concerned, we are at present unable to estimate this even approximately, and therefore it has not yet been possible to draw any detailed conclusions about the relative merits of the various existing sediment transport rate formulae. It is to be hoped that, in the reasonably near future, new instruments will be developed enabling sediment transport rates to be quantified reliably.

It is important for the programme of measurements in the sea to be continued and extended, ultimately to the measurement of small second order quantities such as the residual mass transport velocity and the longshore current. For, having developed an understanding of the first order motion in the wave boundary layer, which mobilises the sediment, it will become important to study these small second-order residual effects. They are likely, for instance, to determine whether accretion or erosion of material occurs on the foreshore. More generally, the problem of the superimposition of a wave flow and a tidal current is a long term objective; in this case the non-linear interaction of the two first order flows will have to be taken into account. Finally, it is to be hoped that the experimental study will be accompanied by theoretical or semi-theoretical investigations of the processes involved in both the fluid flow and the sediment transport aspects of the problem.

We conclude that the most pressing questions requiring research are:

(i) What is the inviscid oscillatory flow pattern over a rippled bed under small amplitude waves?
(ii) Under what conditions are oscillatory flows laminar or turbulent near the seabed?
(iii) If the flow is turbulent what is the form of the effective viscosity?

(iv) Knowing the effective viscosity for both flat and rippled sand beds, what is the nature of the velocity profile close to the bed and what is the resulting bed shear stress? Further, what is the relationship of the turbulent shear stress measured in the flow above the bed to the stress at the bed **itself**?

(v) What critical fluid velocities and pressure gradients close to the seabed cause the sediment to become mobile in an oscillatory flow? (We await the development of new instrumentation before the transport rate of the mobile material can be quantified.)

REFERENCES

BAGNOLD, R.A. (1946) Motion of waves in shallow water. Interaction with a sand
       bottom. Proceedings of the Royal Society, London. Series A, 187, 1-185.

BENDAT, J.S. and PIERSOL, A.G. (1971) Random data: analysis and measurement
       procedure. J.Wiley and Sons Inc. 407pp.

CARSTENS, M.R., NEILSON, F.M. and ALTINBILEK, H.D. (1969). Bedforms generated
       in the laboratory under an oscillatory flow: analytical and experimental
       study. U.S. Army Corps of Engineers, Coastal Engineering Research
       Center Technical Memorandum Number 28, 93 pp. (Unpublished manuscript)

CHAN, K.W., BAIRD, M.H.I. and ROUND, G.F. (1972). Behaviour of beds of dense
       particles in a horizontally oscillating liquid. Proceedings of the
       Royal Society, London. Series A, 330 537-559.

DAVIES, A.G. and WILKINSON, R.H. (1977). The movement of non-cohesive sediment
       by surface water waves, Part I: Literature survey. Institute of
       Oceanographic Sciences Report Number 45   (Unpublished
       manuscript).

DAYTON, C.M. and STUNKARD, C.L. (1971). Statistics for problem solving. McGraw-Hill
       Inc. 290 pp.

EINSTEIN, H.A. (1972). A basic description of sediment transport on beaches.
       Chapter 2 of 'Waves on beaches and resulting sediment transport'
       edited by Meyer R.E.Publication Number 28 of the Mathematics Research
       Center, The University of Wisconsin. Academic Press.

JOHNS, B. (1975). The form of the velocity profile in a turbulent shear wave
       boundary layer. Journal of Geophysical Research 88 (36) 109-5112.

JONSSON, I.G. (1963). Measurements in the turbulent wave boundary layer.
       Proceedings 10th Congress of the International Association for Hydraulic
       Research (1). 85-92. London.

KAJIURA, K. (1968). A model of the bottom boundary layer in water waves.
       Bulletin of the Earthquake Research Institute 46. 75 - 123.

KOMAR, P.D. and MILLER, M.C. (1973). The threshold of sediment movement under
       oscillatory water waves. Journal of Sedimentary Petrology, 43(4)
       1101-1110.

LONGUET-HIGGINS, M.S. (1958). The mechanics of the boundary layer near the bottom
       in a progressive wave. Appendix to 'An experimental investigation
       of drift profiles in a closed channel. By Russell, R.C.H. and Osorio,
       J.D.C. Proceedings 6th Coastal Engineering Conference. 184 - 193.

MANOHAR, M. (1955). Mechanics of bottom sediment movement due to wave action.
       U.S. Army Corps of Engineers. Beach Erosion Board Technical Memorandum

Number 75, 121 pp. (Unpublished Manuscript)

PROUDMAN, J. (1952)   Dynamical Oceanography, Methuen.

RANCE, P.J. and WARREN, N.F. (1968).   The threshold of movement of coarse
material in oscillatory flow. Proceedings 11th Coastal Engineering
Conference, London. 487 - 491.

RAYMENT, R. (1970).   Introduction to the Fast Fourier Transform (FFT) in the
production of spectra. Meteorological Magazine, 99. 261-269.

SEITZ, R.C. (1971). Measurement of a three-dimensional field of water velocities
at a depth of one metre in an estuary. Journal of Marine Research, 29,
(2), 140-150.

SILVESTER, R. and MOGRIDGE, G.R. (1970). Reach of waves to the bed of the
Continental Shelf. Proceedings 12th Coastal Engineering Conference.
651 - 667.

SLEATH, J.F.A. (1974). Stability of laminar flow at the sea bed.   Proceedings
of the American Society of Civil Engineers, Journal of Waterways,
Harbours and Coastal Engineering Division, 100.   105-122.

APPENDIX I

The measurement of the fluid stress on a plane using a EM flowmeter

A.1 Introduction

The problem of the calculation of the Reynolds stress from velocity components
measured with an electromagnetic flowmeter was mentioned in Chapters 5 and 6.
Large errors in the stress can arise from a misalignment of the EM 'head' due to
rotation in the measuring plane, and in an example discussed later, a misalignment
of 5° in a unidirectional flow is shown to give rise to errors in the stress of
about 40%. The corresponding errors for the residual stress under waves can be
considerably larger.

There is a difficulty in defining a suitable set of axes on a vertical measuring
plane in the sea. The 'horizontal' axis may be taken as the true horizontal,
or be chosen parallel to the sea bed. However, it is more useful in the context
of the measurement of turbulent stresses to adopt a third choice, that is to
define the direction in which the mean fluid velocity is zero as the 'vertical'
(or z) direction.

Here we consider the general problems arising in the calculation of the fluid
stress tensor from the measured components of fluid velocity. The tensor
examined is composed only of terms describing the convection of fluid momentum.
The hydrostatic pressure and the small terms arising from molecular viscosity are
neglected. In particular, simple rules are developed for the transformation
of the measured stress tensor into the desired one by an effective rotation of
the axes of measurement. In addition, an analogy between the stress configurations
on a plane in a solid body and in a fluid, enables ideas which have been
developed for the former case to be adapted to the latter. Finally, the
implications of a rotation of the axes of measurement on spectra and cross-spectra
are discussed.

A.2 Background

At any point in a two-dimensional steady shearing flow, a plane can be defined
across which there is a transfer of fluid momentum but no transfer of fluid mass.
For example, in the case of a uniform laminar flow in the x-direction in the
xz-plane, the transfer of streamwise momentum produces a shear stress $\tau_z = \mu \dfrac{dU}{dz}$

on the x y-plane, where μ is the molecular viscosity.   In a turbulent flow,
the plane can only be defined in a time averaged sense, on the basis of the mean
streamline pattern.   Thus, at the general point 0 in Fig A1, we seek the direction
in which the mean velocity is zero, and this we define as the 'z'-direction.   The
measured velocity field
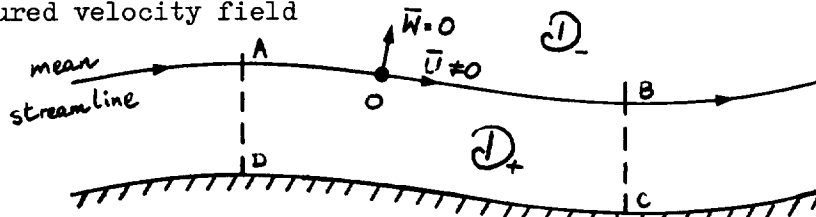
Fig A.1

(U_* (t), W_* (t)) at 0 in the xz-plane will typically be such that
$\overline{U}_* \neq 0$, $\overline{W}_* \neq 0$ over an arbitrary averaging period.   However, it is
simple to 'rotate' the EM head digitally to establish the angle between the
'desired' axes and those in which the measurements were made.   Following the
rotation of the axes, the calculation of the desired stress at 0 can proceed by
calculating the co-variance between the reduced sets of velocity data.   Essentially,
therefore, the problem is that of establishing the direction of the mean stream-
line at the point 0 during some given time interval.   There will be no net fluid
transfer across either the upper streamline AB or the bottom boundary DC of the
region $\mathcal{D}_+$, whilst a shear stress will act on both.   Thus the effect of the
flow in the region $\mathcal{D}_-$ on that in $\mathcal{D}_+$ can be represented by a velocity and a
shear stress along the streamline AB.

In the equations of motion, the turbulent stresses in the flow are replaced by
the array of Reynolds stresses which complement the (small) viscous terms $\nu \nabla^2 \underline{V}$
where $\underline{V} = (U, V, W)$.   These turbulent stresses are averaged over a period
that is long compared with the duration of the turbulent fluctuations.   In
writing τ_{ij} to represent a general component of stress, the first suffix i
denotes the direction of the stress and the second suffix j denotes the
direction of the normal to the plane on which the stress acts.   The complete
stress tensor in a rectangular set of axes 0123 is:

$$\tau = \begin{pmatrix} \tau_{11} & \tau_{12} & \tau_{13} \\ \tau_{21} & \tau_{22} & \tau_{23} \\ \tau_{31} & \tau_{32} & \tau_{33} \end{pmatrix}$$

(A.1)

Suppose initially that we have an instrument which measures the full stress
tensor in a second set of rectangular axes 01'2'3':-

$$\tau_M' = \begin{pmatrix} \tau_{11}' & \tau_{12}' & \tau_{13}' \\ \tau_{21}' & \tau_{22}' & \tau_{23}' \\ \tau_{31}' & \tau_{32}' & \tau_{33}' \end{pmatrix} \qquad (A.2)$$

From the rules of tensor transformation we have:-

$$\tau_{j\ell}' = \ell_{ij} \, \ell_{k\ell} \, \tau_{ik} \qquad (A.3)$$

where ℓ_{ij} are the direction cosines. Equation (A.3) contains nine equations for the components $\tau_{j\ell}'$ but, since the frames of reference 0123 and 01'2'3' are both rectangular sets of axes, it is only possible to specify three of the nine ℓ_{ij}. The six remaining values are determined from:-

$$\ell_{ij} \, \ell_{kj} = \delta_{ik} \qquad (A.4)$$

where δ_{ik} is the Kronecker delta.

Using an EM flowmeter it is only possible to measure the stress tensor, comprising normal and shear stresses, on any one plane. The measured stress tensor in two dimensions can be written

$$\tau_M = \begin{pmatrix} \tau_{11}' & \tau_{13}' \\ \tau_{31}' & \tau_{33}' \end{pmatrix} \qquad (A.5)$$

This is again in the frame of reference 01'2'3', the measurement of velocity being made in the 1'3' plane with the stern of the flowmeter lying along 2'0. Clearly, this information is insufficient to draw any conclusions about the complete stress tensor τ, and we are in a position therefore to ask specific questions only about the stress in the plane 1'3'. We will examine initially a special case involving the reduced stress tensor τ_M.

Suppose the two reference frames 0123 and 01'2'3' have a common axis, such that 02 and 02' are coincident. It follows that the 'measuring' and 'desired' planes are coincident, with the EM head giving the velocities in this plane in the 01' and 03' directions. To obtain the fluid stress in relation to the 'desired' axes, we perform a 'rotation' of the head through an angle θ, as indicated in Fig A.2. The direction cosines are then given by
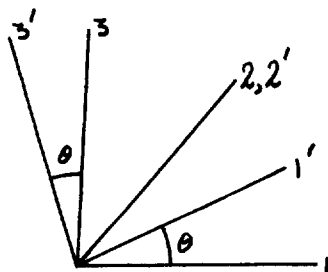
$$\ell_{ij} = \begin{pmatrix} \cos\theta & 0 & -\sin\theta \\ 0 & 1 & 0 \\ \sin\theta & 0 & \cos\theta \end{pmatrix} \qquad (A.6)$$

Fig A.2

Using Equation (A.3) and the fact that the stress tensor is symmetrical it can be shown that, in this case, the elements of the measured stress tensor τ_M' bear the following relationship to the elements of the 'desired' stress tensor τ.

41

$$\tau_{11}' = \tfrac{1}{2}\left(\tau_{11} + \tau_{33}\right) + \tfrac{1}{2}\left(\tau_{11} - \tau_{33}\right)\cos 2\theta + \tau_{13}\sin 2\theta \tag{A.7}$$

$$\tau_{22}' = \tau_{22} \tag{A.8}$$

$$\tau_{33}' = \tfrac{1}{2}\left(\tau_{11} + \tau_{33}\right) + \tfrac{1}{2}\left(\tau_{33} - \tau_{11}\right)\cos 2\theta - \tau_{13}\sin 2\theta \tag{A.9}$$

$$\tau_{12}' = \tau_{21}' = \tau_{12}\cos\theta + \tau_{32}\sin\theta \tag{A.10}$$

$$\tau_{13}' = \tau_{31}' = -\tfrac{1}{2}\left(\tau_{11} - \tau_{33}\right)\sin 2\theta + \tau_{13}\cos 2\theta \tag{A.11}$$

$$\tau_{23}' = \tau_{32}' = -\tau_{12}\sin\theta + \tau_{23}\cos\theta \tag{A.12}$$

Equations (A.7) to (A.12) are equations for the nine 'measured' components of stress in terms of the required components. It is, of course, only τ_{11}', τ_{33}' and τ_{13}' $\left(= \tau_{31}'\right)$ which are measured. The components τ_{ii}' are normal fluid stresses.

A.3 An analogy with the theory of the stress system in a solid body.
In order to illustrate the significance of the Eqs (A.7), (A.9) and (A.11), we can examine the analogy with the Mohr's Stress Circle theory from solid mechanics, since the stress configuration on a plane in a solid cuboid is directly comparable with the fluid stresses in a turbulent flow acting on a plane in an Eulerian frame of reference. In the two-dimensional case in Fig A.3, we take initially an arbitrary plane through PP' (normal to the plane of the paper) on which the resultant stress pattern is to be studied. Resolution of this
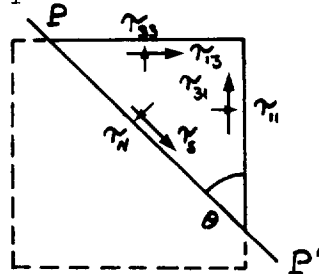
Fig A.3

stress on the plane into a normal component τ_N and a shear component τ_s, and use of the relation $\tau_{13} = \tau_{31}$, leads to the equations:

$$\tau_N = \tfrac{1}{2}\left(\tau_{11} + \tau_{33}\right) + \tfrac{1}{2}\left(\tau_{11} - \tau_{33}\right)\cos 2\theta + \tau_{13}\sin 2\theta \tag{A.13}$$

$$\tau_s = -\tfrac{1}{2}\left(\tau_{11} - \tau_{33}\right)\sin 2\theta + \tau_{13}\cos 2\theta \tag{A.14}$$

which are directly comparable with Eqs (A.7) and (A.11). We note, at this

stage, that in the absence of shear in the flow $\tau_{11} = \tau_{33}$ and $\tau_{13} = 0$ in which case, from Eqs (A.13) and (A.14), $\tau_N = \tau_{11} = \tau_{33}$ and $\tau_s = 0$.

The planes on which τ_N has a turning value, when $\theta = \theta_p$ say, can be established by differentiating (A.13) with respect to θ :

$$\frac{d\tau_N}{d\theta} = 0 \quad when \quad \tan 2\theta_p = \frac{2\,\tau_{13}}{(\tau_{11} - \tau_{33})} \qquad (A.15)$$

This **provides** two values of θ_p, $\pi/2$ apart, and on these planes $\tau_s = 0$.
In the solid body case, the maximum value of τ_N is termed the 'major principal stress', τ_1, and the minimum value of τ_N is termed the 'minor principal stress' τ_3, $(\tau_1 > \tau_3)$. The planes on which the principal stresses act are termed the 'principal planes' θ_p. Adopting this terminology in the present problem, we can use the definition of τ_1 to produce the relation

$$\tan \theta_p = \frac{\tau_1 - \tau_{11}}{\tau_{13}}$$

and, further, it can be shown that

$$\tau_{1,3} = \tau_{N \, max, min} = \tfrac{1}{2}\left(\tau_{11} + \tau_{33}\right) \pm \tfrac{1}{2}\sqrt{\left(\tau_{11} - \tau_{33}\right)^2 + 4\,\tau_{13}^2}$$

In a similar way, planes can be established on which τ_s has a turning value: by setting $d\tau_s/d\theta = 0$ we obtain two planes θ_s, again $\pi/2$ apart, defined by

$$\tan 2\theta_s = \left(\tau_{33} - \tau_{11}\right)/2\,\tau_{13}$$

from which it follows that

$$\tau_{s \, max, min} = \pm \tfrac{1}{2}\sqrt{\left(\tau_{11} - \tau_{33}\right)^2 + 4\,\tau_{13}^2}$$

or

$$\tau_{s \, max, min} = \pm \tfrac{1}{2}\left(\tau_1 - \tau_3\right)$$

The relation between θ_s and θ_p can be shown to be

$$\theta_s = \theta_p + \pi/4$$

and, on a plane defined by θ_s, the normal stress is given by

$$\tau_N\Big|_{\theta_s} = \tfrac{1}{2}\left(\tau_{11} + \tau_{33}\right)$$

Further, the sum of normal stresses on perpendicular planes can be shown to be

$$\tau_N\Big|_{\theta} + \tau_N\Big|_{\theta + \pi/2} = \tau_1 + \tau_3$$

We can display the relation between τ_N and τ_s in the Mohr's Stress Circle. If we introduce an angle ϕ such that $\phi = 0$ corresponds to $\tau_N = \tau_1$, and $\phi = \pi/2$ corresponds to $\tau_N = \tau_3$, it follows that

$$\tau_N = \tfrac{1}{2}(\tau_1 + \tau_3) + \tfrac{1}{2}(\tau_1 - \tau_3)\cos 2\phi$$
$$\tau_s = -\tfrac{1}{2}(\tau_1 - \tau_3)\sin 2\phi$$

Thus, firstly, we have expressed the information about the complete stress system in terms of the principal stresses $\tau_{1,3}$ and, secondly, have performed a further resolution to obtain equations for τ_N and τ_s on a general plane defined by ϕ. These equations can be written in the form

$$x = A + B\cos\omega, \quad y = -B\sin\omega \implies (x-A)^2 + y^2 = B^2$$

which is the equation of a circle in the frame of reference (x, y). With $x = \tau_N$, $y = \tau_s$ and $\omega = 2\phi$, we have available, therefore, a simple graphical representation of the stress system, see Fig A.4. The co-ordinates of

Fig A.4
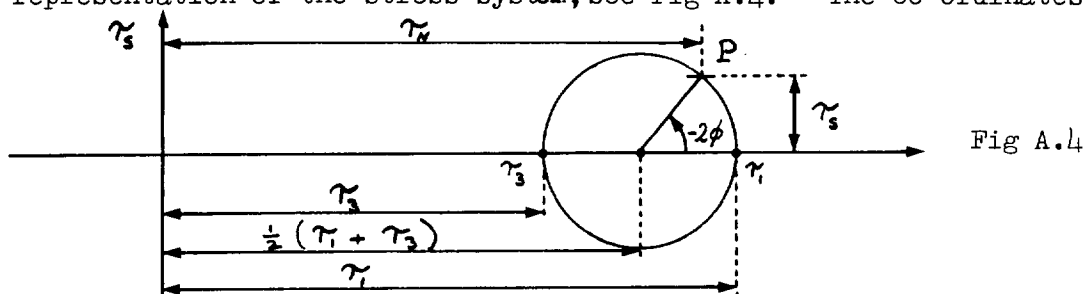
the general point P in the figure are τ_N and τ_s, on a plane making an angle $-\phi$ with a principal plane. Each point on the circumference of the circle represents a stress state on a particular plane through the given point in the body.

Measurement of two velocity components with an EM flowmeter enables the calculation of the stress tensor to be made relative to axes defined by the positioning of the electrodes in the measuring plane. In general, this calculated stress may be at any point P on the circle. It was argued earlier that the fluid stress has a rather more obvious physical meaning if it is evaluated with respect to axes defined according to the criterion $\overline{W} = 0$. Any rotation of axes required to meet this criterion amounts to a rotation of two degrees in the stress circle for every one degree that the head is 'rotated'. Thus it is clear that, depending upon the starting position P on the stress circle, departures from the measured normal and shear stresses may differ greatly for the same head rotation. In general, the smaller is the shear stress the greater will be the absolute (not mention proportional) changes arising in the shear stress due to a digital head rotation.

44

A.4 The rules for the rotation of the EM flowmeter head

Consider now the composition of the stress tensor in terms of the velocity components in a three-dimensional flow field. We will take the stress tensor to consist of stresses arising from the convection of momentum due to both mean and turbulent components (see PROUDMAN (1952, pp 93-94)). Writing $U = \bar{U} + u$, etc, the mean values of the time rate of convection of momentum across unit area over a fundamental time interval give rise to a tensor of the form

$$\begin{bmatrix} \rho\,\bar{U}^2 + \rho\,\overline{u^2} & \rho\,\bar{U}\bar{V} + \rho\,\overline{uv} & \rho\,\bar{U}\bar{W} + \rho\,\overline{uw} \\ \rho\,\bar{U}\bar{V} + \rho\,\overline{uv} & \rho\,\bar{V}^2 + \rho\,\overline{v^2} & \rho\,\bar{V}\bar{W} + \rho\,\overline{vw} \\ \rho\,\bar{U}\bar{W} + \rho\,\overline{uw} & \rho\,\bar{V}\bar{W} + \rho\,\overline{vw} & \rho\,\bar{W}^2 + \rho\,\overline{w^2} \end{bmatrix} \quad (A.16)$$

In order to link the tensor (A.16) to the earlier results, consider only the 13-plane for simplicity. If the measured velocities are (U_*, W_*) and the desired velocities are (U, W), (see Fig A.5), then

$$U = U_* \cos\theta - W_* \sin\theta$$
$$W = W_* \cos\theta + U_* \sin\theta \quad (A.17)$$
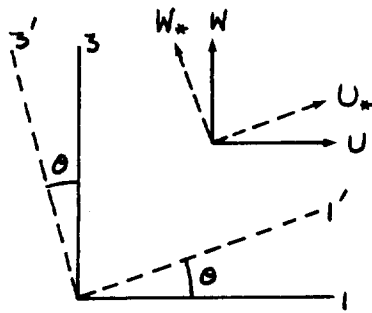
or, alternatively

$$U_* = U \cos\theta + W \sin\theta$$
$$W_* = W \cos\theta - U \sin\theta \quad (A.17a)$$

Fig A.5

As far as the rotation of the EM head is concerned, to convert the measured quantities U_* and W_* to the required U and W with $\bar{W} = 0$, we note that

$$\bar{W} = 0 \quad \text{when} \quad \tan\theta = -\frac{\bar{W}_*}{\bar{U}_*}$$

Here θ represents the angle through which the EM head must be 'rotated' (in the sense of Fig A.5), and its value has a meaning as an average appropriate to some time interval.

The measured product of U_* and W_* can be written

$$U_* W_* = UW \cos 2\theta + \tfrac{1}{2}\left(W^2 - U^2\right) \sin 2\theta \quad (A.18)$$

Using Reynolds' technique and substituting $U = \bar{U} + u$, $W = \bar{W} + w$, Eq (A.18)

45

becomes, after time averaging and mulitplication by ρ :

$$\rho \,\overline{U_* W_*} = \left(\rho \,\overline{U}\,\overline{W} + \rho \,\overline{uw} \right) \cos 2\theta + \tfrac{1}{2}\left(\rho \,\overline{W}^2 + \rho \,\overline{w^2} - \rho \,\overline{U}^2 - \rho \,\overline{u^2} \right) \cdot \sin 2\theta \tag{A.19}$$

Here the left hand side is equal to τ_{13}' in (A.5) and, noting the equivalence of (A.16) and (A.2), (A.19) can be written

$$\tau_{13}' = \tau_{13} \cos 2\theta - \tfrac{1}{2}\left(\tau_{11} - \tau_{33} \right) \sin 2\theta \tag{A.20}$$

in agreement with Eq (A.11). Similarly, by expanding the relations $\tau_{11}' = \rho \,\overline{U_*^2}$ and $\tau_{33}' = \rho \,\overline{W_*^2}$ using (17a), Eqs (A.7) and (A.9) are easily recovered.

The desired shear stress can be written in terms of the measured velocity components as follows:

$$\tau_{13} = \rho \,\overline{UW} = \rho \left\{ \overline{U_* W_*} \cos 2\theta + \tfrac{1}{2}\left(\overline{U_*^2} - \overline{W_*^2} \right) \sin 2\theta \right\} \tag{A.21}$$

Excluding mean flow contributions and dividing this by ρ , we obtain

$$\overline{uw} = \overline{u_* w_*} \cos 2\theta + \tfrac{1}{2}\left(\overline{u_*^2} - \overline{w_*^2} \right) \sin 2\theta \tag{A.22}$$

A.5 Numerical Illustrations

(i) Unidirectional flow: Substituting in (A.22) some typical readings for a tidal stream   (obtained by our colleague R.L. Soulsby):

$$\overline{u_*^2} = 36 \text{ cm}^2/\text{sec}^2, \qquad \overline{w_*^2} = 10 \text{ cm}^2/\text{sec}^2, \qquad \overline{u_* w_*} = -6 \text{ cms}^2/\text{sec}^2$$

we have

$$\overline{uw} = -6 \cos 2\theta + 13 \sin 2\theta$$

In this case, a rotation of the EM head through an angle θ , in the sense of Fig A.5, produces the following results:

θ :	$-5°$	$-3°$	$-1°$	$0°$	$1°$	$3°$	$5°$
$\overline{uw}$:	-8.15	-7.35	-6.45	-6.0	-5.56	-4.65	-3.65

Thus a misalignment of the measuring head from its desired orientation in the 13-plane gives rise to changes in the Reynolds stress of 36% and 39% for head

46

rotations of -5° and $+5^{\circ}$ respectively. The importance of obtaining the correct head orientation in the measurement of Reynolds stress needs no further emphasis, and, if mean flow contributions are included as required for the study of the total stress (see (A.19)), the need for correct head orientation becomes even more acute.

(ii) Oscillatory flow: The same problem arises in the measurement of the residual shear stress under waves, where the averaging period is taken over many wave cycles.   This stress is normally a small term associated with second-order residual mass transport velocities.   Consequently, it is not surprising that its measurement poses a difficult problem.

Examples of velocities relevant to this problem (from Table 5.4 of the main body of this report) are

$$\overline{u_*^2} = 152.5 \text{ cms}^2/\text{sec}^2 \qquad \overline{w_*^2} = 1.4 \text{ cms}^2/\text{sec}^2 \text{ at } \approx 30\text{cms above the bed}$$
$$\overline{u_*^2} = 134.5 \text{ cms}^2/\text{sec}^2 \qquad \overline{w_*^2} = 1.3 \text{ cms}^3/\text{sec}^2 \text{ at } \approx 1\text{m above the bed}$$

It follows from Eq (A.22) that large variations arise in the shear stress as Θ is varied:

Θ		-5°	-3°	-1°	0°	1°	3°	5°
$\overline{uw}$ at	$\approx$ 30cms	-23.4	-18.3	-13.1	-10.4	-7.8	-2.5	2.9
$\overline{uw}$ at	$\approx$ 1m	-12.9	-8.3	-3.7	-1.3	1.0	5.7	10.3

These values of shear stress are not strictly comparable with the values of Reynolds stress quoted for unidirectional flow, even though the data sets have been reduced in both cases, by the subtraction of their mean values prior to the calculation of the stress.   The reason for this is that in an oscillatory flow, both $\overline{U_*}$ and $\overline{W_*}$ are likely to be very small, which means that the values quoted are approximately equal to total stress values; whereas in the case of a unidirectional tidal flow, $\overline{U_*}$ will be large and the Reynolds stress will have a very different value to the total stress.

We can now calculate the angle through which the EM head must be rotated in order to measure a maximum or minimum in the shear stress.   Since the desired shear stress has a turning value when $\frac{d}{d\Theta}\left(\rho\, \overline{uw}\right) = 0$, that is when

47

$$\tan 2\theta = \{ \overline{u_*^2} - \overline{w_*^2} \} / 2\, \overline{u_* w_*} \quad,$$

it can be shown for the unidirectional flow case that:

when $\quad \theta = 57\frac{1}{2}^{\circ}$ (and $-122\frac{1}{2}^{\circ}$), $\qquad \rho\, \overline{uw} \qquad$ has a maximum,

and when $\quad \theta = 147\frac{1}{2}^{\circ}$ (and $-32\frac{1}{2}^{\circ}$), $\qquad \rho\, \overline{uw} \qquad$ has a minimum.
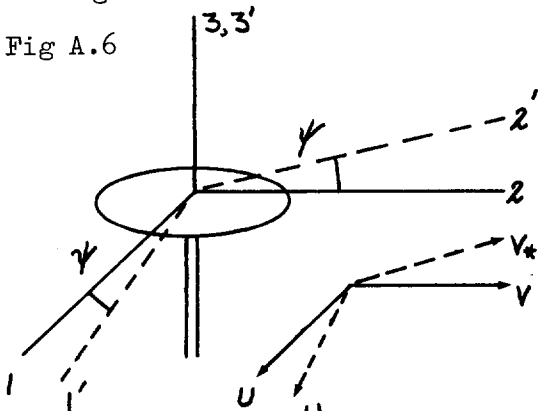
A rotation to midway between the extreme positions defined above would lead to a measurement of a zero shear stress at $\theta = 12\frac{1}{2}^{\circ}$ (and $-77\frac{1}{2}^{\circ}$).

All the results quoted in this section can be interpreted in terms of Mohr's stress circle introduced earlier. It is recalled, with particular reference to the case of the residual shear stress under waves, that a rotation of the head through some prescribed angle is likely to have a greater effect if the measured value of stress is small. Thus a rotation of the head for the values at $\approx$ 1m is likely to produce a change in the stress greater than the change at $\approx$ 30cms for the same rotation, as borne out in the results tabulated above.

A.6 Measurement of the direction of advance of a train of waves

In the experiment described earlier in the report, an EM Flowmeter was used to measure velocity components in the vertical 1'3'-plane given by the direction of wave advance. A check can be made to establish that the flowmeter lies in the correct vertical plane, if measurements are also made in the 1'2' plane.

Suppose that the waves travel in the 1-direction, but that the rig is aligned in such a way that the velocity components measured are (U_*, V_*) as defined in Fig A.6. The direction cosines in this case are

Fig A.6

$$\begin{pmatrix} \cos\psi & -\sin\psi & 0 \\ \sin\psi & \cos\psi & 0 \\ 0 & 0 & 1 \end{pmatrix} \tag{A.23}$$

and the measured stress tensor is now

$$\begin{pmatrix} \tau_{11}' & \tau_{12}' \\ \tau_{21}' & \tau_{22}' \end{pmatrix}$$

which is a reduced form of (A.2.) We can use transformation rule (A3) to deduce the results

$$\tau_{11}' = \tfrac{1}{2}\left(\tau_{11} + \tau_{22}\right) + \tfrac{1}{2}\left(\tau_{11} - \tau_{22}\right)\cos 2\psi + \tau_{12}\sin 2\psi$$

$$\tau_{22}' = \tfrac{1}{2}\left(\tau_{11} + \tau_{22}\right) + \tfrac{1}{2}\left(\tau_{22} - \tau_{11}\right)\cos 2\psi - \tau_{12}\sin 2\psi \qquad (A.24)$$

$$\tau_{12}' = \tau_{21}' = \tfrac{1}{2}\left(\tau_{22} - \tau_{11}\right)\sin 2\psi + \tau_{12}\cos 2\psi$$

In terms of velocity components the required transformations in the 12-plane are

$$U_* = U\cos\psi + V\sin\psi$$

$$V_* = V\cos\psi - U\sin\psi \qquad (A.25)$$

and so, writing $U = \bar{U} + u$, etc, we obtain

$$\rho\,\overline{U_* V_*} = \tfrac{1}{2}\rho\left(\bar{V}^2 + \overline{v^2} - \bar{U}^2 - \overline{u^2}\right)\sin 2\psi + \rho\left(\bar{U}\bar{V} + \overline{uv}\right)\cos 2\psi$$

Noting the equivalence of (A.16) and (A.2). Eq (A.24iii) can be recovered from this at once.

To find the angle ψ by which the head is misaligned, the simplest rule to adopt involves the minimization of the (wave induced) fluctuating component of velocity in the 12-plane; this minimum will define the perpendicular to the line of wave crest advance. (We must accept the possibility of a non-zero $\bar{V}$ since, in practice, a steady transverse current may be present. Also, in the simple approach discussed here, the possibility of any wave/current interaction is ignored.) The object of the exercise can most easily be achieved if $\overline{V^2}$ is minimized subject to the conditions (introduced for convenience):

$$\overline{U_*^2} > \overline{V_*^2} \qquad \text{and} \qquad |\psi| < \frac{\pi}{4} \qquad (A.26)$$

Neither of these conditions imposes too harsh a restriction and both could be relaxed quite simply if necessary. Thus

$$\frac{d}{d\psi}\left(\overline{V^2}\right) = 0 \qquad \text{when} \qquad \tan 2\psi = \frac{2\,\overline{U_* V_*}}{\overline{V_*^2} - \overline{U_*^2}} \qquad (A.27)$$

and the value of ψ given by (A.27) can be shown to give a minimum in $\overline{V^2}$ if conditions (A.26) are satisfied. It can be shown directly that for this choice of ψ a maximum arises in $\overline{U^2}$, again under conditions (A.26), since

$$\frac{d^2}{d\psi^2}\left(\overline{U^2}\right) = -\frac{d^2}{d\psi^2}\left(\overline{V^2}\right).$$

Thus to ensure that measurements are being made in the desired vertical plane, we seek an angle ψ defined in Fig A.6 and calculated by means of (A.27). It should be stressed that the criterion leading to (A.27) is not the same as that which would be required in considering the calculation of shear stress in the 12-plane; for this purpose a criterion of the kind described in the earlier sections is needed.

A.7 Consequences of measurement in the incorrect vertical plane

Following consideration of the types of rotation depicted in Figs A.2 and A.6, consider now a third special case. The rotation is such that the stem of the flowmeter is positioned in the 12-plane as shown in Fig A.7, and we measure the stress in the 1'3'-plane. The direction cosines are:

Fig A.7
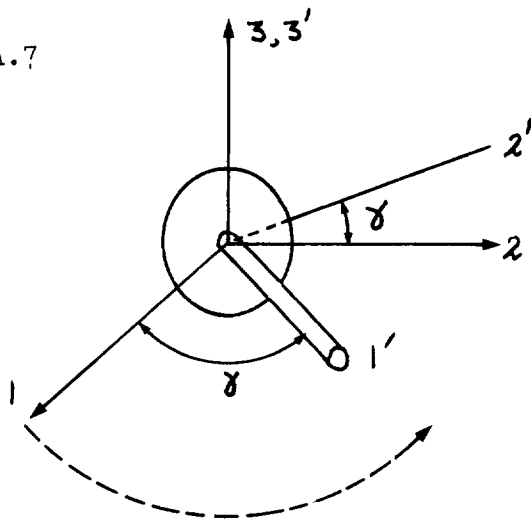
$$\begin{pmatrix} \cos\gamma & -\sin\gamma & 0 \\ \sin\gamma & \cos\gamma & 0 \\ 0 & 0 & 1 \end{pmatrix}$$

in other words, exactly the same set as (A.23). We are now interested in the stresses in the 1'3'-plane however, and using (A.3) it can be shown that

$$\gamma'_{13} = \gamma'_{31} = \cos\gamma\ \gamma_{13} + \sin\gamma\ \gamma_{23}$$

Here the measured shearing stress is a combination of two shear stresses acting on mutually orthogonal planes. Clearly this result is comparable with (A.10) and (A.12). We can conclude that the measured information is insufficient to recover the stress on either of the planes 13 or 23.

A.8 The effect of a rotation of axes on energy spectra and cross-spectra

The discussion in Sections A.2 and A.4 can be extended to cover the effects of a rotation of axes on energy spectra and cross-spectra. Initially, in this Section, results are stated for a simple rotation of axes in two dimensions, with reference to the problems which arise using an EM flowmeter. It is shown that spectra of U and W and the co-spectrum of U and W are affected by a rotation of the EM measuring head, but that the quad-spectrum is not. The results obtained are then generalised for the three-dimensional case.

In developing spectra in Chapter 5, we examined the frequency compositions of the variances of the fluctuating components of the measured velocity field, $\overline{u_*^2}$ and $\overline{w_*^2}$, and of the co-variance $\overline{u_* w_*}$. Using (A.17), the "desired" signal variances and co-variance can be expressed in terms of the measured velocity components as

$$
\left.
\begin{aligned}
\overline{u^2} &= \tfrac{1}{2}\left(\overline{u_*^2} + \overline{w_*^2}\right) + \tfrac{1}{2}\left(\overline{u_*^2} - \overline{w_*^2}\right)\cos 2\theta - \overline{u_* w_*}\sin 2\theta \\
\overline{w^2} &= \tfrac{1}{2}\left(\overline{u_*^2} + \overline{w_*^2}\right) + \tfrac{1}{2}\left(\overline{w_*^2} - \overline{u_*^2}\right)\cos 2\theta + \overline{u_* w_*}\sin 2\theta \\
\overline{uw} &= \overline{u_* w_*}\cos 2\theta + \tfrac{1}{2}\left(\overline{u_*^2} - \overline{w_*^2}\right)\sin 2\theta
\end{aligned}
\right\} \text{(A.28)}
$$

If we now restrict our comments to a single general frequency, the rth harmonic with frequency ω_r, we can write

$$
\left.
\begin{aligned}
u_*(\omega_r) &= a_r \cos \omega_r t + b_r \sin \omega_r t \\
w_*(\omega_r) &= c_r \cos \omega_r t + d_r \sin \omega_r t
\end{aligned}
\right\} \text{(A.29)}
$$

Ultimately we can superimpose linearly over all the harmonics present in the flow field to obtain the results desired. It follows from (A.29) that

$$
\overline{u_*^2(\omega_r)} = \tfrac{1}{2}\left(a_r^2 + b_r^2\right) \tag{A.30}
$$

$$
\overline{w_*^2(\omega_r)} = \tfrac{1}{2}\left(c_r^2 + d_r^2\right) \tag{A.31}
$$

$$
\overline{u_*(\omega_r).w_*(\omega_r)} = \tfrac{1}{2}\left(a_r c_r + b_r d_r\right) \tag{A.32}
$$

If we now adopt RAYMENT's notation (using a dash to indicate a measured spectrum), we have at the rth frequency:

(i) the contributions to the power spectra:

$$ S_u'(r) = \tfrac{T}{2}\left(a_r^2 + b_r^2\right) \tag{A.33} $$

$$ S_w'(r) = \tfrac{T}{2}\left(c_r^2 + d_r^2\right) \tag{A.34} $$

(ii) the contribution to the co-spectrum:

$$ S_{uw}'(r) = \tfrac{T}{2}\left(a_r c_r + b_r d_r\right) \tag{A.35} $$

(iii) the contribution to the quad-spectrum:

$$ Q_{uw}'(r) = \tfrac{T}{2}\left(b_r c_r - a_r d_r\right) \tag{A.36} $$

where T is the total sampling time. These definitions in combination with (A.28) give

$$
\overline{u^2(\omega_r)} = \frac{S_u(r)}{T} = \tfrac{1}{2}\left(\frac{S_u'(r)}{T} + \frac{S_w'(r)}{T}\right) + \tfrac{1}{2}\left(\frac{S_u'(r)}{T} - \frac{S_w'(r)}{T}\right)\cos 2\theta - S_{uw}'(r)\sin 2\theta \tag{A.37}
$$

$$
\overline{w^2(\omega_r)} = \frac{S_w(r)}{T} = \tfrac{1}{2}\left(\frac{S_u'(r)}{T} + \frac{S_w'(r)}{T}\right) + \tfrac{1}{2}\left(\frac{S_w'(r)}{T} - \frac{S_u'(r)}{T}\right)\cos 2\theta + S_{uw}'(r)\sin 2\theta \tag{A.38}
$$

and indicate the effect of rotation through an angle θ (in the sense of Fig A.6) on the rth energy estimate in the spectrum. Similarly, we have in relation to the co-spectrum

$$
\overline{u(\omega_r)w(\omega_r)} = \frac{S_{uw}'(r)}{T}\cos 2\theta + \tfrac{1}{2}\left(\frac{S_u'(r)}{T} - \frac{S_w'(r)}{T}\right)\sin 2\theta \tag{A.39}
$$

To examine the rth quad-spectral estimate we note initially that (A.36) is consistent with the adoption of a phase lag of $\frac{\pi}{2}$ in $u_*(\omega_r)$ as follows

$$\overline{u_*(\omega_r)\Big|_{\frac{\pi}{2}\text{lag}} w_*(\omega_r)} = \overline{(-a_r \sin\omega_r t + b_r \cos\omega_r t)(c_r \cos\omega_r t + d_r \sin\omega_r t)}$$
$$= -\frac{1}{2}\left(a_r d_r - b_r c_r\right)$$

In writing $Q'_{uw}(r)$ we therefore accept as our convention the application of a $\pi/_2$ phase shift in the quantity indicated by the first suffix, u. Using (A.17), it is then simply shown that

$$\overline{u(\omega_r)\Big|_{\frac{\pi}{2}\text{lag}} w(\omega_r)} = \frac{Q_{uw}(r)}{T} = \overline{\left(u_*(\omega_r)\cos\theta - w_*(\omega_r)\sin\theta\right)\Big|_{\frac{\pi}{2}\text{lag}}\left(w_*(\omega_r)\cos\theta + u_*(\omega_r)\sin\theta\right)}$$

$$= \overline{u_*(\omega_r)\Big|_{\frac{\pi}{2}\text{lag}} w_*(\omega_r)}$$

$$= -\frac{1}{2}\left(a_r d_r - b_r c_r\right) = \frac{Q'_{uw}(r)}{T} \qquad \text{(A.40)}$$

In other words, the rth quad-spectral estimate, and hence the quad-spectrum itself, is unaffected by the simple rotation of axes indicated in Fig A.6. On the other hand, the energy spectra and co-spectrum are affected as indicated in (A.37) – (A.39). The result (A.40) is explained on the argument that the quadrature spectrum expresses the level of uncorrelated activity on a plane in the fluid and is in this sense not a directional quantity. The spectral estimators in (A.37) – (A.40) can ultimately be superimposed over all the 'r' frequencies present to obtain the complete spectra.

Let us now generalise these results to three dimensions. It is convenient initially to write the stress tensor (A.16) in the form

$$\overline{\rho\left(\bar{U}+u,\ \bar{V}+v,\ \bar{W}+w\right)\begin{pmatrix}\bar{U}+u\\ \bar{V}+v\\ \bar{W}+w\end{pmatrix}} \qquad \text{(A.41)}$$

where the overbar denotes time averaging. This tensor can be viewed as comprising the in-phase parts of the nine product terms, $(\bar{U}+u)(\bar{U}+u)$, etc. We can now extend the notation introduced in (A.33) – (A.36) in the following way for the measured quantities.

Taking the rth harmonic only, we can write the measured stress tensor as

$$\rho\begin{pmatrix}\overline{u_*^2} & \overline{u_* v_*} & \overline{u_* w_*}\\ \overline{v_* u_*} & \overline{v_*^2} & \overline{v_* w_*}\\ \overline{w_* u_*} & \overline{w_* v_*} & \overline{w_*^2}\end{pmatrix}_r \qquad \text{(A.42)}$$

52

Using (A.30) - (A.35) and recalling (A.2) we see that this can be expressed
alternatively

$$
\tau_m' \Big|_r = \begin{pmatrix} \tau_{11}' & \tau_{12}' & \tau_{13}' \\ \tau_{21}' & \tau_{22}' & \tau_{23}' \\ \tau_{31}' & \tau_{32}' & \tau_{33}' \end{pmatrix}_r = \frac{\rho}{T} \begin{pmatrix} S_u & S_{uv} & S_{uw} \\ S_{vu} & S_v & S_{vw} \\ S_{wu} & S_{wv} & S_w \end{pmatrix}_r
\tag{A.43}
$$

The measured stress is symmetrical with $\tau_{ij}' = \tau_{ji}'$, $i=1,3$, $j=1,3$ (see Section A.2).

Pursuing the same argument for the quadrature spectral estimates, we proceed from
(A.41) by imposing a phase shift of $\frac{\pi}{2}$ at the rth frequency as follows:

$$
\rho \big(u_*(\omega_r) \quad v_*(\omega_r) \quad w_*(\omega_r) \big) \begin{pmatrix} u_*(\omega_r)\big|_{\pi/2\,lag} \\ v_*(\omega_r)\big|_{\pi/2\,lag} \\ w_*(\omega_r)\big|_{\pi/2\,lag} \end{pmatrix}
\tag{A.44}
$$

Using the double suffix notation introduced above (such that the phase lag is
applied to the quantity indicated by the first suffix) and adopting an R_{ij}'
notation for purposes of comparability with the τ_{ij}', we can express (A.44)

$$
R_m' \Big|_r = \begin{pmatrix} R_{11}' & R_{12}' & R_{13}' \\ R_{21}' & R_{22}' & R_{23}' \\ R_{31}' & R_{32}' & R_{33}' \end{pmatrix}_r = \frac{\rho}{T} \begin{pmatrix} 0 & Q_{uv} & Q_{uw} \\ Q_{vu} & 0 & Q_{vw} \\ Q_{wu} & Q_{wv} & 0 \end{pmatrix}_r
\tag{A.45}
$$

In (A.45) we have $R_{ii}' = 0$, $i=1,3$, (as can be simply shown from (A.29) by
setting $a_r = c_r$ and $b_r = d_r$ in (A.36)). It can also be shown that $R_{ij}' = -R_{ji}'$, $i \neq j$, $i=1,3$, $j=1,3$.

The rotation of tensor (A.2) according to the rule (A.3) has been discussed
earlier. The rotation of (A.45) to its desired form can similarly be accomplished
by the transformation

$$
R_{ji}' = \ell_{ij}\,\ell_{k\ell}\,R_{ik}
$$

Since the measured tensor R_m' is antisymmetrical, the desired tensor R will also
be antisymmetrical and have the properties

$$
\begin{aligned}
R_{ii} &= 0 & i &= 1,3 \\
R_{ij} &= -R_{ji} & i &\neq j, \quad i=1,3, \quad j=1,3
\end{aligned}
$$

We note that, in general, $R_{ij} \neq R_{ij}'$ $(i \neq j)$.

It is convenient finally to define the measured complex frequency or spectral
density function, φ_{ij}', as follows:

$$
\varphi_{ij}' = \tau_{ij}' + i\,R_{ij}'
\tag{A.46}
$$

Writing $\phi'_{ab} = S'_{ab} + i\, Q'_{ab}$, $a \neq b$, and $\phi'_{aa} = S'_a$, we have from (A.43) and (A.45)

$$\phi'_M = \begin{pmatrix} \phi'_{11} & \phi'_{12} & \phi'_{13} \\ \phi'_{21} & \phi'_{22} & \phi'_{23} \\ \phi'_{31} & \phi'_{32} & \phi'_{33} \end{pmatrix} = \frac{\rho}{T}\begin{pmatrix} \Phi_{uu} & \Phi_{uv} & \Phi_{uw} \\ \Phi_{vu} & \Phi_{vv} & \Phi_{vw} \\ \Phi_{wu} & \Phi_{wv} & \Phi_{ww} \end{pmatrix} \qquad (A.47)$$

From the properties established above, we have in (A.47)

(i) $\quad \mathcal{I}_m \; \phi'_{ii} = 0 \qquad i = 1,3.$

(ii) $\quad \mathcal{I}_m \; \phi'_{ij} = - \mathcal{I}_m \; \phi'_{ji} \qquad i \neq j, \; i = 1,3, \; j = 1,3.$

A rotation of axes in (A.47) according to the rule $\quad \phi'_{ji} = \ell_{ij}\, \ell_{k\ell}\, \phi_{ik}$, causes, in the imaginary parts:

(i) no change along the leading diagonal: $\mathcal{I}_m \; \phi_{ii} = 0$, $i = 1,3.$

(ii) the preservation of the antisymmetrical structure of the tensor with

$$\mathcal{I}_m \; \phi_{ij} = - \mathcal{I}_m \; \phi_{ji} \quad, \quad i \neq j, \; i = 1,3, \; j = 1,3.$$

and, in the real parts:

(iii) the preservation of the symmetrical structure of the tensor with

$$\mathcal{R}_e \; \phi_{ij} = \mathcal{R}_e \; \phi_{ji} \quad, \quad i = 1,3, \; j = 1,3.$$

The superimposition of spectral contributions over all r frequencies is required to build up the complete picture of the flow field.

A.9 Conclusions

In measuring the shearing stress in a turbulent water flow, with an EM Flowmeter or any other two component velocity measuring device, the utmost care must be taken in interpreting the results. A failure to determine correctly the relationship between the plane on which the stress in the fluid is to be calculated and the plane on which the stress was effectively measured may lead to large errors. This comment can be extended both to the spectral estimates of the energy in the two velocity components when these are taken separately, and to the co-spectral estimates of the two components. However, in any given plane, the estimates in the quad-spectrum are independent of the orientation of the two rectangular axes of measurement.

It is also clear that an accurate knowledge of the zeroes on the velocity scales is essential if reliable residual shear stress information is to be obtained, especially for oscillatory flows with low mean velocities. Such a knowledge was not available in producing the results in the main body of the report.

ARRANGEMENT OF EQUIPMENT ON SEABED AND DEFINITION OF AXES

P_1 Pressure Transducer

Electromagnetic Flowmeter Heads

U_U

W_U

U_L

W_L

'Z' Axis

Television Camera

'X' Axis

direction of wave advance

Ripples

Sand

Cables to Beach

P_2 Pressure Transducer
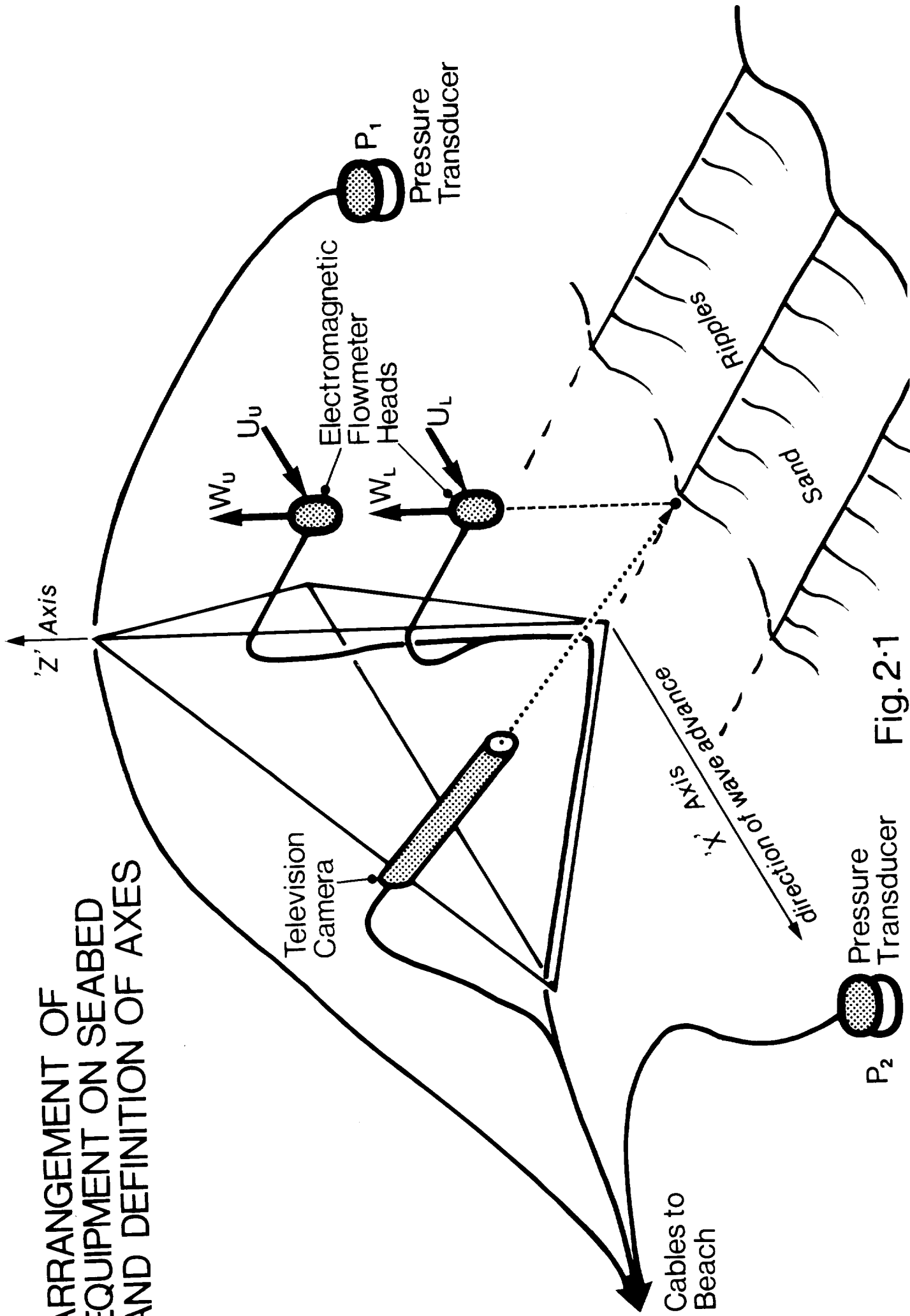
Fig. 2·1
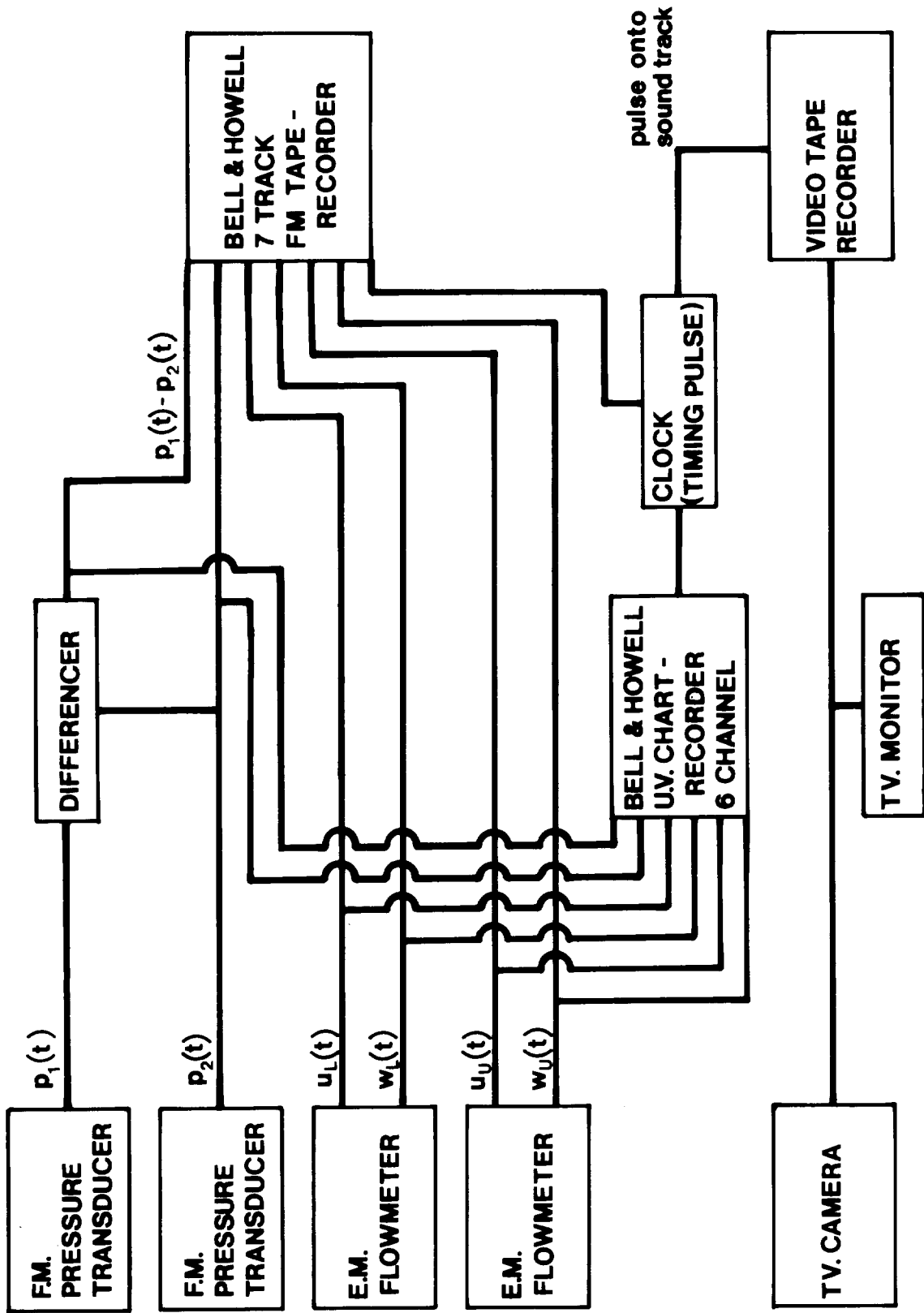
FIG 2.2   Block diagram of transducers and electronic recording apparatus
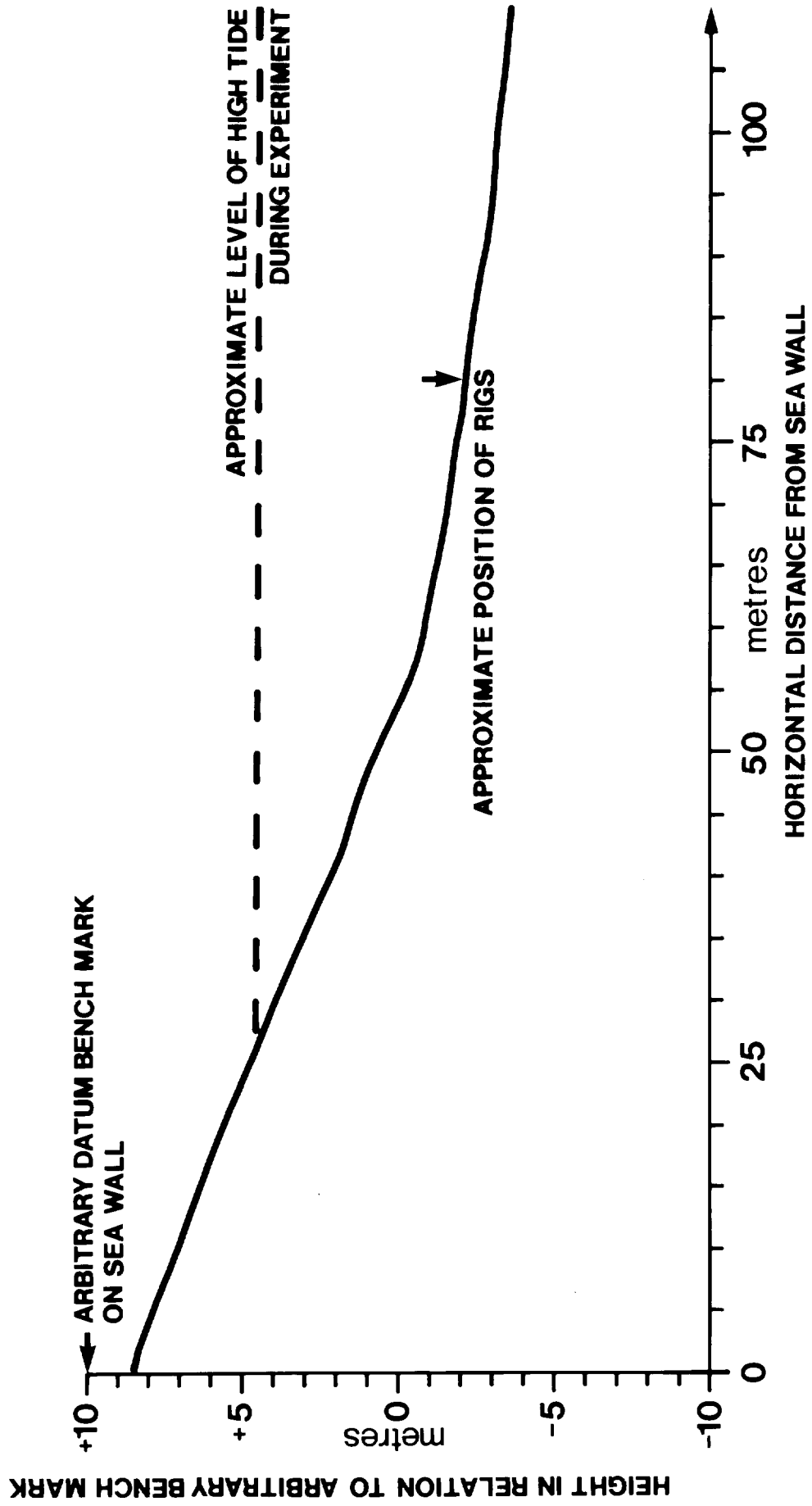
FIG 3.1 Beach profile and nearshore bottom topography

HEIGHT IN RELATION TO ARBITRARY BENCH MARK

ARBITRARY DATUM BENCH MARK ON SEA WALL

APPROXIMATE LEVEL OF HIGH TIDE DURING EXPERIMENT

APPROXIMATE POSITION OF RIGS

HORIZONTAL DISTANCE FROM SEA WALL

metres
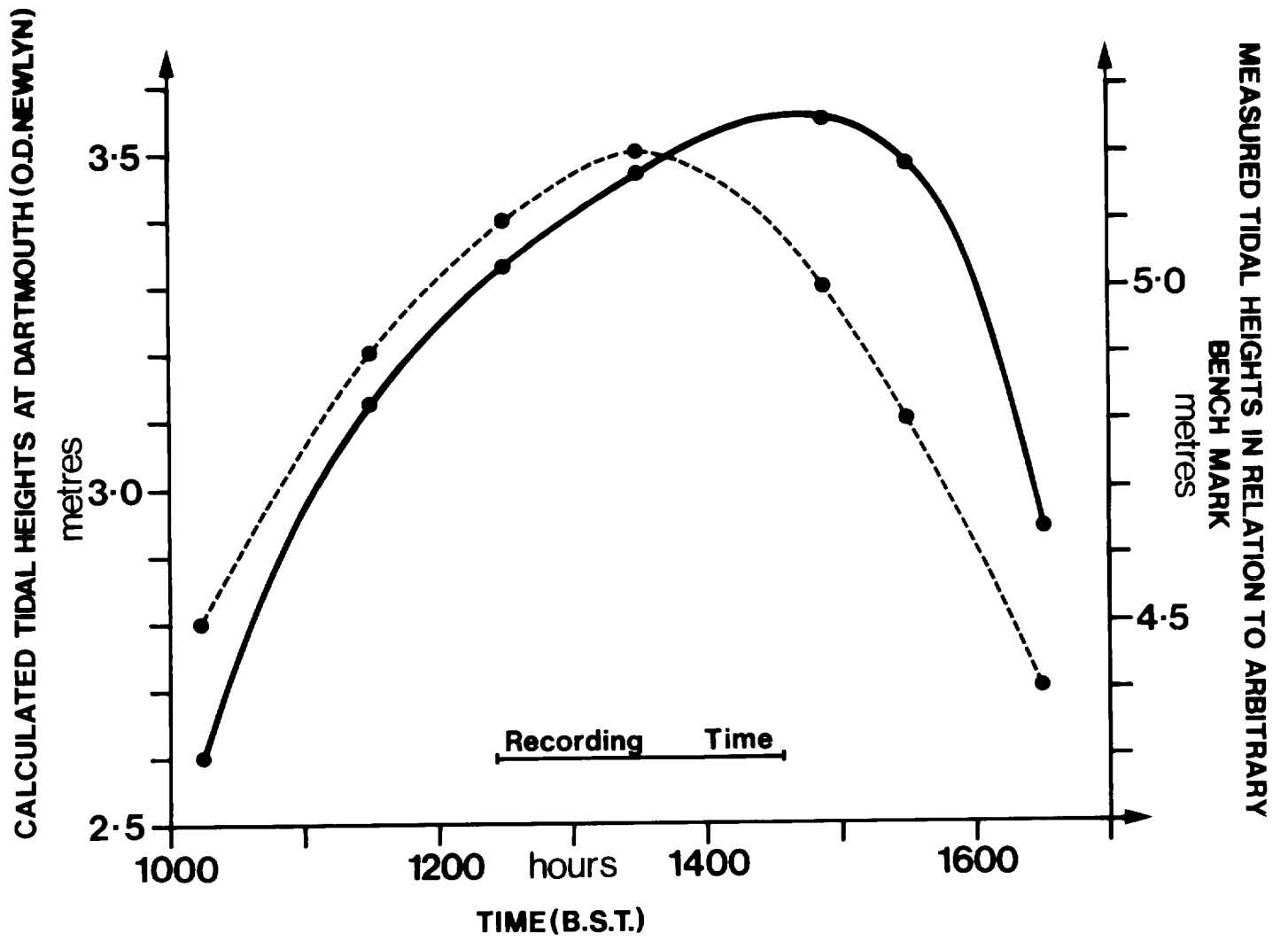
FIG 3.2   Tidal height during the experiment (22 March 1977)
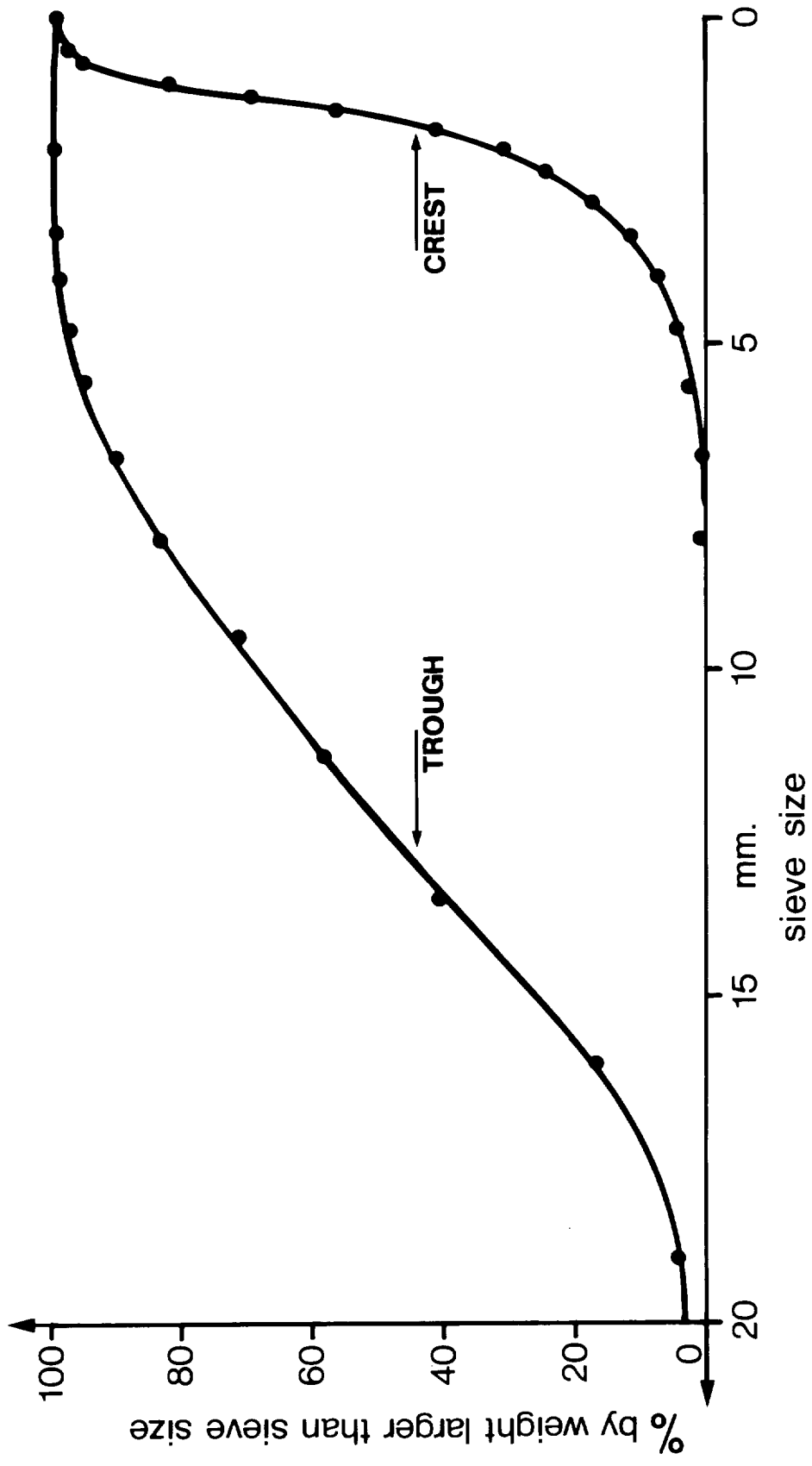
FIG 3.3   Grain size sieve analysis

1 metre (approx)

Camera housing

Upper frame

Lower frame

Rollers

Horizontal parallel calibration rods

Square topped pegs
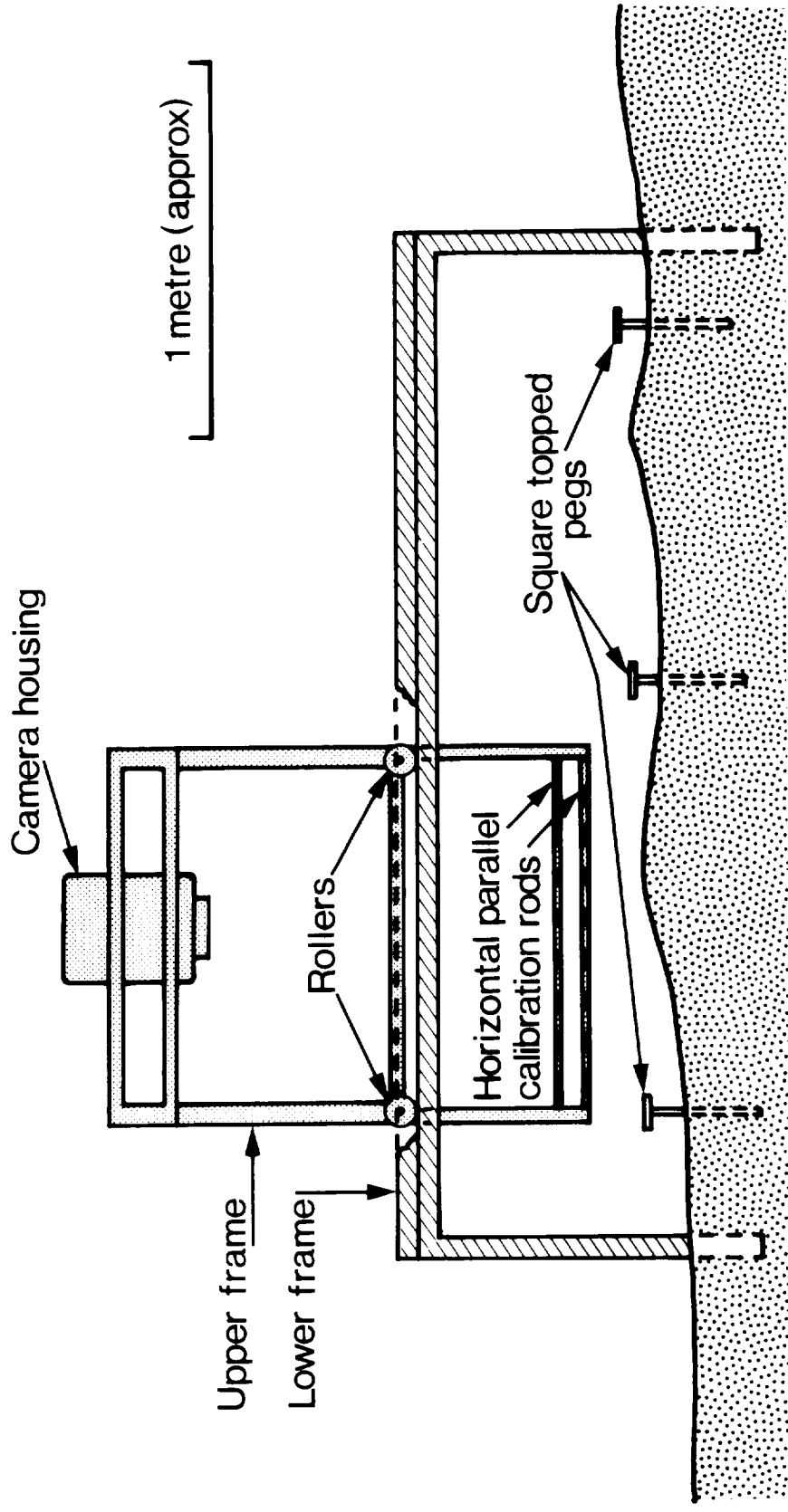
FIG 3.4   Layout of photogrammetric equipment
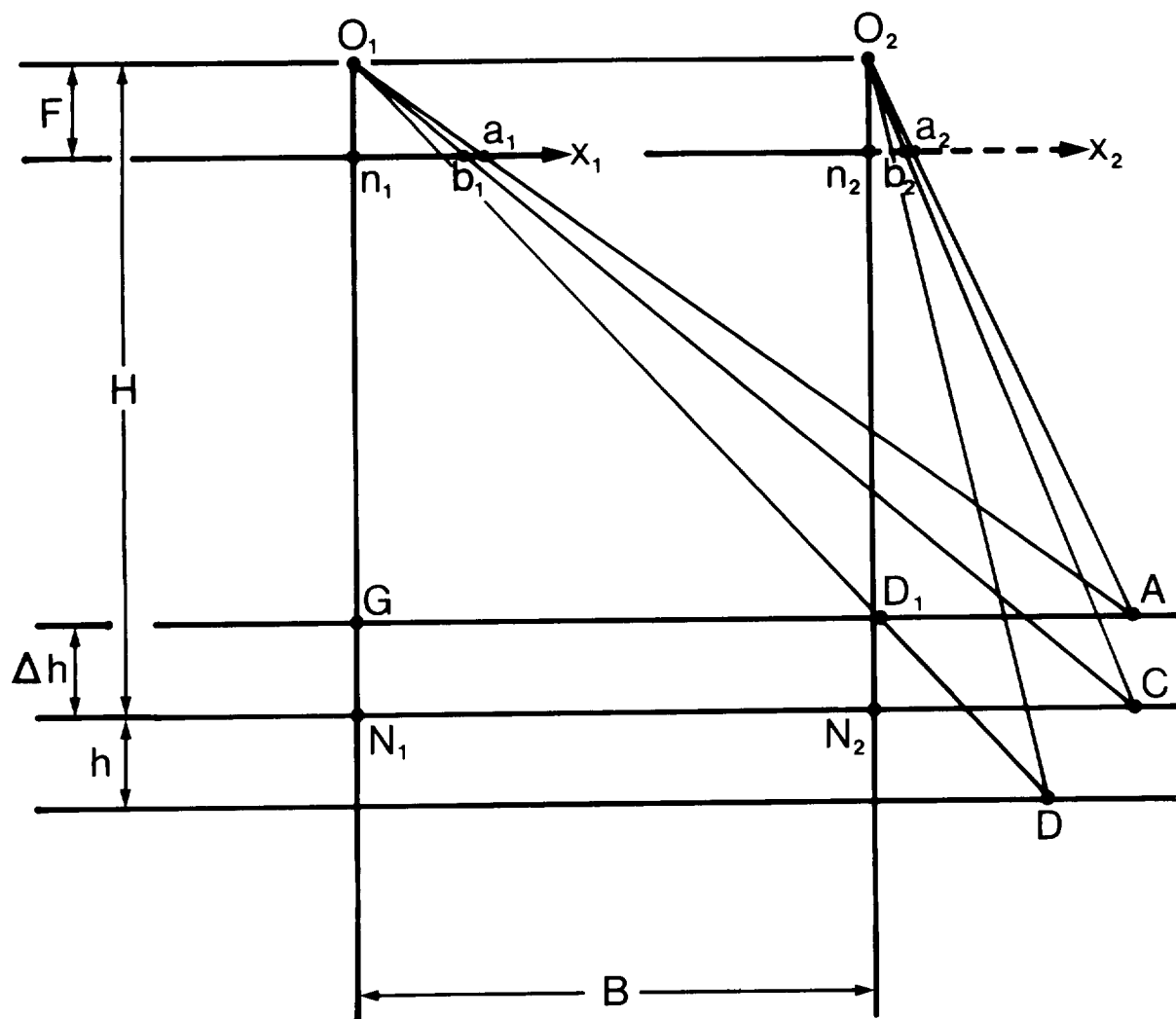
FIG 3.5   Geometrical relations for a vertical pair of stereophotographs

Fig 3.6

A Typical Stereo Pair

PROFILE MAINTAINED DURING EXPERIMENT
13·45 to 16·15 , 23rd March 1975.
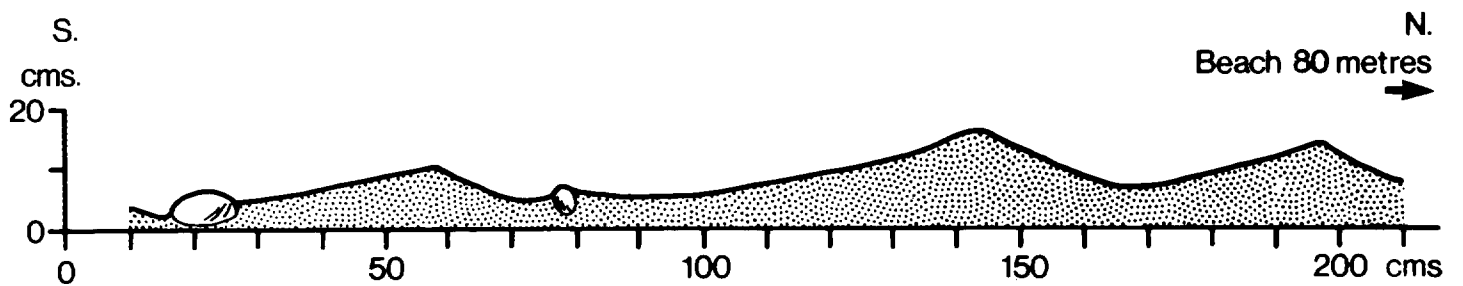
Fig 3.7

The Ripple Profile
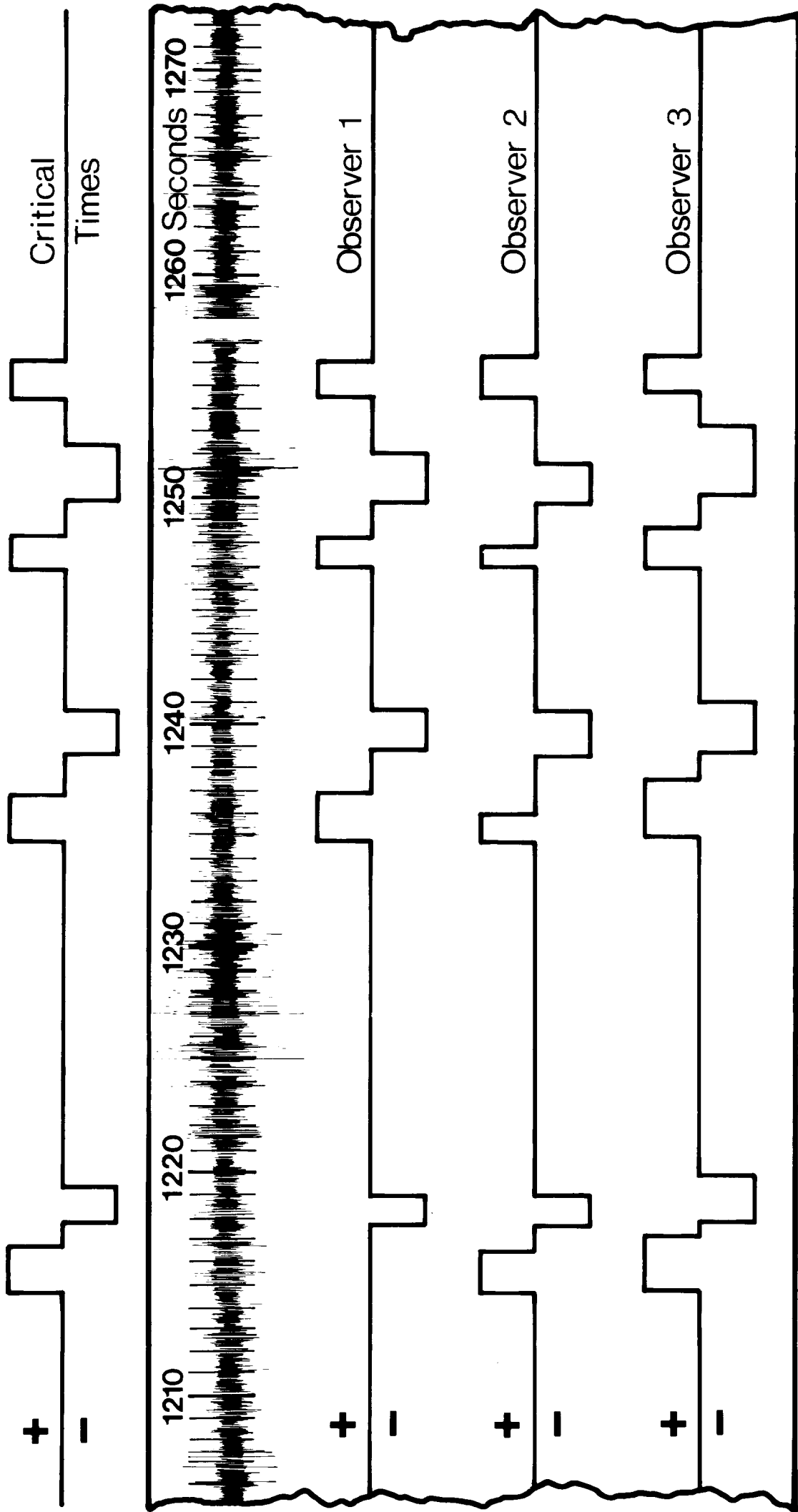
FIG 4.1 Estimated times of shoreward (+) and seaward (−) sediment motion during a typical part of the experiment
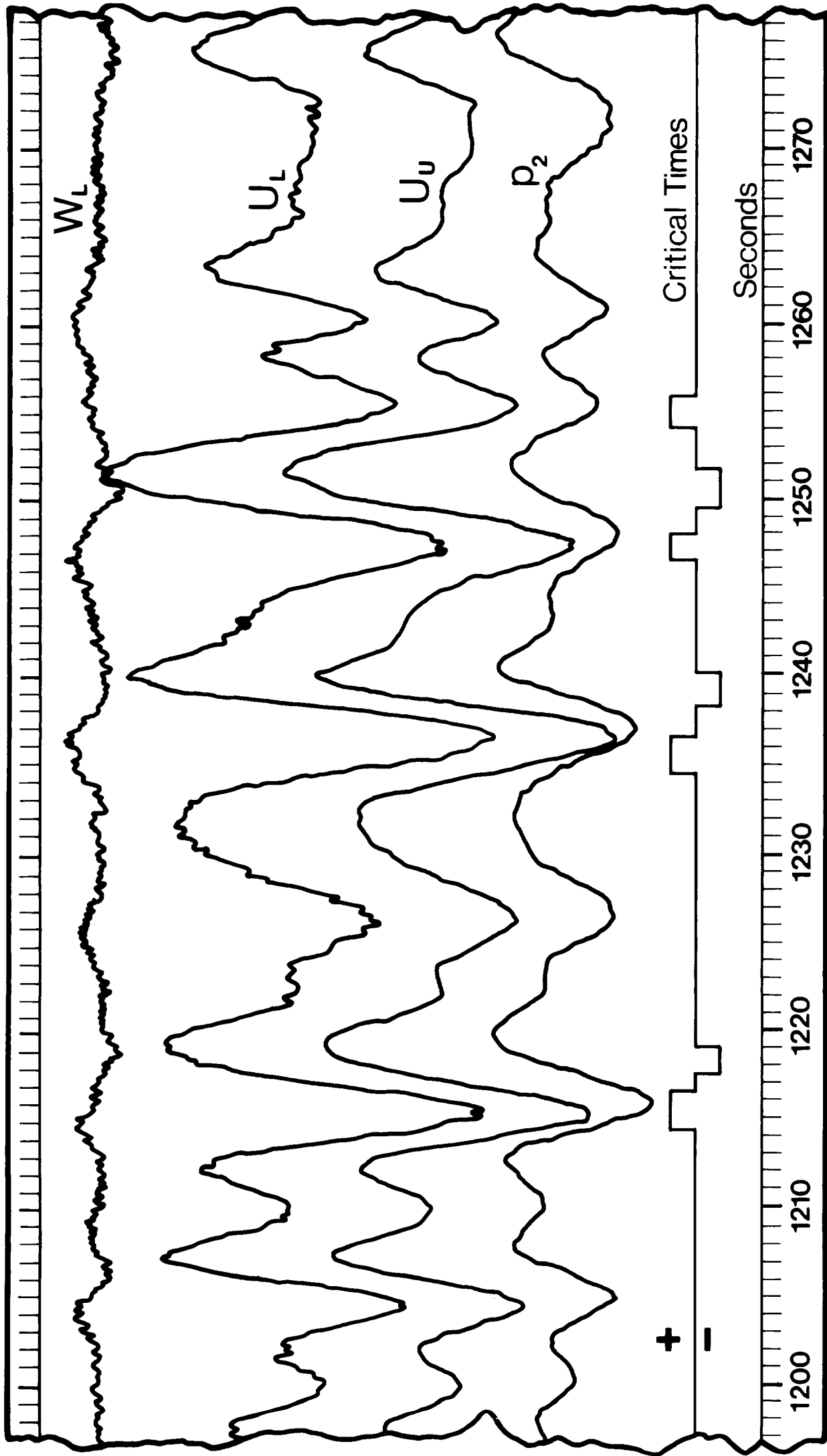
FIG 4.2   An example of the analogue traces of four of the basic variables and the estimated times of sediment motion taken from Fig 4.1
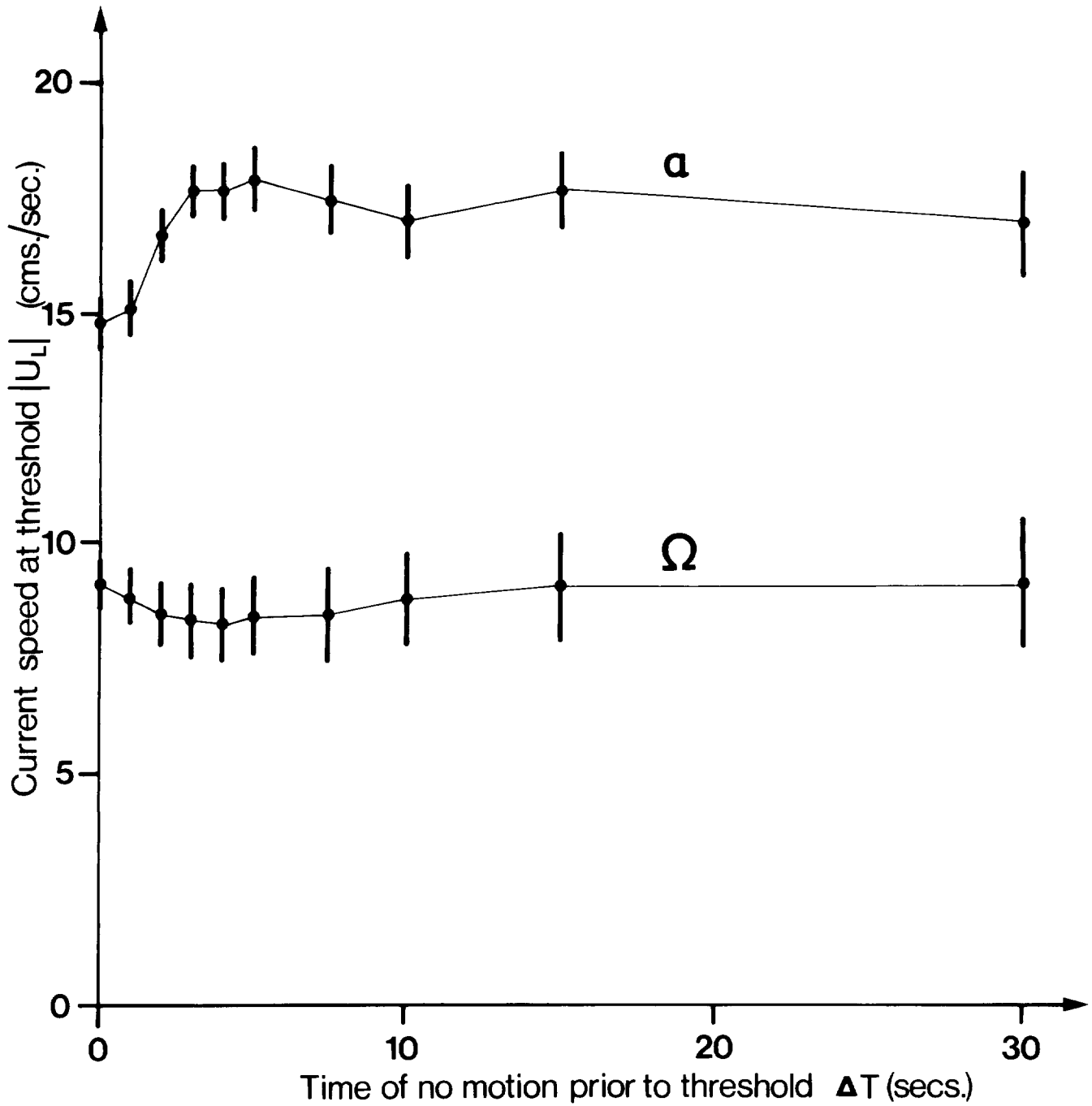
FIG 5.1   Variation of threshold speed with ΔT at initiation and termination of motion, for the case of u_L (negative).

Standard errors are indicated by vertical bars.
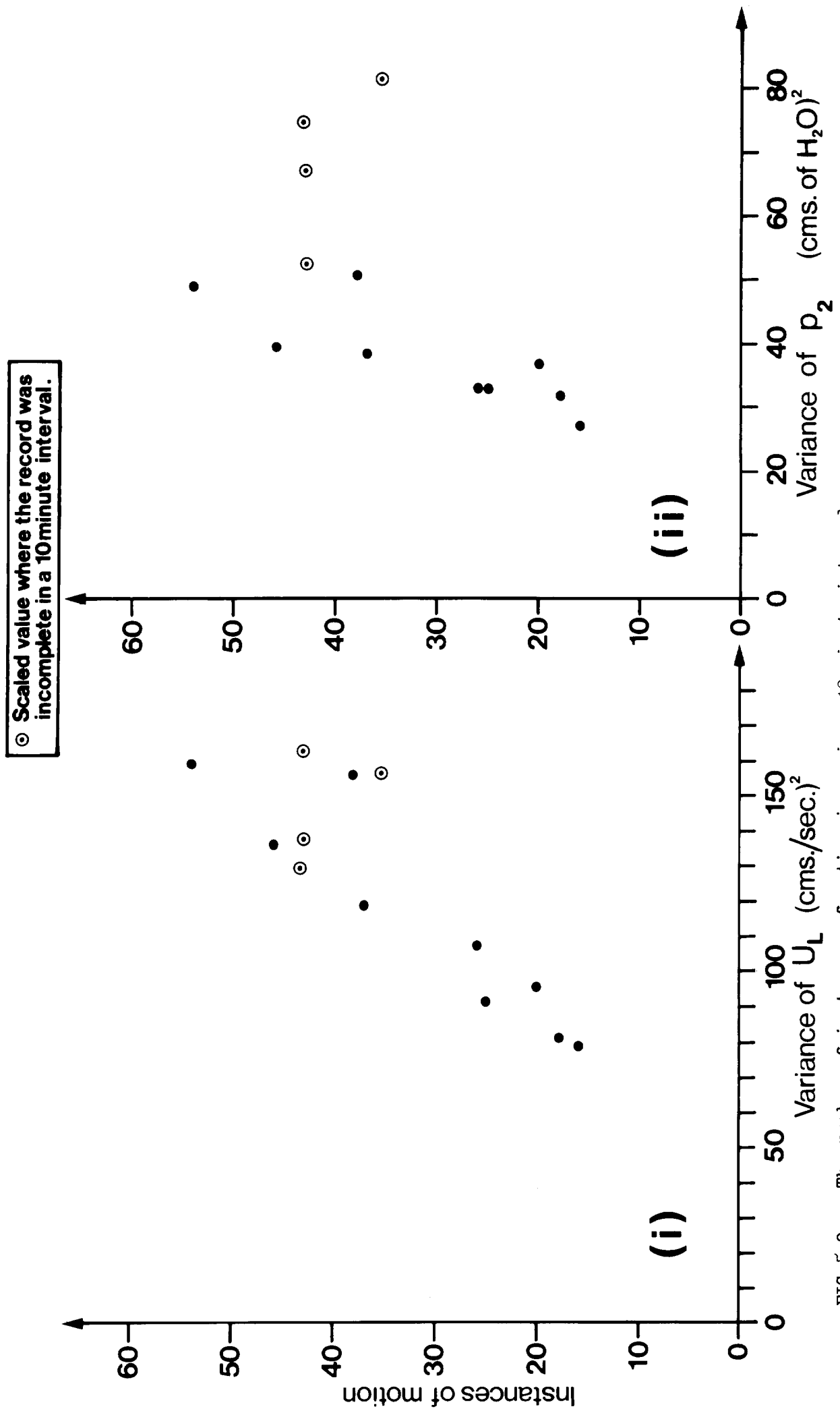
FIG 5.2   The number of instances of motion in a given 10 minute interval plotted against the variance (i) of u_L and (ii) of p_2
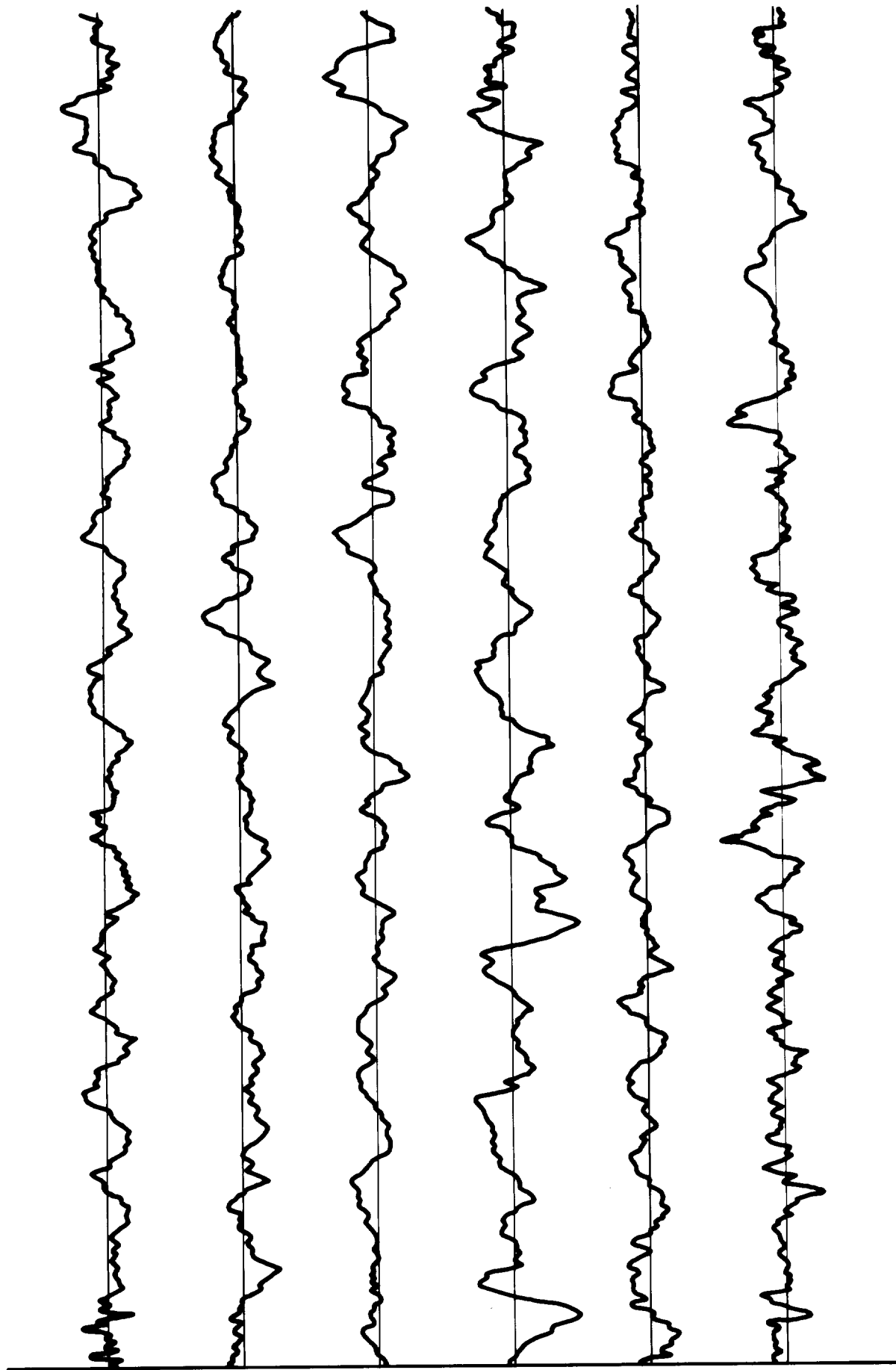
FIG 5.3   Trace of W_L plotted about its mean over the 10 minute interval.

Signal variance 1.4 $(cms/sec)^2$.
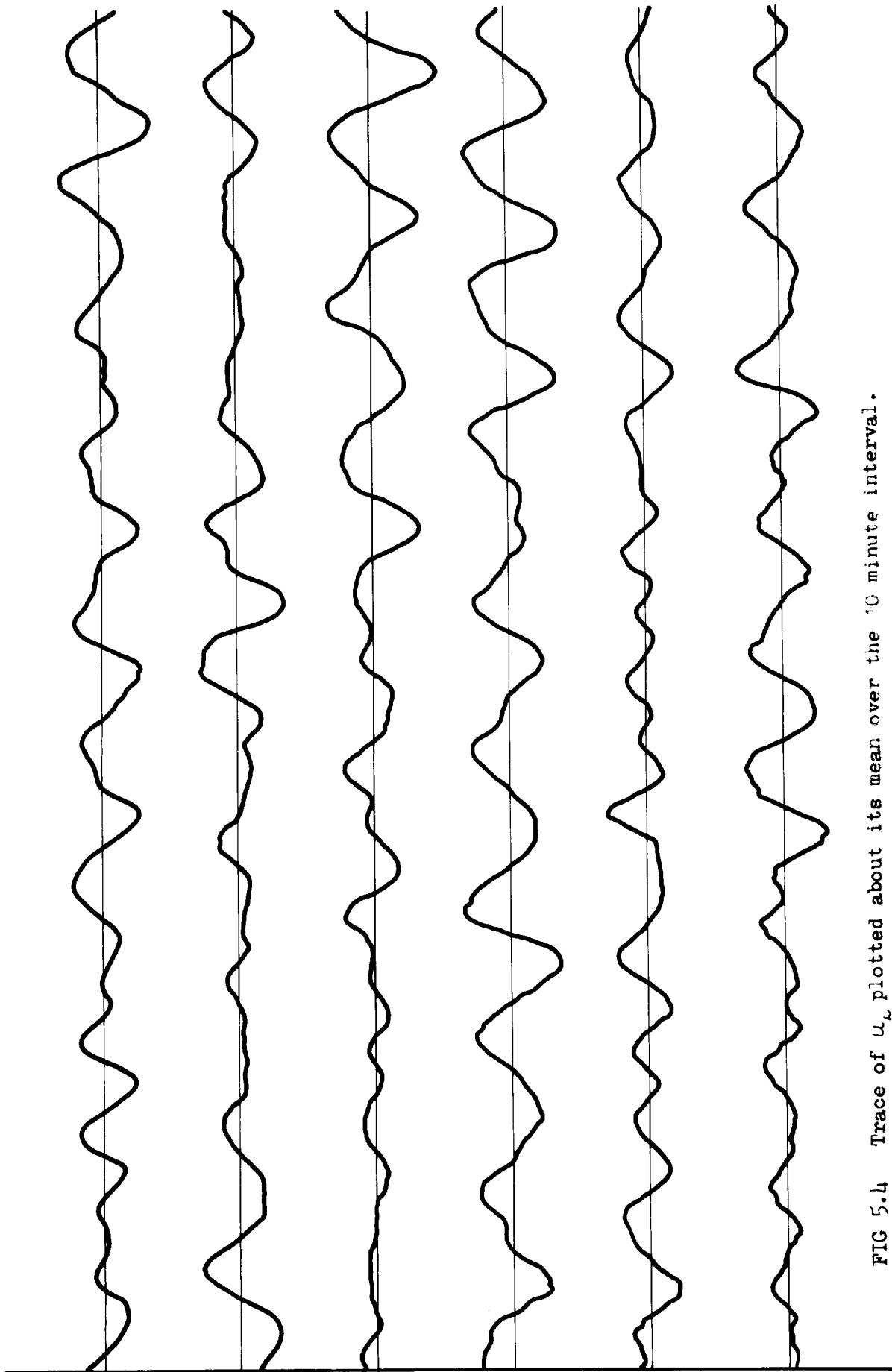
FIG 5.4   Trace of u_L plotted about its mean over the 10 minute interval.

Signal variance 152.5 $(cms/sec)^2$.
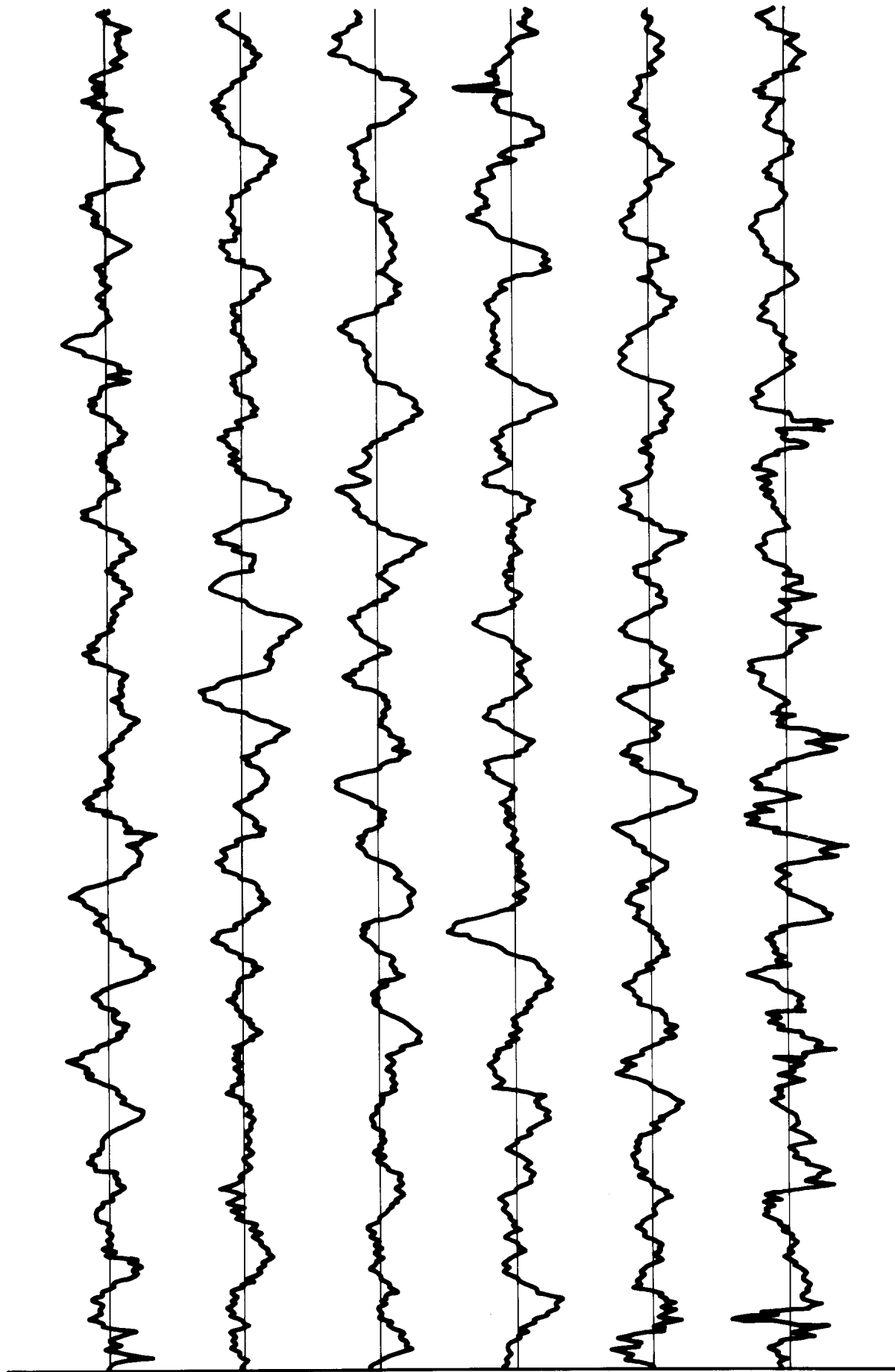
FIG 5.5   Trace of w_u plotted about its mean over the 10 minute interval.

Signal variance 1.3 $(cms/sec)^2$.
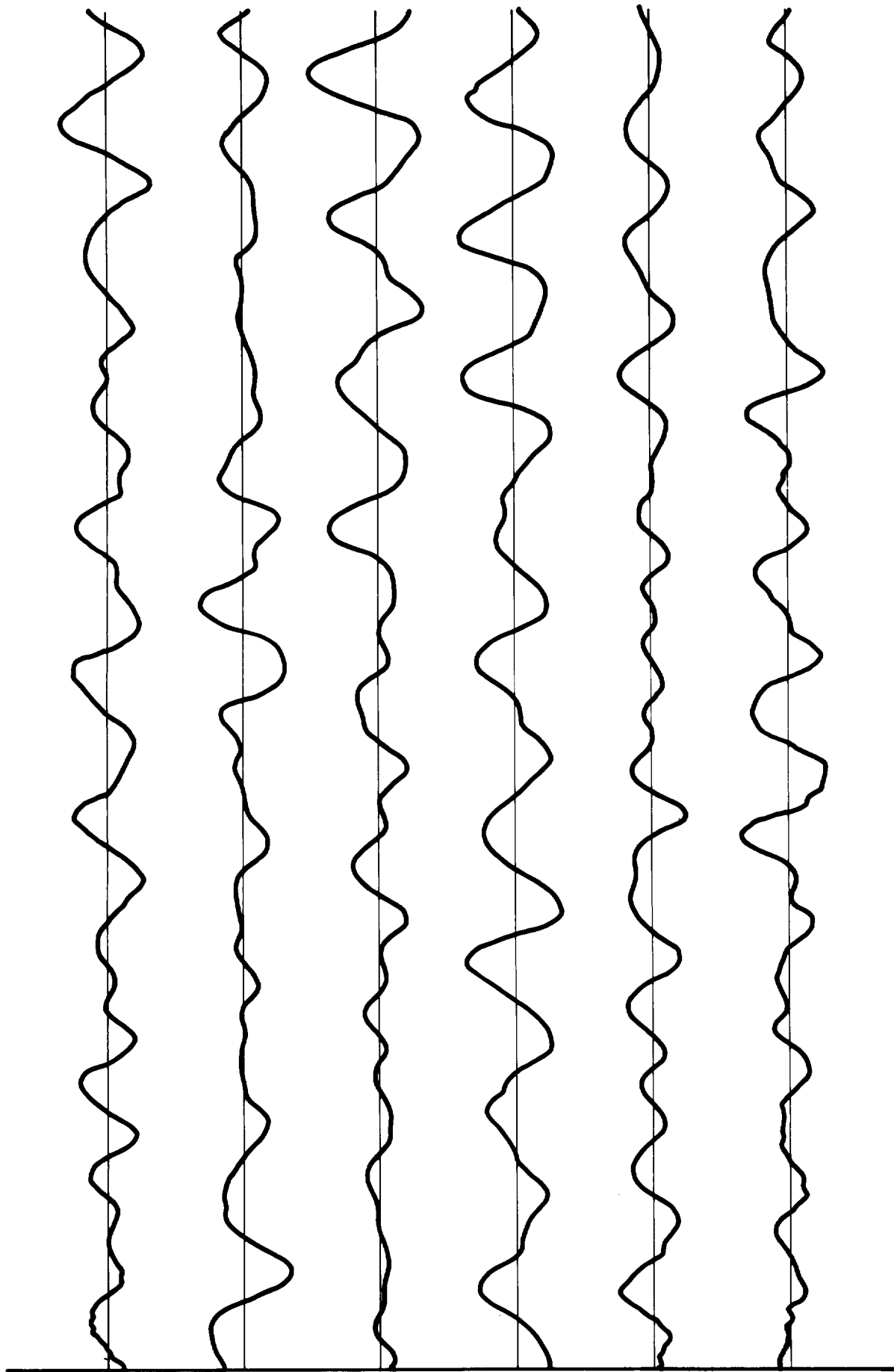
FIG 5.6   Trace of u_v plotted about its mean over the 10 minute interval.

Signal variance 134.5 $(cms/sec)^2$.
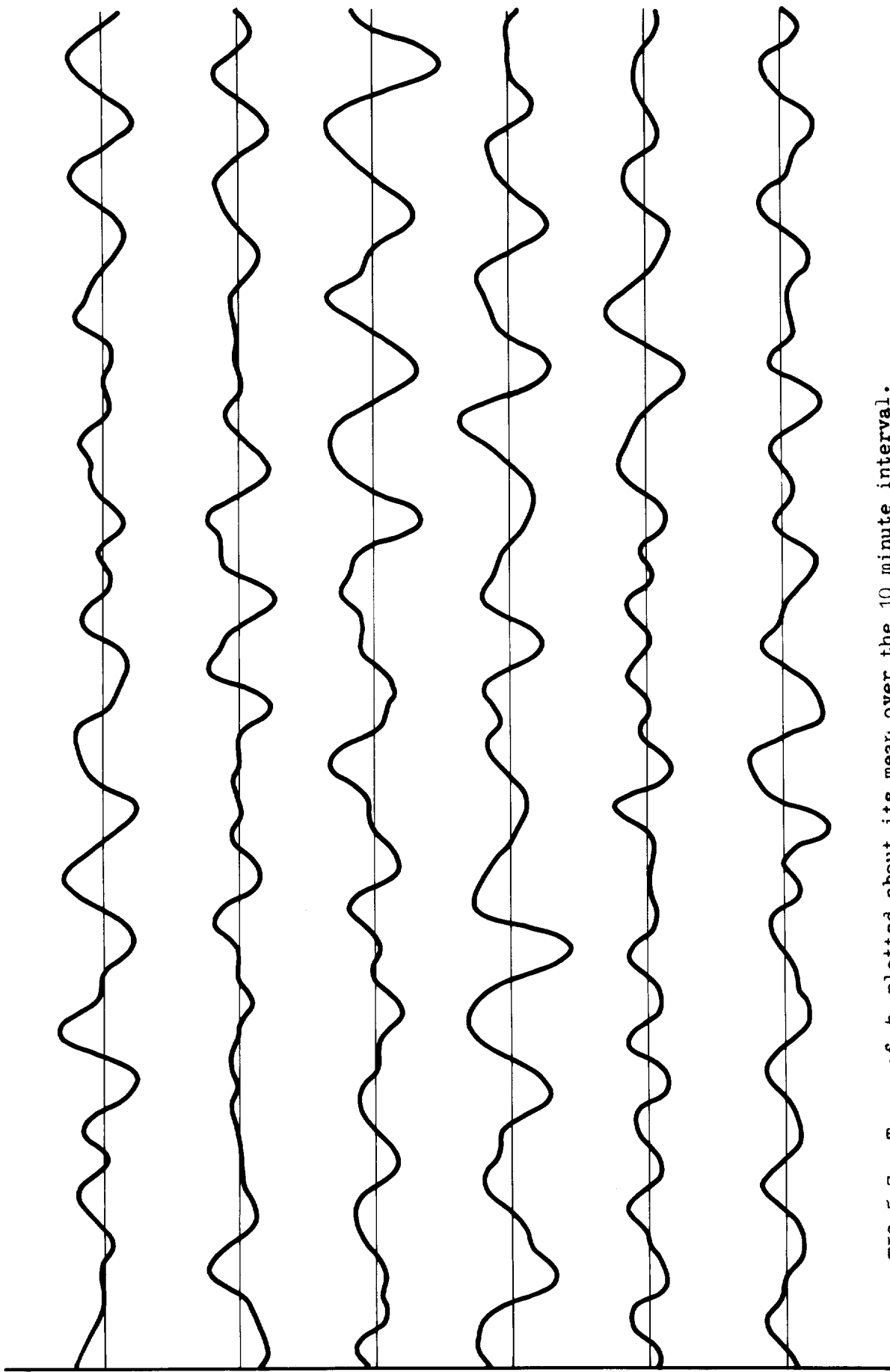
FIG 5.7   Trace of $\hat{p}_2$ plotted about its mean over the 10 minute interval.

Signal variance 42.5 $(cms.H_2O)^2$.

$\dfrac{(cms./sec.)^2}{Hz.}$

Energy Spectrum of w_z

Frequency Hz.

FIG 5.8

$\dfrac{(cms/sec.)^2}{Hz.}$

Energy Spectrum of u_x

Frequency Hz.

FIG 5.9

$\frac{(cms./sec.)^2}{Hz.}$

Energy Spectrum of u_v

Frequency Hz.

FIG 5.11

$\frac{(cms./sec.)^2}{Hz.}$

Energy Spectrum of w_u

Frequency Hz.
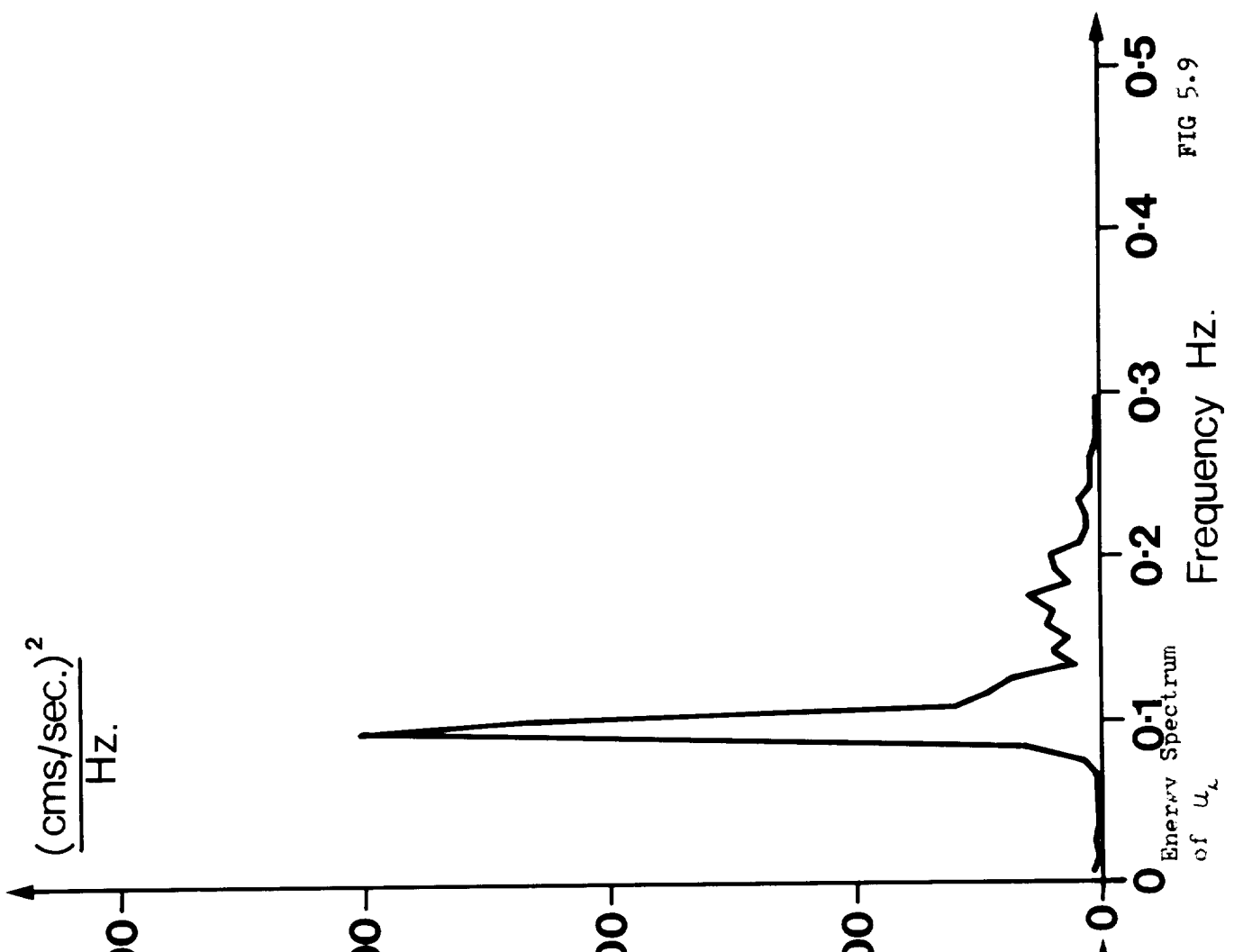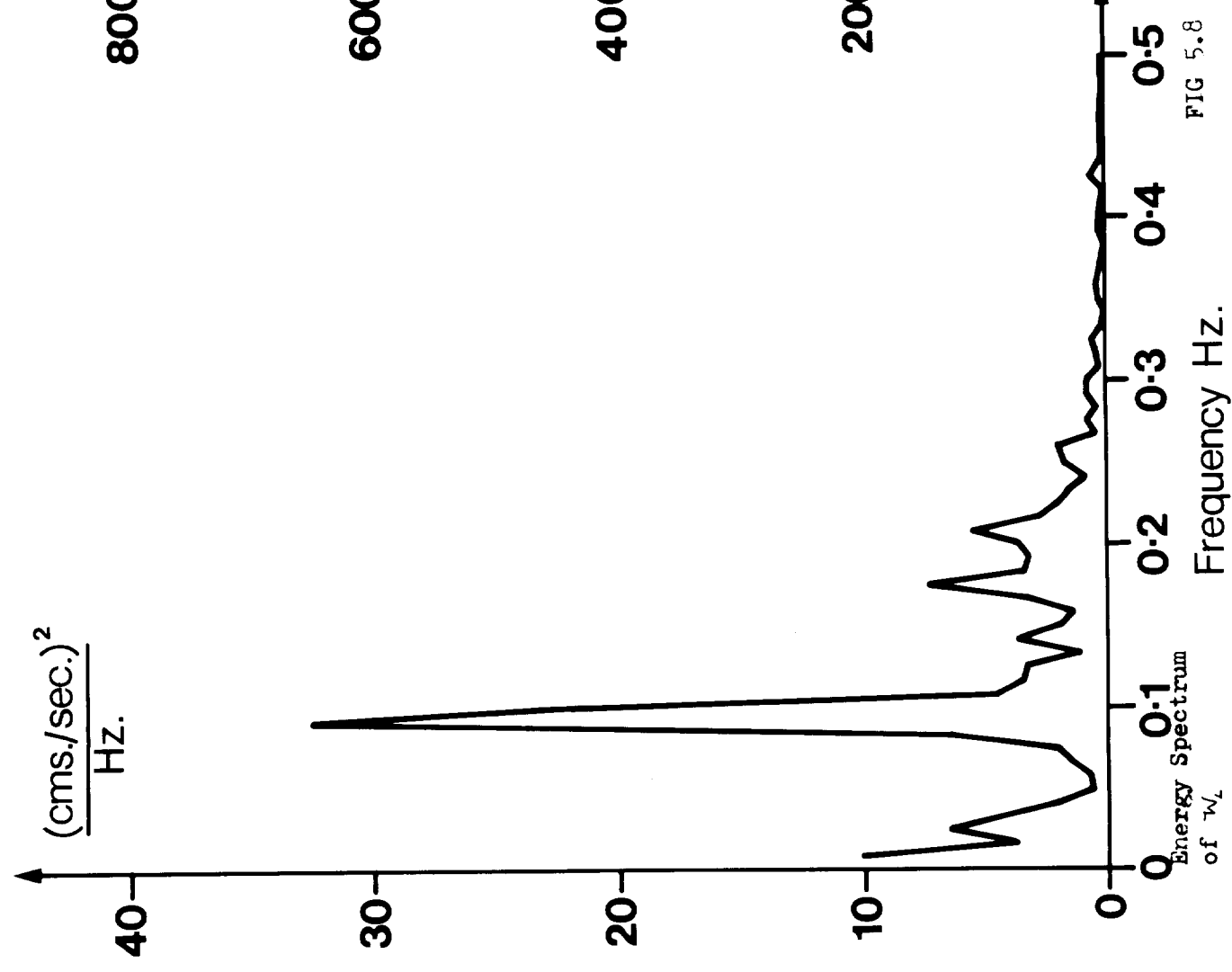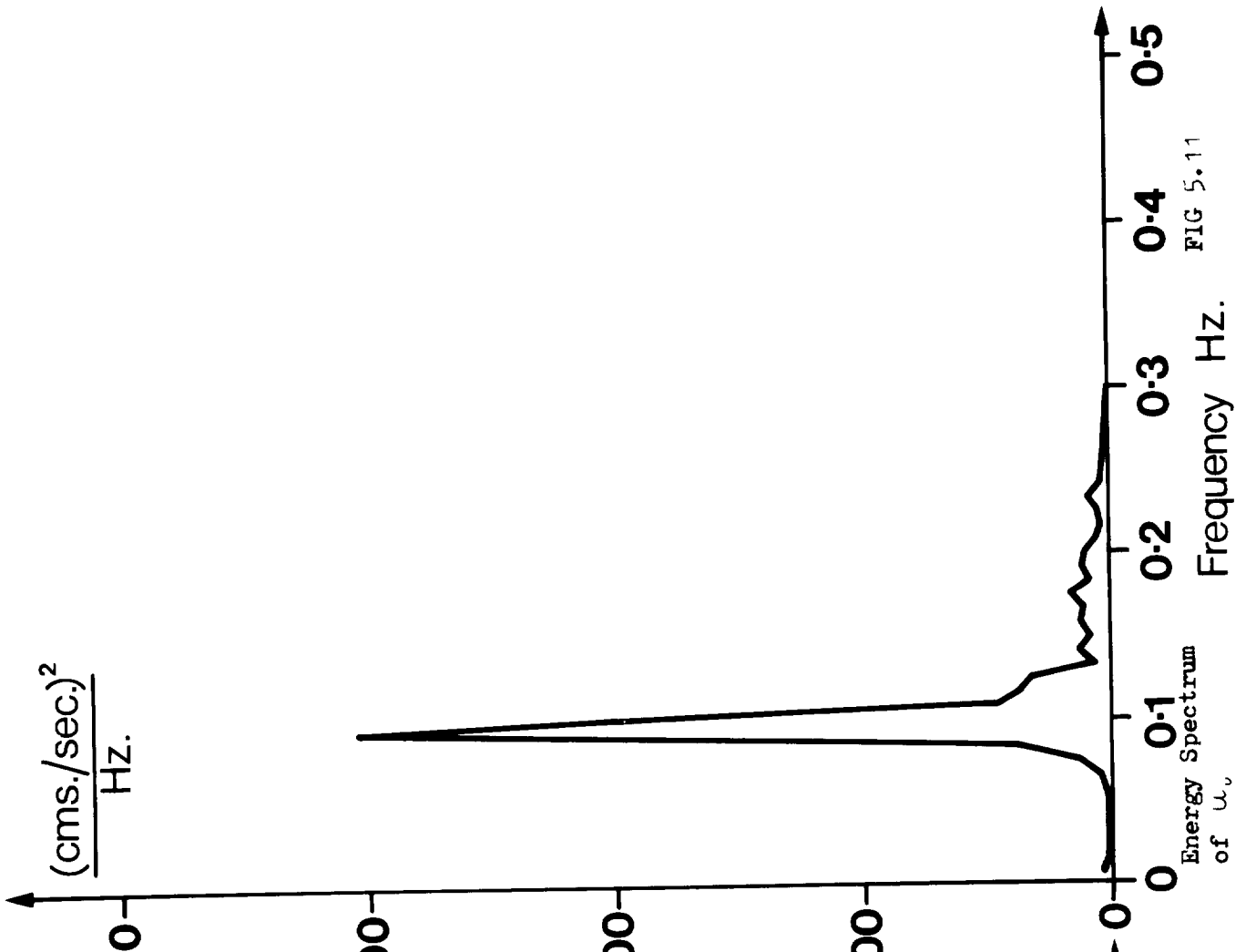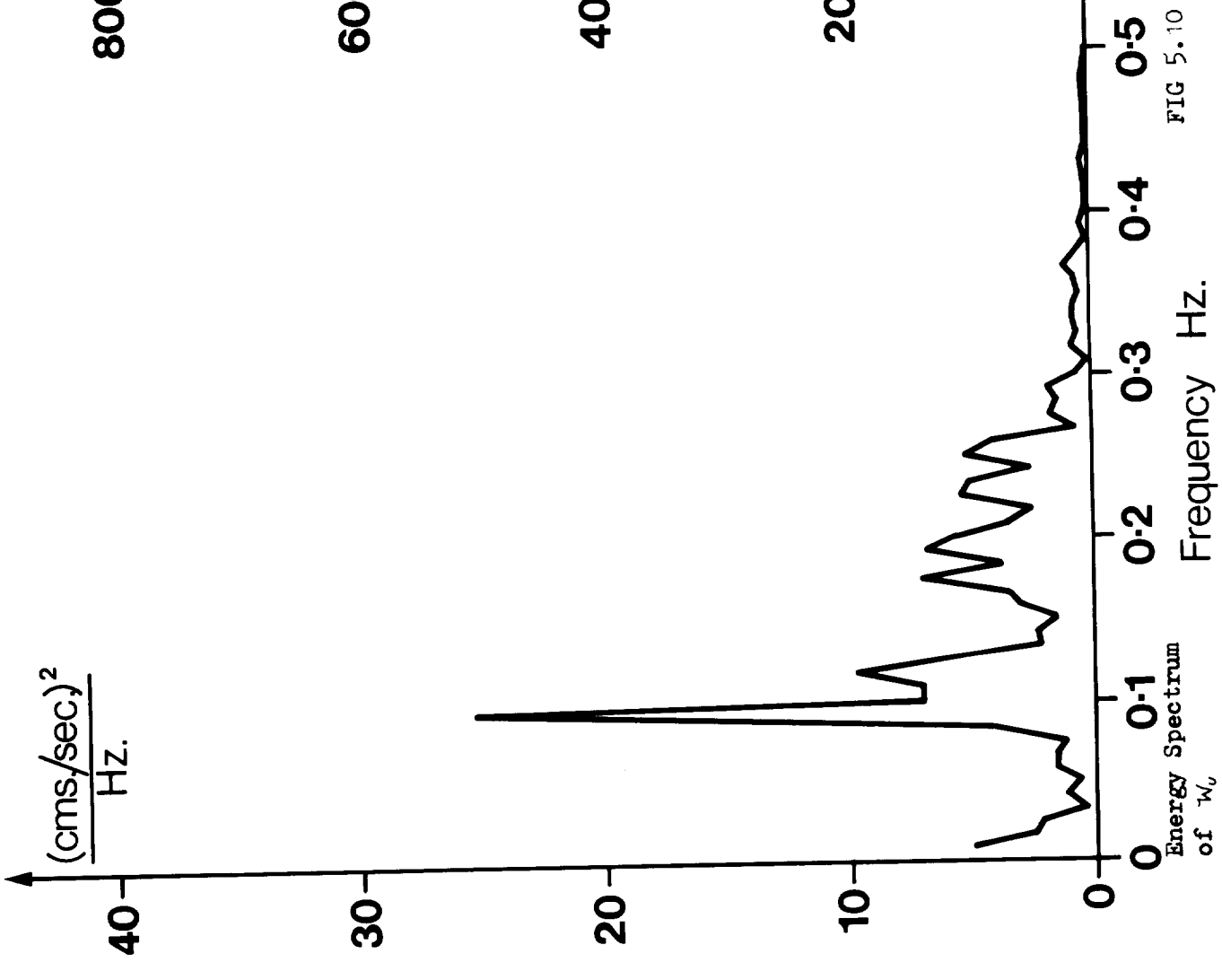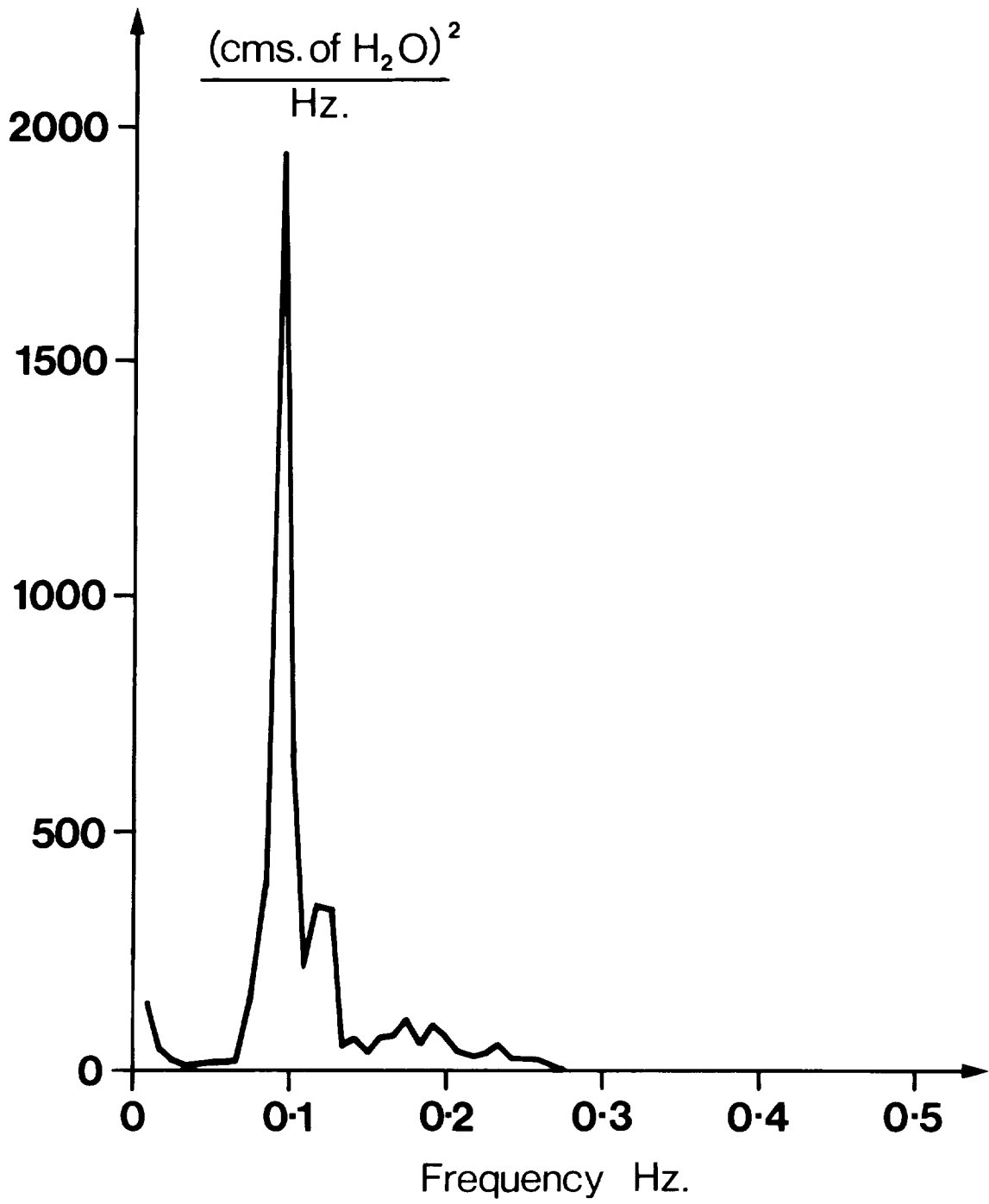
FIG 5.10

FIG 5.12   Spectrum of p_2
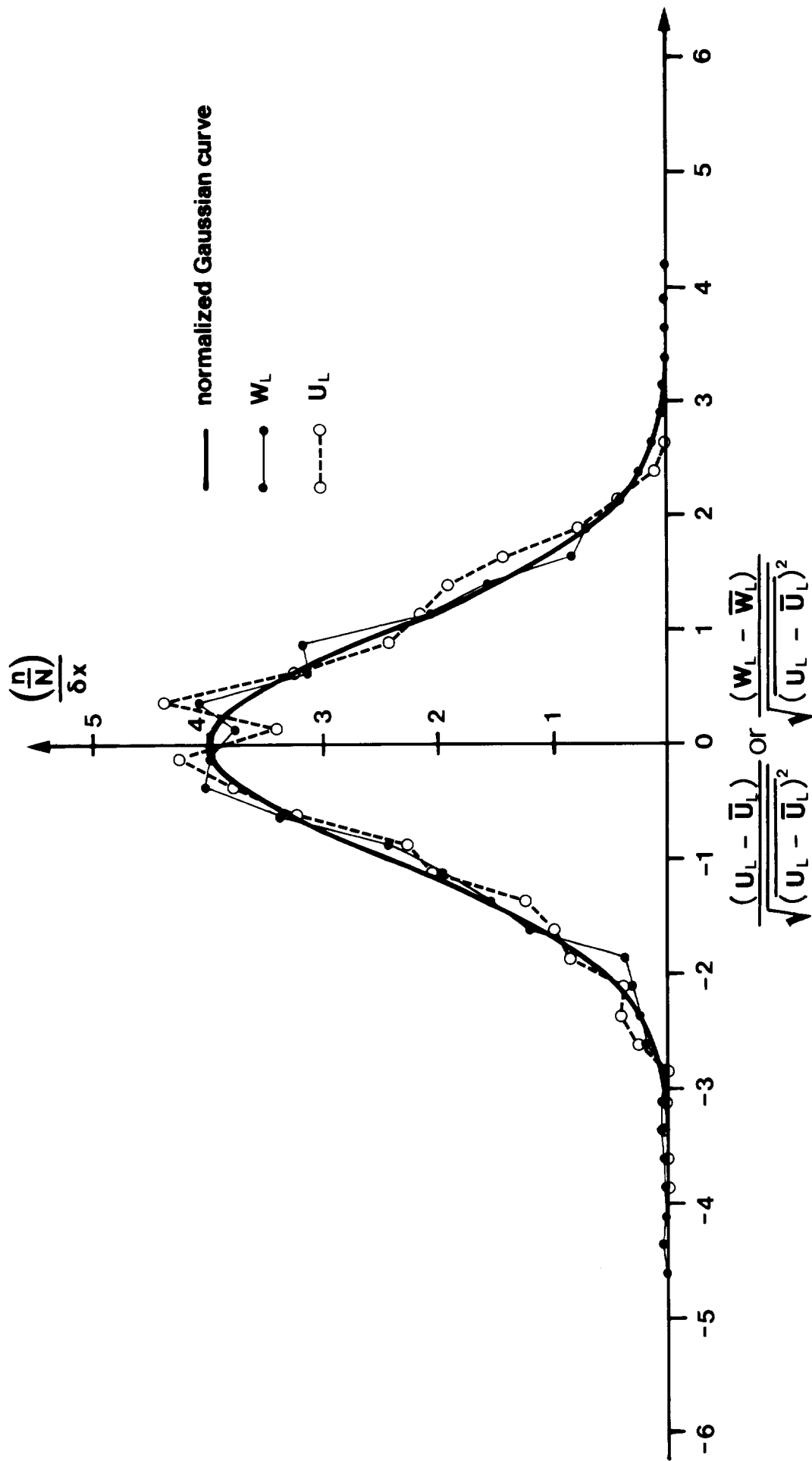
Fig 5.13 Normalized probability density functions of u_L and w_L, plotted together with the normalized Gaussian curve. (Notation: n occurrences of the N digitized values overall, lying in a band of width $\delta x = \frac{1}{4} x \{$ standard deviation of the signal$\}$).
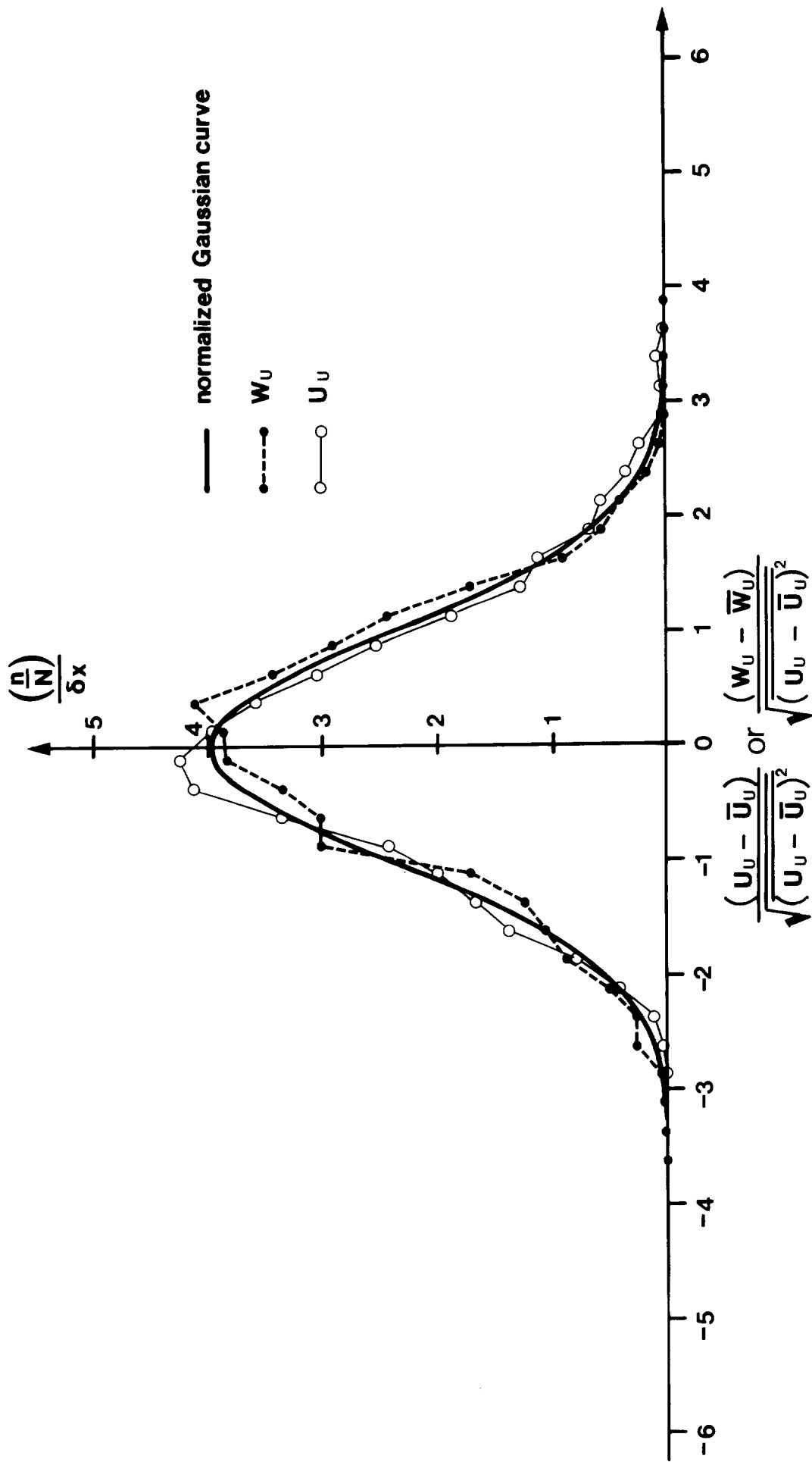
FIG 5.14   Normalized probability density functions of u_v and w_v, plotted together with the normalized Gaussian curve. For notation, see caption to Fig 5.13.
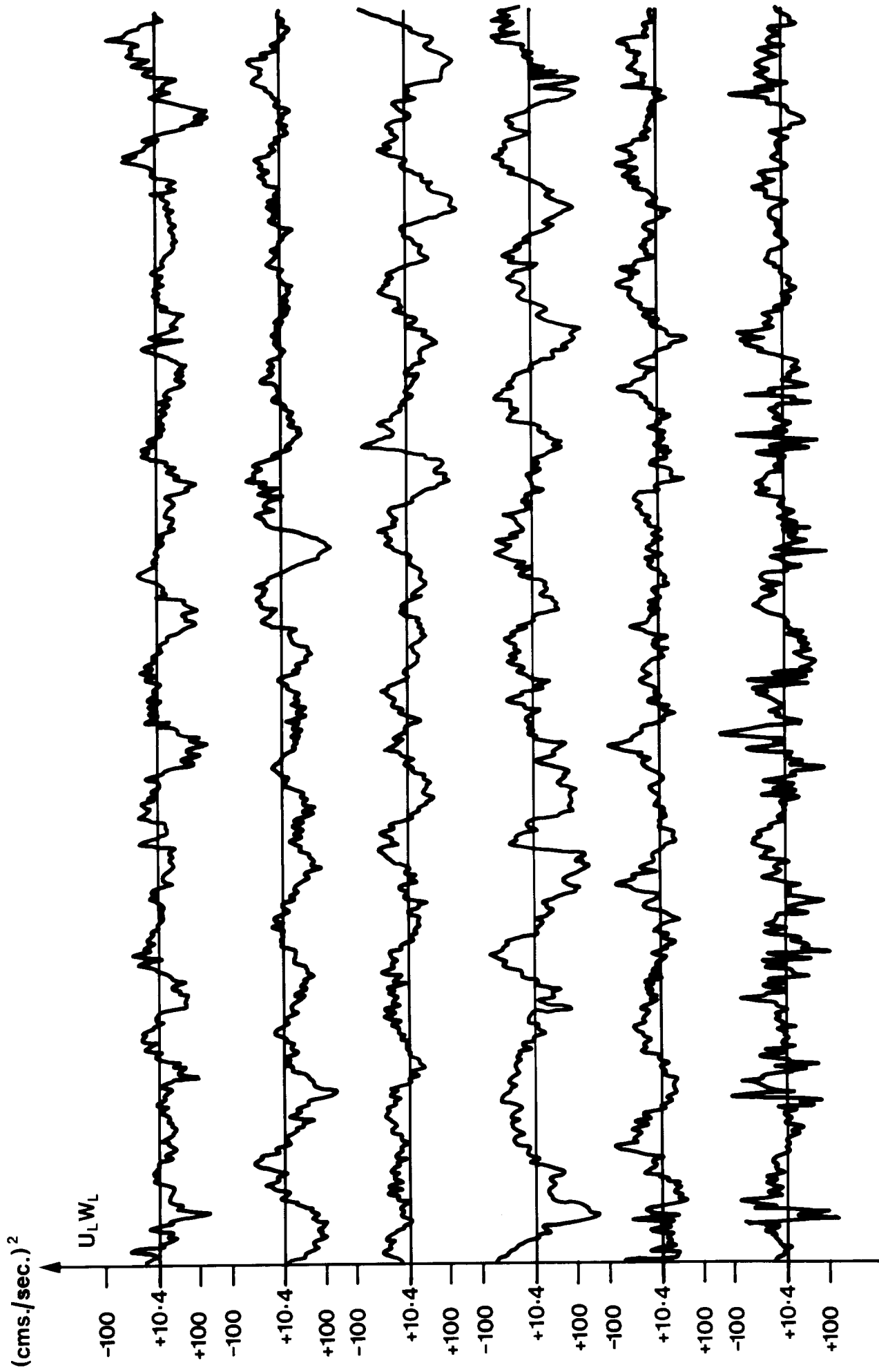
(cms./sec.)^2

$U_L W_L$

-100 $+10.4$ $+100$ -100 $+10.4$ $+100$ -100 $+10.4$ $+100$ -100 $+10.4$ $+100$ -100 $+10.4$ $+100$ -100 $+10.4$ $+100$

FIG 5.15 Trace of $U_L W_L$ plotted about its mean ($=10.4$ (cms/sec)^2) taken over the 10 minute interval.
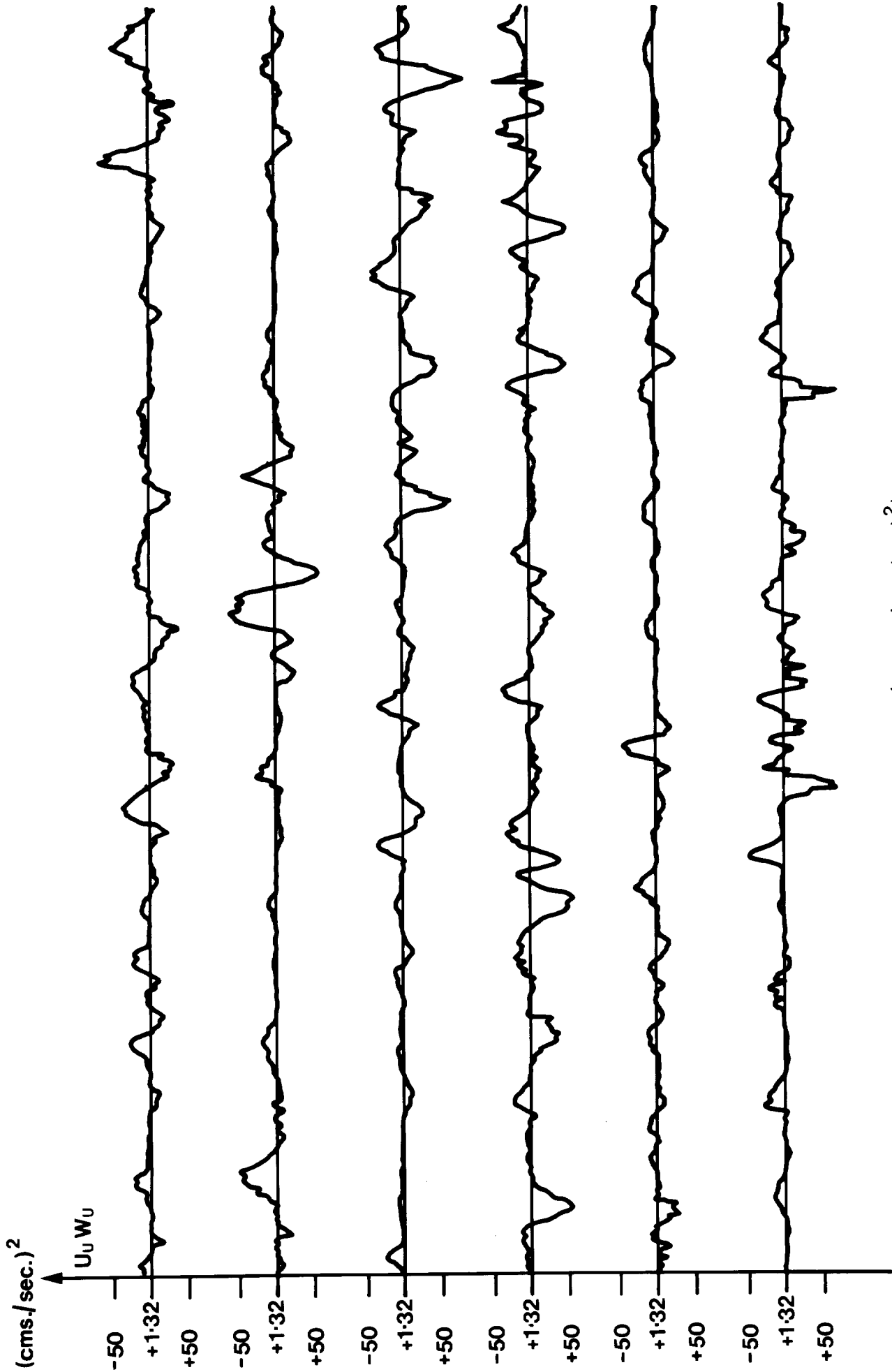
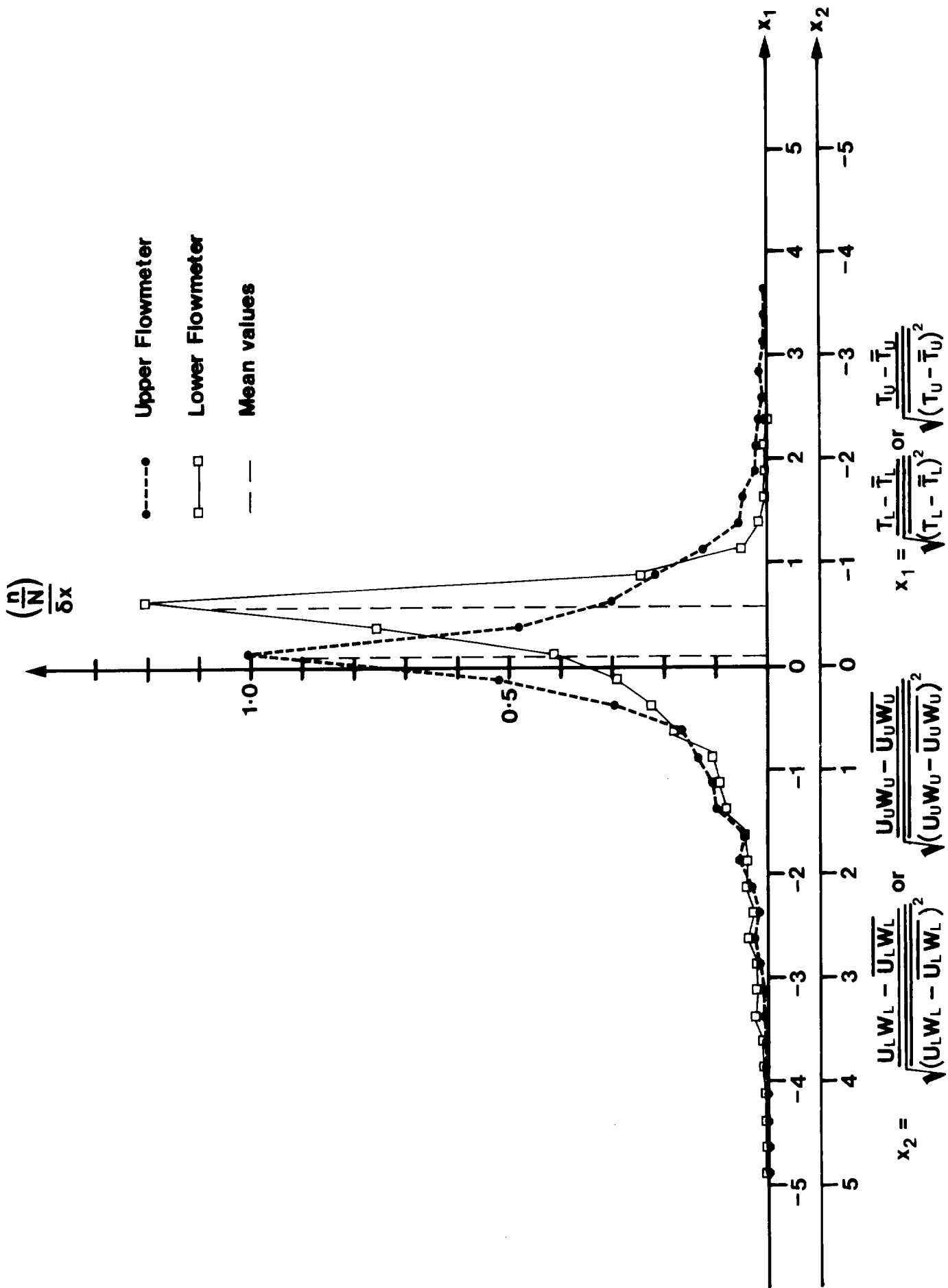FIG 5.16 Trace of $u_U w_U$ plotted about its mean ($=1.32$ $(cms/sec)^2$) taken over the 10 minute interval.

FIG 5.17 Normalized probability density functions of $u_L w_L$ and $u_U w_U$. (For notation, see caption to Fig 5.13). The double scale ($x_{1,2}$) shows the distribution both in terms of instantaneous stress values and instantaneous values of the uw product

Figure Caption to Fig 5.17

Instead of 'Mean values', insert 'Position of the vertical axis (in relation to each drawn curve) had $\overline{uw}$ not been subtracted from uw '.
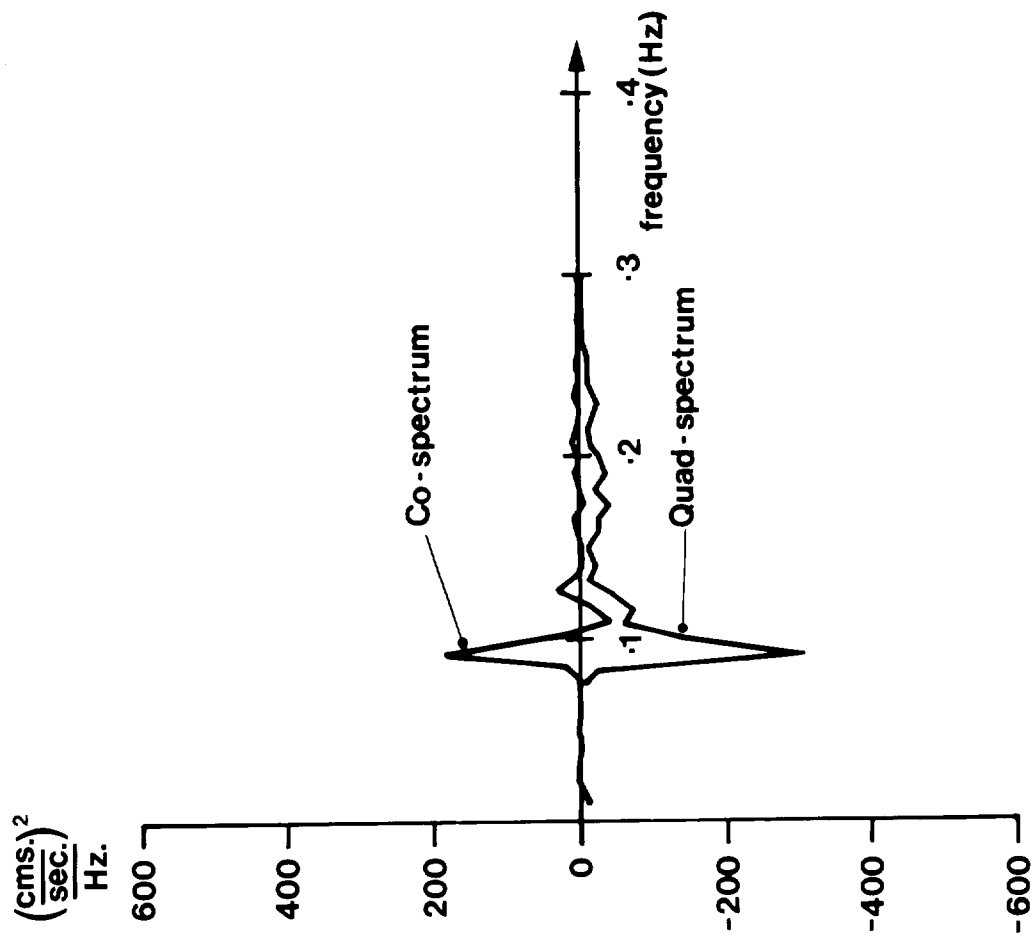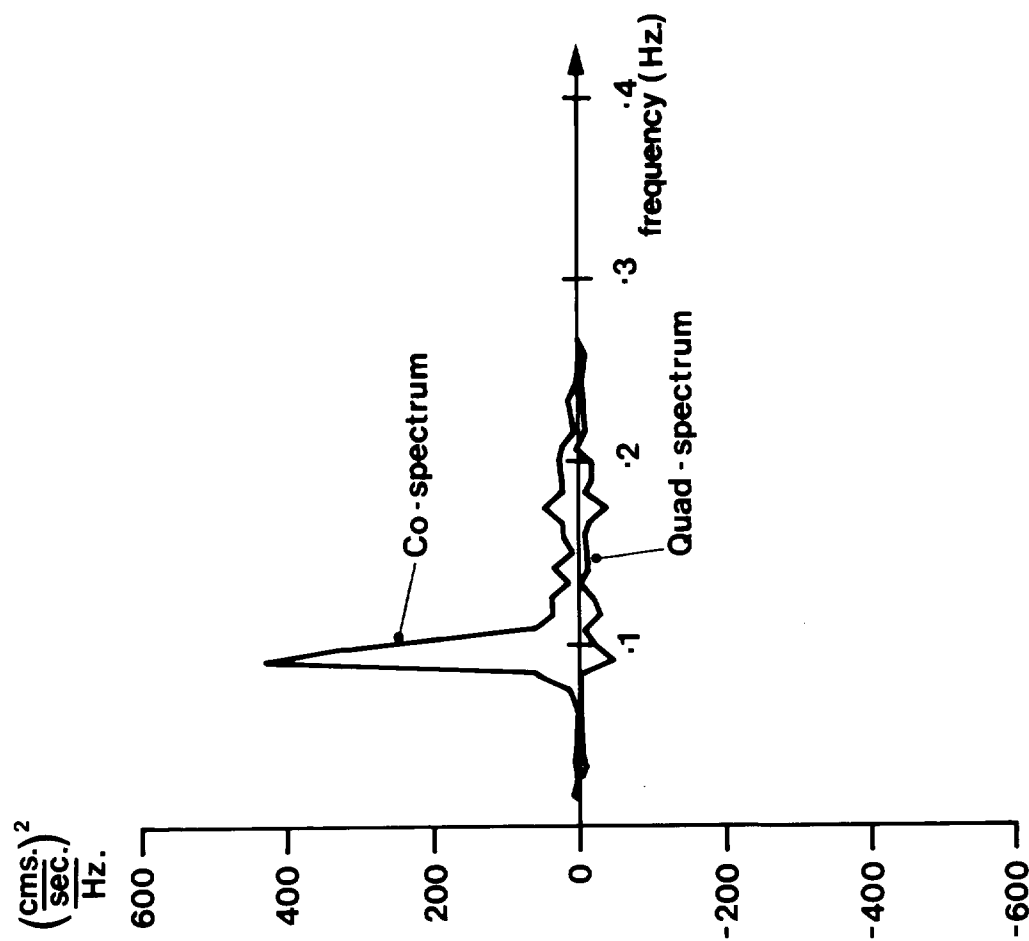
FIG 5.18   Cross spectrum of u_ν and w_ν

FIG 5.19   Cross spectrum of u_ν and w_ν